

2018

Diffusion of Ultra-Cold Neutrons in Randomly Rough Channels

Sarah Elizabeth Brent
University of Rhode Island, sbrent@uri.edu

Follow this and additional works at: https://digitalcommons.uri.edu/oa_diss

Terms of Use

All rights reserved under copyright.

Recommended Citation

Brent, Sarah Elizabeth, "Diffusion of Ultra-Cold Neutrons in Randomly Rough Channels" (2018). *Open Access Dissertations*. Paper 720.
https://digitalcommons.uri.edu/oa_diss/720

This Dissertation is brought to you by the University of Rhode Island. It has been accepted for inclusion in Open Access Dissertations by an authorized administrator of DigitalCommons@URI. For more information, please contact digitalcommons-group@uri.edu. For permission to reuse copyrighted content, contact the author directly.

DIFFUSION OF ULTRA-COLD NEUTRONS IN RANDOMLY ROUGH
CHANNELS

BY

SARAH ELIZABETH BRENT

A DISSERTATION SUBMITTED IN PARTIAL FULFILLMENT OF THE
REQUIREMENTS FOR THE DEGREE OF
DOCTOR OF PHILOSOPHY
IN
PHYSICS

UNIVERSITY OF RHODE ISLAND

2018

DOCTOR OF PHILOSOPHY DISSERTATION
OF
SARAH ELIZABETH BRENT

APPROVED:

Dissertation Committee:

Major Professor Alexander Meyerovich

Leonard Kahn

David Freeman

Nasser H. Zawia

DEAN OF THE GRADUATE SCHOOL

UNIVERSITY OF RHODE ISLAND

2018

ABSTRACT

This thesis deals with ultra cold neutrons, or, more precisely, with beams of ultra-cold neutrons. ultra-cold neutrons are longwave particles produced in a reactor from which they are coming to experimental cells through narrow channels. The beams are collimated so that the distribution of longitudinal and transverse velocities is narrow. The energies of the neutrons that we consider as ultra cold are somewhere around $100neV$.

Neutrons with such low energies have long wavelengths; $\lambda \sim 100nm$. Neutral particles with such large wavelengths exhibit nearly (locally) specular reflection when reflected by the solid surfaces at almost any angle of incidence.

The number of ultra-cold neutrons available for experiment is extremely small. Therefore, a major experimental challenge is not to lose any particles while they travel from the reactor to the lab. Some of the main losses occur in the channel junctions when the neutrons disappear into the gaps between the overlapping channels. We explore the possibility of recovering some of these otherwise "lost" neutrons by making the inside surfaces of the junctions rough: scattering by the surface roughness can send some of the neutrons back out of the gap. This practical goal made us to re-examine diffusion of neutrons through rough channels which is by itself an interesting problem. We assume that the correlation function of random surface roughness is either Gaussian or exponential and investigate the dependence of the mean free path on the correlation radius R of the surface inhomogeneities. My results show that in order to ensure better recovery of the "lost" neutrons the walls of the junction should be made rough with the exponential correlation function of surface roughness with as small a correlation radius as possible. The results also show that the diffusion coefficient and the mean free path of UCN in rough channels exhibit a noticeable minimum at very small values

of the correlation radius. This minimum sometimes has a complicated structure.

The second goal is the study of UCN in Earth's gravitational field. One of the most interesting features of ultra-cold neutrons is a possible quantization of their vertical motion by the Earth's gravitational field: the kinetic energies are so low that they become comparable to the energy of neutrons in Earth's gravitational field. This results in quantization of neutron motion in the vertical direction. The energy discretization occurs on the scale of several peV.

In the first part of my thesis I ignore the presence of the gravitational field and look at the transport of neutrons through rough waveguides in the absence of gravity. The effects of gravity are explored in the last part. To streamline the transition I use the common notations suitable for both types of problems.

More specifically, I am studying the diffusion of ultra-cold neutrons in the context of the experiments done at ILL in Grenoble in the frame of the multinational GRANIT collaboration. The parameters used in numerical calculations are the ones most common to ILL experiments. I will be calculating the diffusion coefficient and the mean-free path (MFP) under the conditions of the quantum size effect. Specifically I look at the dependence of the diffusion coefficient and the MFP on the correlation radius of surface inhomogeneities, R . In the second and third parts of the thesis I include the study of the neutron diffusion accompanied by slow continuous disappearing of neutrons as a result of penetration into the channel walls. This includes calculating the number of neutrons $N(t = \tau_{ex}, h, R)$, where τ_{ex} is the experimental value of the time of flight in GRANIT experiments and h is the channel width. I look not only at the square well geometry, but will also include the effects of the Earth gravitational field. The results show that while the neutrons in the square well potential disappear almost immediately, the small perturbation near the bottom of the well caused by the presence of the Earth's

gravitational field drastically changes the results and is solely responsible for the observed exit neutron count in GRANIT experiments. The shape of the curves describing the exit neutron count on the width of the waveguide is extremely robust. Our brute force calculations also confirm that the earlier biased diffusion approximation is quite accurate.

ACKNOWLEDGMENTS

I would like to acknowledge first and foremost my thesis adviser, Professor Alexander Meyerovich. I am deeply grateful for the guidance, advice, tremendous insight and immeasurable patience and support that you provided to me over the past 6 years.

I would also like to acknowledge Professor Leonard Kahn for the wonderful teacher that he is, for the encouragement that he provided even at times when I had doubts, and for the many informal conversations we had on a vast array of topics.

Sincere thanks go out to Professor Gerhard Muller, for all the physics tools he gave me over the past 6 years, as well as the many enjoyable and insightful conversations.

Thanks to Professor Peter Nightingale, for the crazy difficult classes that provided me with great challenges, as well as for his wit and generosity in sharing knowledge about music, history and other topics outside of physics.

Thank you to Professor Richard McCorkle for being a great support to me in my function as a TA, as well as always having a pleasant outlook on life.

Thank you to Linda Connell for always cleaning up my administrative messes, as well as being a great friend and support over the last 6 years.

Thank you to Steve Pellegrino for helping me with countless technology and computer problems, as well as for his friendship.

Thank you to David Notorianni for always fixing anything that went wrong in the labs or offices, as well as for having a kind heart behind the rough exterior.

Thank you to Professor Donna Meyer, for introducing me to engineering which has become another passion of mine, as well as for being a great role model for a woman in the hard sciences. I have great admiration for you.

Thank you to Professor Stephen Barber, who though not a disciple of the sciences, I have learned so much from, not only in English literature, theory and history but from who you are as a person. You are one of the most generous and loving people I know, thank you for sharing yourself with me, I'm a better person because of it.

Thank you to my dear friend Mauricio Escobar, who has always been a stellar friend as well as a confident and support, even after he himself was done with his Ph.D.

Thank you to Eden Uzrad and the entire Uzrad family in Israel, whom I got to know very well over the course of my Ph.D. Thank you for all the support you gave me, for your generosity, and for opening my eyes about your beautiful country.

Thank you to the woman of my life, Cecile Cres, whom I've been lucky to have known since high school. You always encouraged me to pursue my passions, and I thank you so much for being my greatest confident, as well as source of comfort and support in my life.

Lastly, but certainly not least, a huge thank you to my parents for the education they gave me, for always allowing me to follow my dreams, and providing me with endless support in all my endeavors. In particular I would like to thank my mom, who has always had my back 100 percent of the time, even at times when she didn't agree with my decisions. I wouldn't be the person I am today without you

DEDICATION

This thesis is dedicated to the two most important women in my life who have loved and encouraged me always. To my incredibly strong and bright mother, Antoinette Duymovitsh, whom I admire so much, and to whom I owe everything. And to my partner Cécile who encourages and supports me unconditionally on this wild and fun ride called life, and from whom I learn daily.

Contents

ABSTRACT	ii
Acknowledgements	vi
List of Tables	xii
List of Figures	xiii
Chapter 1. Introduction	1
1.1. Preliminary Comments	1
1.2. GRANIT Experiment	8
1.3. Notations and Dimensionless Variables	14
1.4. Theoretical Background	17
Chapter 2. Diffusion Coefficient and Mean Free Path in a Rough Waveguide	26
2.1. Introductory Comments	26
2.2. The Diffusion Coefficient	27
2.3. Mean Free Path	28
2.4. Numerical Results	29
2.5. Conclusions	37

Chapter 3. Neutron Beams between Absorbing Rough Walls: Square Well	
Approximation	44
3.1. Description of Problem	44
3.2. Wavefunction for the Square Well	48
3.3. Transition Probabilities and Neutron Count	50
3.4. Numerical Results	52
3.5. Conclusions	60
Chapter 4. Neutrons in the Rough Waveguide in the Presence of Gravity	67
4.1. Gravity-Imposed Changes: Similarities and Differences with the Previous Chapter	67
4.2. Results from the Preceding Work: the Biased Diffusion Approximation	70
4.3. Exact Calculation of the Absorption Time	75
4.4. Numerical Results	78
4.5. Conclusions	85
Chapter 5. Summary and Conclusions	96
5.1. Main Conclusions	96
5.2. Recommendations for Future Work	99
Appendix A. Dimensionless Transition Probabilities	101
Appendix B. Asymptotic Expansion for Transition Probabilities for Surfaces with Exponential Roughness Correlator	103

Appendix C. Diagonal Elements of Transition Probabilities for the Biased Diffusion Approximation	105
Bibliography	107

List of Figures

- 1.1 Sketch of the experimental cell with a neutron beam between two plates. The neutrons bounce between the "rough" ceiling and "smooth" floor. The neutrons with low vertical velocity, which do not reach the ceiling get to the detector. 9
- 1.2 The GRANIT experiment: a more technical sketch of the experiment as a whole. The experimental cell is on the right. 11
- 1.3 "Rough" ceiling mirror. The patches 1-5 represent the spots where the roughness has been measured using vertical scanning interferometry. 13
- 2.1 Minima of the diffusion coefficient $d(r)$ as a function of the correlation radius for the Gaussian inhomogeneities. The diffusion coefficient starts growing again at larger r . 32
- 2.2 Diffusion coefficient $d(r)$ for the Gaussian surface correlator over large range of r . The minima in $d(r)$ cannot be resolved on this scale. 33

2.3	The next figure (Fig.[2.4]) shows the diffusion coefficient for the exponential correlation function of surface roughness.	34
2.4	Diffusion for the surface inhomogeneities with the exponential correlation function over large range of r .	35
2.5	Mean free path $l(r)$ for the surface with Gaussian roughness over wider range of r .	36
2.6	Mean free path for the surface with exponential roughness over wider range of r .	37
2.7	Mean-free path $l(r)$ for both Gaussian and exponential correlation functions for small r .	38
2.8	MFP for Gaussian correlation function for various channel widths $h = 16, 8, 4$.	39
2.9	MFP for Gaussian (1) and exponential (2) surface correlation functions over a wide range of r .	40
2.10	Power law fitting for the MFP $l(r)$ surfaces with the Gaussian correlation function for r from 20 to 40.	41
2.11	The power law fit for MFP $l(r)$ for Gaussian inhomogeneities over the range of r from 40 to 60	42
2.12	Power law fit for $d(r)$ the exponential surface correlation function over a large range of r .	43

3.1	Sketch of neutron beam entering the experimental cell: the neutrons pass between rough "ceiling" and smooth "floor".	45
3.2	Square well levels.	47
3.3	Coefficients $b_j(h)$ Ref[3.3] as a function of the width of the channel h for the square well.	50
3.4	N_e as a function of the cutoff parameter $S1$ for $h = 8$ and $r = 0.65$. Here we can see the initial increase.	54
3.5	Neutron count as a function of the size of the matrix $S1$ for $h = 8$ and $r = 0.65$. We can see how it saturates nicely, at about $S1 = 300$. In this plot we are looking at N_e over a larger scale.	55
3.6	N_e as a function of the size of the matrix $S1$ for $h = 5$ and $r = 0.65$. We are looking at N_e closer scale, so that we can see the initial increase and gradual saturation.	55
3.7	Saturation of the neutron count as a function of the size of the matrix $S1$, for $h = 5$ and $r = 0.65$.	56
3.8	N_e as a function of the matrix size $S1$ for $h = 3$ and $r = 0.65$. We are looking at N_e closer scale, so that we can see the initial increase and gradual saturation.	56
3.9	Neutron count as a function of the cutoff parameter $S1$ and $r = 0.65$ for $h = 3$.	57

3.10	$N_e(h)$ as a function of h for $r = 0.1$.	58
3.11	$N_e(h)$ as a function of h for $r = 1$.	59
3.12	$N_e(h)$ as a function of h for $r = 5$.	60
3.13	$N_e(h)$ as a function of h for $r = 10$.	61
3.14	$N_e(h)$ as a function of h for $r = 30$.	62
3.15	Total neutron count N_e as a function of different correlation radii r for small well width $h = 3$.	63
3.16	Total neutron count N_e as a function of different correlation radii r for well width $h = 5$.	64
3.17	Total neutron count N_e as a function of different correlation radii r for well width $h = 7$.	65
3.18	Total neutron count N_e as a function of different correlation radii r for well width $h = 9$.	66
4.1	Sketch of the gravitational well as a function of z .	68
4.2	The first three eigenvalues for both the square well and the gravitational well as a function of the well width h . For better comparison, the bottom of the square well is chosen in the middle of the bottom of the gravitational well, $mgh/2$, and is drifting with h . The eigenvalues for the gravitational well are the lower curves, for the SW-the upper.	69

4.3	A few coefficients b_j 's as a function of well width size h for both the square (lower curves) and the gravitational wells (upper curves).	70
4.4	The first nine coefficients b_j as a function of the width of the channel h for the gravitational well. The lowest curve is b_1 and the highest b_9 .	71
4.5	The transition probabilities $W_{1j'}$ as a function of j' exhibit the peak around $j' = 100$.	78
4.6	Potential with Earth's gravity field.	80
4.7	Neutron exit count as a function of h , for experimental parameters.	82
4.8	Neutron count as a function of h for correlation radius radius of roughness $r = 0.1$.	83
4.9	Neutron count as a function of h for correlation radius of roughness $r = 1$. This is approximately twice the experimental value of r .	84
4.10	Neutron count as a function of h for correlation radius of roughness $r = 5$.	85
4.11	Neutron count as a function of h for correlation radius of roughness $r = 10$.	86

4.12	Neutron count as a function of h for correlation radius of roughness $r = 20$.	87
4.13	Neutron count as a function of h for correlation radius of roughness $r = 30$.	88
4.14	Neutron count as a function of h for correlation radius of roughness $r = 50$.	89
4.15	Neutron count as a function of h for correlation radius of roughness $r = 100$.	90
4.16	Neutron count as a function of h for correlation radius of roughness $r = 500$.	91
4.17	Neutron count as a function of h for correlation radius of roughness $r = 1000$.	92
4.18	Neutron exit count for fixed well width at $h = 9$, over a large range of r .	93
4.19	Neutron exit count for fixed well width at $h = 5$, over a large range of r .	94
4.20	Neutron exit count for fixed well width at $h = 3$, over a large range of r .	95

CHAPTER 1

Introduction

1.1. Preliminary Comments

The main goal of this thesis is to provide a rigorous theoretical description for the diffusion of ultra cold neutrons (UCN) through narrow rough channels, which is based on the theory of quantum transport in systems with rough boundaries formulated by *Meyerovich et al.*[1]-[12]. We look at two separate problems: diffusion of the neutrons through rough waveguides on the way from the reactor to the experimental cell and the neutron count for neutrons exiting experimental cell with absorbing walls.

We use numerical computations to investigate the effect of two types of random roughness on the diffusion coefficient and use numerical methods to evaluate the neutron count using the experimental values of input parameters. We analyze two types of potentials inside the cell: one the idealized square well potential (SW) and the other the SW potential with an addition of the gravitational field. The experimental parameters were provided for us by our experimental collaborators at the Institute Laue-Langevin (ILL) in Grenoble, France in the frame of the GRANIT project.

The purpose of this multinational collaborative experimental and theoretical work is two-fold: to investigate the quantization of the motion of UCN by the Earth gravitational field and to create UCN with well-defined energies in the peV range necessary for studies of fundamental forces in quantum field theory.

Typical UCN coming out of the reactor have large wavelengths, $\lambda \sim 100$ nm. Neutral particles with such large wavelengths exhibit nearly (locally) specular reflection when reflected by the solid surfaces at almost any angle of incidence. One of the most interesting features of ultra-cold neutrons is their quantization in the Earth gravitational field: the particle kinetic energies can be so low (~ 1 peV) that they become comparable to the gravitational energy of neutrons in Earth's gravitational field. This results in quantization of neutron motion in the vertical direction. This discretization is illustrated in the sketch below showing the discrete energy levels of neutrons in the Earth gravitational field. The energy discretization occurs on the scale of several peV. The first experimental observation of such a quantization was done by *Nesvizhevsky et al.* Ref.[14]-[24] by using the GRANIT spectrometer (see below).

Ultra-cold neutrons are longwave particles produced in a reactor from which they are coming to experimental cells through narrow channels containing various mirrors and collimators. The UCN beams are collimated so that the distribution of longitudinal and transverse velocities is narrow. The energies of the neutrons that we consider as ultra-cold are somewhere around 100 neV, and below.

The particles in the beam that reach the cell have a relatively large horizontal velocity and much smaller vertical velocities. Still standard collimation and cooling methods are insufficient to limit the vertical energies to the peV scale comparable to gravitational energies. The typical UCN beam brought to the experimental cell contains neutrons in thousands of occupied gravitational states making it virtually impossible to study the quantization of vertical motion.

The purpose of the GRANIT spectrometer is to eliminate the particles in higher gravitational states and leave only the ones in the few lowest states. This allows one to achieve both goals: to study the quantization of neutron motion in the gravitational field and to produce neutrons with well-defined energies in the peV range.

The lower surface of the spectrometer is as close as possible to being perfectly smooth, in order to make it to be a perfect reflector which specularly reflects the UCN. The upper surface of the GRANIT cell has microscale roughness. This "rough" ceiling scatters the UCN in higher gravitational states, which can reach it. The scattered neutrons from the higher gravitational states eventually acquire large vertical velocities sufficient to trigger penetration through the walls and disappearance from the system. Due to this setup, only the UCN in low gravitational states, which do not reach the rough ceiling, can continue bouncing along the flat floor and arrive at the exit neutron detector.

The use of rough mirrors as quantum state selectors is possible because the very large horizontal velocities in the beam and peculiarities of quantization of the

vertical motion in the gravitational field. This kind of state selector is used or is planned to be used, in numerous other applications not exclusive to GRANIT experiments or to UCN beams. Some examples of these potential applications include: the observation of quantum gravitational states for other ultra-cold particles and anti-particles in the context of the GBAR project at CERN [[28]-[32]]; the resolution of centrifugal quantum states in UCN in the "whispering gallery" [[26],[27]]; the search for fundamental forces at extra-short range as predicted by the grand unification theory [[33]-[41]]; the test of the weak equivalence principle [[39]-[42]]; the continual extension of understanding of quantum mechanics. Additionally, these GRANIT-like experiments could potentially be used to measure the electric dipole moment of a neutron [[46],[47]], if it exists, help to search for the potential neutron charge [[48],[49]], and make a precise measurement of neutron lifetime [[50]].

The resolution and the quality of the observed quantum gravitational states of UCN rely on the quality of the roughness of the upper surface of the GRANIT cell. *Meyerovich et al.* developed a theoretical framework in which they analyzed the particle diffusion along the random rough walls and linked it to the roughness parameters of the rough mirror. The theory generally agrees with the experimental results despite uncertainty in certain parameters.

Additionally, *Meyerovich et al.* [[52]-[55]] discovered that the shape of the correlation function of surface inhomogeneities (CF) plays a very important role in the diffusion of UCN along rough walls. It turns out that the roughness-driven

transition probabilities between the states are directly proportional to the Fourier image (the so-called power spectrum) of the CF. In previous work, *Escobar et al.* [[8]] showed that within the biased diffusion approximation all the information about the surface imperfections can be accounted for in the neutron count as a single parameter Φ , which is a complicated integral of the power spectrum. However, in practice, it is impossible to create imperfections with a predetermined CF on real surfaces, and even if it were possible it would be highly non-trivial to identify this CF.

In order to increase the resolution of the observed quantum gravitational states of the UCN in the GRANIT spectrometer, proper identification of the surface correlator is paramount. If one can establish a superior way to control the necessary random roughness of the scatterer and absorber mirror, it will contribute greatly to the optimization of results from the GRANIT experiment.

In the context of the theoretical background and numerical experiments, we designate the shape of the CF explicitly, and analyze its potential impact on physical variables. In previous papers, *Meyerovich et al.* [[9]] have analyzed the generated rough surface by measuring it with the computational analog of STM needle (scanning tunneling microscope). Unlike the CF used to generate the surface, the correlator was extracted by direct computation and analyzed using various fitting functions. Alternatively, the extracted correlator was fed directly into the equations for the observables without the fitting functions. The reason for the importance of the numerical experiments with the simulated surfaces lies in showing

how to avoid certain limitations that might stymie the dependable identification of a surface correlator for a real surface.

There is also a supplementary practical issue. The number of ultra-cold neutrons available for experiment is extremely small. Therefore, a major experimental challenge is not to lose many particles while they travel from the reactor to the lab. The main losses occur in the channel junctions when the neutrons get into the gaps between the overlapping channels. Therefore the minimization of losses in channel junctions becomes an important goal which will also be approached in this thesis.

This thesis is arranged as follows:

In the remainder of Chapter 1, we will provide a fairly detailed description of the experiment and its setup used by GRANIT to observe the quantum gravitational states of the ultra cold neutrons. In particular we will describe the GRANIT cell, and introduce the important parameters that are used to describe the roughness of the surfaces of the GRANIT mirror. In section 2 we will discuss the details of the mirror used in the newer experiments including the design and providing a description of how they made the roughness. In section 3 we introduce the main parameters and dimensionless variables. And, finally, in section 4, we will provide the main equations and the theoretical framework for the quantum transport equation and diffusion.

In Chapter 2, we will explore the possibility of recovering these "lost" neutrons that we discussed above by making the inside surfaces of the junctions rough:

scattering by the surface roughness can turn some of the neutrons back. This practical goal made us to re-examine diffusion of neutrons through rough channels which is by itself an interesting general problem. We assume that the correlation function of surface roughness is either Gaussian or exponential (see below) and investigate the dependence of the mean free path on the correlation radius R . Our conclusion is that if ideally we could create the type of roughness we want, it would be better to use exponential roughness.

In Chapter 3, we will be discussing the exit neutron count in an idealized condition, in the square-well potential without gravity. This involves solving large sets of equations with complicated coefficients which tie together neutrons in thousands of quantum states. We first look to investigate the exit neutron count as a function of matrix size, in order to assess the value of the possible cutoff. The matrix size here being the number of equations we are solving. In other words, to reduce the computation time, we deduce what size of the matrix is sufficient for our computations to be accurate. We then cut off the matrix at the cutoff parameter and proceed to extract the neutron count and its dependence on the width of well H . In the case of the square well potential we will see that the neutron count should go quickly to zero.

In Chapter 4, we will be doing something very similar to Chapter 3, except this time we take into account the gravitational potential. To simplify the computations, we assume that the matrix of the interstate transition probabilities has a block structure. The first block contains the transitions between the lowest

(gravitational) states. Since for the higher states there is practically no difference between the gravitational and square well states, the other three blocks describe the transitions between the square well states and between the gravitational and square well states. From this we derive the neutron count.

In the last chapter we will summarize the results presented earlier, and discuss some suggestions for what can be done looking towards the future.

1.2. GRANIT Experiment

1.2.1. Description of the Actual GRANIT Experiment

Neutrons are elementary particles with no charge and a relatively long lifetime (~ 900 s) compared to many other elementary particles, such as mesons ($\sim 10^{-17} - 10^{-8}$ s). This makes neutrons quite a good candidate for experimental observation of quantum mechanical bound states in the weak Earth's gravitational field [[59]]. The quasi-classical estimation of energy levels of bouncing quantum mechanical particles on an ideal horizontal surface in the Earth gravitational field gives a spectrum of a few peV for the lowest energy states of the neutrons [[56]-[58]]. Such low energies make the observation of gravitational quantum bound states very difficult. The primary reason for this is the weakness of the gravitational field compared to the electromagnetic and nuclear forces.

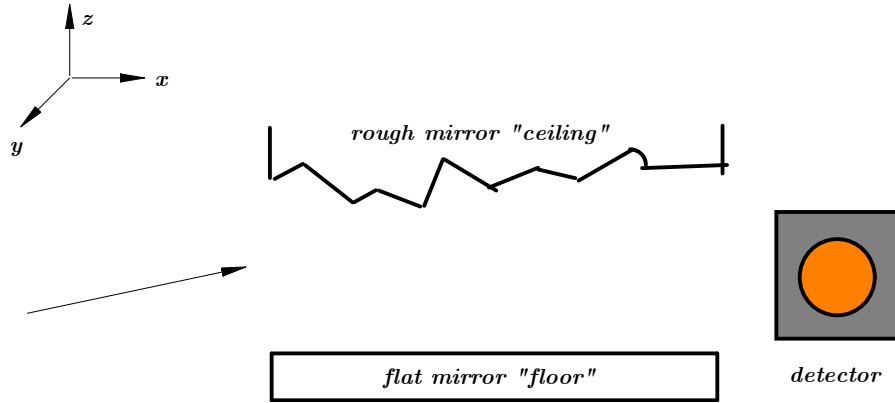


Figure 1.1. Sketch of the experimental cell with a neutron beam between two plates. The neutrons bounce between the "rough" ceiling and "smooth" floor. The neutrons with low vertical velocity, which do not reach the ceiling get to the detector.

The first experimental observation of quantum mechanical bound states of neutrons in the Earth's gravitational field was made by *Nesvizhevsky et al.* in 2002 [[14]-[24]] after a series of experiments in high precision neutron gravitational spectrometry (GRANIT). The GRANIT experiment uses the fact that neutrons have a relatively long lifetime by sending a collimated beam of UCN to the cell through a long complicated waveguide with reflective walls.

One can visualize in a simple way the observation of gravitationally induced quantum states of UCN experiment. There is a collimated beam entering an experimental cell (see Fig.1.1) consisting of a smooth "floor" and a rough "ceiling". More details of the GRANIT experiment will be discussed below [[14]-[24]].

More explicitly, we have a collimated beam of UCN with a large horizontal velocity on the order of $\sim (5 - 15)\text{m/s}$ and a small vertical velocity of a few cm/s

propagating between two parallel horizontal sapphire mirrors. The bottom mirror or "floor" is made as close to perfect as possible. This ensures high probability of specular reflection for the bouncing neutrons. The upper mirror or "ceiling" has a rough surface which is made rough by simply scratching the surface [[16],[61]] . This rough mirror effectively serves as a selector for the vertical component of the velocity of the neutrons. The scattering by the rough ceiling makes the velocity vector turn, which increases the vertical component of velocity and, therefore, the probability of absorption of the neutrons by the wall material. When the vertical velocity exceeds a certain critical value (~ 4 m/s) as a result of scattering by roughness, the neutrons penetrate the wall and disappear. Only the neutrons with a low vertical velocity do not reach the rough ceiling, do not scatter and, therefore, survive.

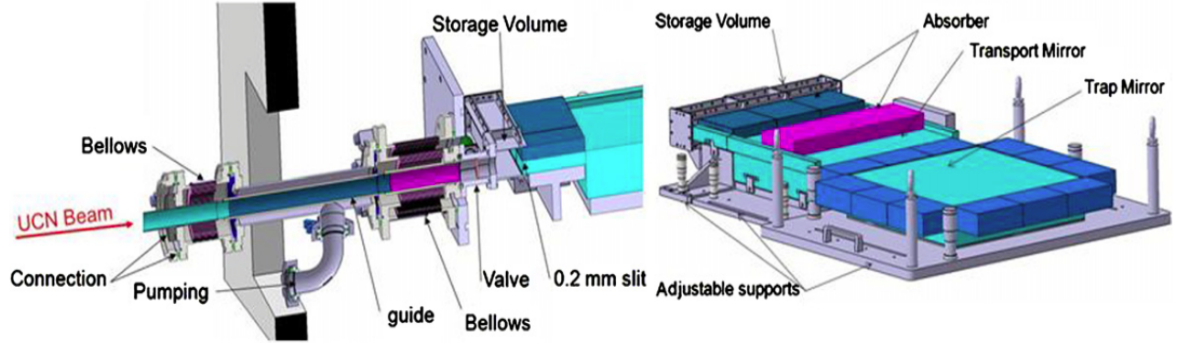


Fig. 6. From the source (left) to the trap (right): UCN guide, UCN valve, intermediate UCN storage, UCN extraction system, UCN storage trap.

Figure 1.2. The GRANIT experiment: a more technical sketch of the experiment as a whole. The experimental cell is on the right.

The location of the waveguide is in the uppermost part of the spectrometer. The reason for this is to isolate it from the effects of external vibrations and from electromagnetic fields. The mirrors in the waveguide can be moved or even interchanged. The positions can be adjusted vertically and horizontally depending on what is needed in the experiment [[23]-[25]]. The configuration that we use in this thesis is the one shown in the figure above in which the edges of the mirrors are perfectly aligned and are of the order of 10cm long. The length represents the minimum horizontal distance covered by the UCN inside the cell; the estimated flight time is about 20 ms. Additionally, the vertical separation between the mirrors (the width of the waveguide H) can be changed. The minimal width of the waveguide is $\sim 15 \mu\text{m}$, which is comparable to the semi-classical amplitude of the bounces of UCN in the ground state. The quantization of the UCN by the Earth's

gravitational field translates into the quantization of the amplitudes of the bounces from the floor mirror.

Ideally, the neutron count at the location of the detector should be a step function of the width H of the waveguide. The reason why we should have a stepwise type function is because of the quantum size effect. The quantum size effect occurs from a gravity-induced perpendicular quantization of the motion to the bottom of the mirror, and leads to a split in the energy spectrum into mini-bands. It is interesting to note that the sharpness of the quantum size effect in neutron count is related to the increase in roughness of amplitude l rather than the correlation radius of roughness R (see below).

The roughness of the imperfections of the ceiling mixes the gravitational states and broadens the energy levels. Below, we provide a quantitative description of the roughness parameters governing the surface inhomogeneities.

1.2.2. Experimental Analysis of the Mirror Roughness

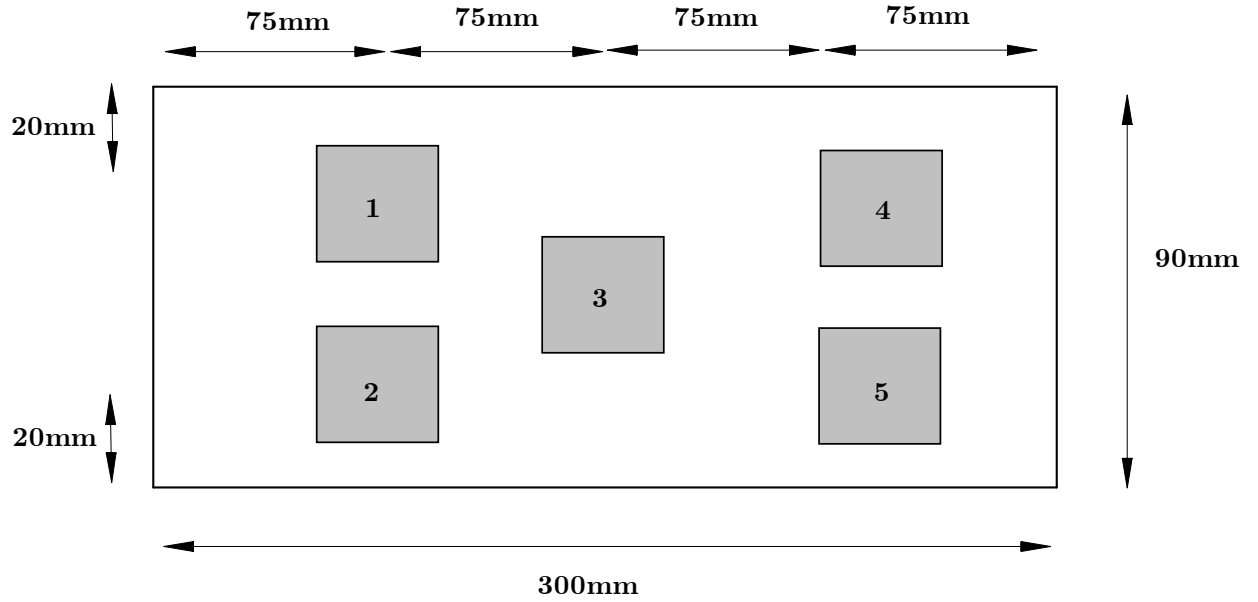


Figure 1.3. "Rough" ceiling mirror. The patches 1-5 represent the spots where the roughness has been measured using vertical scanning interferometry.

One of the main goals of the GRANIT project is to continuously refine the observation of the UCN spectrum. Since the first experiments in 2002, there have been improvements made to the GRANIT spectrometer in order to reduce uncertainties in the waveguide. Various parameters such as the correlation radius of roughness R , amplitude of roughness l , and the oscillation frequency for neutrons in the gravitational well τ_0 have been adjusted and measured more accurately. The latest improvement was the installation of a new large rough mirror on the "ceiling".

The dimensions of the mirror are shown in the Fig.[1.3]. The UCN are propagated along the 90mm long edge. The five square patches in the figure represent

the areas where the mirror roughness has been measured. Each patch in the Figure represents $0.504 \times 0.504 \text{ mm}^2$ and consists of a matrix of $\sim 2500 \times 2500$ experimental data points for which the surface position with respect to a mean reference plane was measured. The surface roughness was measured using Vertical Scanning Interferometry (VSI) technique. The surface was scanned using a light source that splits into two coherent light beams. One of the two beams is sent towards a mirror which is coupled with a different light beam that has been reflected from a sample (amplitude of roughness of 0.5 \AA). The interference patterns are then analyzed using a CCD camera and provide a surface profile. Unfortunately however, this technique is not perfect. For example, the measurement fails if some peak is too sharp and therefore the beam doesn't reflect back onto the detector. The experimental data on the surface profile were analyzed numerically. It was determined that the roughness correlation function most likely has an exponential shape. [9]

This technique though is more appropriate than other scanning techniques such as the Atomic Force Spectroscopy. One of the reasons that VIS is better is that the scanned surface is considerably larger than the correlation radius.

1.3. Notations and Dimensionless Variables

For the purpose of this work it is useful to introduce some uniform notations for the calculations in both presence and absence of gravitational field. Some of the parameters below will be used to make the equations dimensionless. We are looking at the effects of gravity on the transport of the UCN.

1. In this case it is useful to measure all lengths in units of:

$$(1.1) \quad l_0 = \left(\frac{\hbar}{2m^2g} \right)^{1/3} \approx 5.87 \text{ } \mu\text{m},$$

This is the amplitude of the particle bouncing in the lowest quantum state in the presence of the Earth gravitational field.

2. The energy scale is defined by:

$$(1.2) \quad e_0 = mgl_0 \sim 0.602 \text{ peV},$$

This is the gravitational energy of the neutron in the ground state.

3. The velocity scale is defined by:

$$(1.3) \quad v_0 = \sqrt{2gl_0} = \frac{\hbar}{ml_0} \sim 1.1 \times 10^{-2} \text{ m/s}.$$

4. The time scale is given by:

$$(1.4) \quad \frac{1}{\tau_0} = \frac{\sqrt{2\pi} \hbar}{4m l_0^2} \sim 1149 \text{ s}^{-1}.$$

This is roughly the frequency of bounces in the lowest state.

5. The width of the waveguide H in units of l_0 is:

$$(1.5) \quad h = \frac{H}{l_0}.$$

6. The roughness correlation radius R expressed as a dimensionless variable is:

$$(1.6) \quad r = \frac{R}{l_0}.$$

7. Similarly, the amplitude of roughness l as a dimensionless variable is expressed as:

$$(1.7) \quad \eta = \frac{l}{l_0}.$$

8. The quantized energy levels E_j of the ultra-cold neutrons in the gravitational well are given by:

$$(1.8) \quad \lambda_j = \frac{E_j}{e_0}.$$

9. The absorption threshold U_c of the mirror material is given by:

$$(1.9) \quad u_c = \frac{U_c}{e_0},$$

where $U_c \approx 100$ neV, and, therefore, $u_c \approx 1.4 \times 10^5$.

10. The flight time for the ultra-cold neutrons through the waveguide of the length L is given by:

$$(1.10) \quad \tau_L = \frac{L}{v_x},$$

In experimental conditions $\tau_L \approx 2 \times 10^{-2}$ s. In dimensionless units $\tau_L/\tau_0 \approx 26$.

11. The neutron momenta are measured in units of:

$$(1.11) \quad q_0 = \frac{\hbar}{l_0}.$$

1.4. Theoretical Background

1.4.1. Quantum Size Effect (QSE)

Ultra-cold neutrons (UCN) are longwave particles. We are looking at UCN in narrow waveguides in which the width is comparable to the wavelength and the motion across the waveguide is quantized. This QSE automatically discretizes the initially continuous equations. This quantization turns out to be very fortuitous as it helps in numerical calculations: if we were working with a continuous system, we would need to discretize the problem anyway. QSE leads to a split of the energy spectrum $\epsilon(\mathbf{p})$ into a set of minibands $\epsilon_j(\mathbf{q})$ such that $\epsilon(p_x, \mathbf{q}) \longrightarrow \epsilon_j(\mathbf{q})$, where \mathbf{p} is the 3D momentum, and \mathbf{q} is the 2D momentum in the plane of the surface.

More explicitly, an initially parabolic spectrum, $\epsilon(\mathbf{p}) = p^2/2m$ becomes

$$(1.12) \quad \epsilon_j(\mathbf{q}) = \frac{1}{2m} \left[\left(\frac{\pi \hbar j}{H} \right)^2 + q_j^2 \right]$$

and the 2D momentum for miniband j becomes

$$(1.13) \quad q_j^2 = \left[2mE - \left(\frac{\pi \hbar j}{H} \right)^2 \right]$$

where E is the overall kinetic energy of particles, m is the mass of the neutrons, H is the width of the channel.

In an ideal waveguide, the quantum levels are well defined and the states are not mixing. Scattering by random surface inhomogeneities leads to inter- and intraband transitions and eventually mixes and broadens the quantum states.

Sometimes, as in experiments performed at ILL (Grenoble), the waveguides, or, more precisely, one of the neutron mirrors, are made rough on purpose.

1.4.2. Transport Equation

Studies on the effect of random surface roughness on wave or particle scattering describe the diffusion flows of UCN along a rough waveguide. *Meyerovich et al.* [[1]-[8]] developed a rigorous theoretical framework of quantum transport theory in system with random rough boundaries. This framework incorporates the boundary scattering directly into the bulk transport equation. It includes the roughness of the walls explicitly into the roughness-driven transition probabilities between quantum states. The transport equation for distribution functions $n_j(\mathbf{q})$ in a miniband j has the form

$$(1.14) \quad \frac{dn_j}{dt}(\mathbf{q}) = 2\pi \sum_{j'} \int W_{jj'}(n_j - n_{j'}) \delta(\epsilon_{j\mathbf{q}} - \epsilon_{j'\mathbf{q}'}) \frac{d^2\mathbf{q}'}{(2\pi)^2}$$

where $n_j(\mathbf{q})$ is the distribution function of the particles, $\epsilon_{j\mathbf{q}}$ is the energy spectrum, \mathbf{q} is the momentum in the plane parallel to the surface, and $W_{jj'}(\mathbf{q}, \mathbf{q}')$ are the scattering-driven probabilities of transitions between the states $\epsilon_j(\mathbf{q})$ and $\epsilon_{j'}(\mathbf{q}')$.

The probabilities of direct transitions from the lowest states to the continuous spectrum above the threshold U_c are negligible and such transitions can be disregarded. After integration over the energies, the transport equation acquires the following form:

$$(1.15) \quad \frac{\partial N_j}{\partial t} = \frac{m}{2\pi} \sum_{j'} \int d\theta W_{jj'}(|\mathbf{q}_j - \mathbf{q}_{j'}|) (N_{j'} - N_j)$$

where N_j is the number of neutrons in the state j , and θ is the angle between \mathbf{q}_j and $\mathbf{q}_{j'}$.

Our goal is to find the diffusion coefficient and the mean-free path, which is proportional to the diffusion coefficient. After standard transformations (a more detailed derivation can be found in the Appendices) the transport equation reduces to a set of linear equations for $\nu_j(q_j)$:

$$(1.16) \quad Q_j = -m \sum_{j'} \frac{\nu_{j'}(q_{j'})}{\tau_{jj'}},$$

Here Q_j is the momentum, the transition times $\tau_{jj'}$ are given below by Eq.(1.24), and ν_j is the first angular harmonic of the distribution function $n_j^{(1)} = \nu_j \delta(\epsilon - \epsilon_F)$

at $q = q_j$, Ref. [[4],[5]]. The equations can be made dimensionless using

$$(1.17) \quad q_j q_0 = -m \sum_{j'} \frac{\tilde{\nu}_{j'} \nu_0}{\tilde{\tau}_{jj'} \tau_0}$$

which leads to

$$(1.18) \quad q_j = -\frac{m\nu_0}{q_0\tau_0} \sum_{j'} \frac{\tilde{\nu}_{j'}}{\tilde{\tau}_{jj'}},$$

where

$$(1.19) \quad q_j = \frac{Q_j}{q_0}, \quad \tilde{\nu}_j = \frac{\nu_j}{\nu_0} \quad \text{and} \quad \tilde{\tau}_{jj'} = \frac{\tau_{jj'}}{\tau_0}.$$

Finally, the dimensionless transport equation acquires the form:

$$(1.20) \quad q_j = -\frac{ml_0^2}{\hbar\tau_0} \sum_{j'} \frac{\tilde{\nu}_{j'}(q_{j'})}{\tilde{\tau}_{jj'}}.$$

1.4.3. Transition Probabilities

The roughness-driven transition probabilities between quantized states have the following form:

$$(1.21) \quad W_{jj'} = \zeta |\psi_j(h)|^2 |\psi_{j'}(h)|^2 U_c^2$$

if the absorption threshold U_c is finite. Alternatively,

$$(1.22) \quad W_{jj'} = \frac{1}{4m^2} \zeta |\psi'_j(h)|^2 |\psi'_{j'}(h)|^2$$

when the absorption threshold $U_c \rightarrow \infty$. Here j and j' are the miniband indices, ζ is the correlation function of surface homogeneities (see below), $\psi_j(h)$ is the wavefunction at the surface.

In the case of the square well potential this equation becomes the following :

$$(1.23) \quad W_{jj'}(\mathbf{q}, \mathbf{q}') = \frac{\hbar}{m^2 L^2} \zeta \left(\frac{\pi \hbar j}{L} \right)^2 \left(\frac{\pi \hbar j'}{L} \right)^2.$$

The transitions times in the transport equation are directly related to the angular harmonics of these transition probabilities as follows:

$$(1.24) \quad \frac{2}{\tau_{jj'}} = m \sum_{j''} \left[\delta_{jj'} W_{jj''}^{(0)} - \delta_{j'j''} W_{jj'}^{(1)} \right]$$

1.4.3.1. Correlation Function of Roughness. The correlation function of surface roughness (CF) is defined as:

$$(1.25) \quad \zeta(|\mathbf{s}|) = \langle \xi(\mathbf{s}_1) \xi(\mathbf{s}_1 + \mathbf{s}) \rangle \equiv A^{-1} \int \xi(\mathbf{s}_1) \xi(\mathbf{s}_1 + \mathbf{s}) d\mathbf{s}_1,$$

$$(1.26) \quad \zeta(|\mathbf{p}|) = \int d^2 s e^{i\mathbf{q}\cdot\mathbf{s}} \zeta(|\mathbf{s}|) = 2\pi \int_0^\infty \zeta(s) J_0(qs) s ds,$$

where $\xi(|\mathbf{s}|)$ is the exact profile of the wall and A is the area over which the averaging is done. The mathematical form of the CF cannot be found theoretically except in very few instances in which we have exactly solvable models of surface

roughness. It is usually assumed that the CF has the following general form:

$$(1.27) \quad \zeta(x) = l^2 \varphi(x/R)$$

with some function $\varphi(x/R)$, where l and R are the average amplitude and correlation radius. However, nothing prevents the CF to acquire a more complicated form, for example, with several correlation scales R_c . In calculations we assume that we know the shape of the CF. The most commonly used correlation functions have either the Gaussian

$$(1.28) \quad \zeta(s) = l^2 \exp(-s^2/2R^2),$$

$$(1.29) \quad \zeta(q) = 2\pi l^2 R^2 \exp(-q^2 R^2/2),$$

or exponential

$$(1.30) \quad \zeta(s) = l^2 \exp(-s/R)$$

$$(1.31) \quad \zeta(q) = \frac{2\pi l^2 R^2}{(1 + q^2 R^2)^{3/2}}$$

forms. Sometimes people also use a CF with a power law shape. Here R is the correlation radius of surface inhomogeneities., $r = R/l_0$, and the dimensionless

amplitude is defined as $\eta = l/l_0$. There are reasons to believe that the correlation function in Grenoble experiments might be exponential, Ref. [[9]].

The angular harmonics of the Gaussian correlation function are

$$(1.32) \quad \zeta^{(0)} = 4\pi l^2 R^2 \left[e^{-qq' \cdot r^2} I_0(qq' \cdot r^2) \right] e^{-r^2/2(q-q')^2}$$

$$(1.33) \quad \zeta^{(1)} = 4\pi l^2 R^2 \left[e^{-qq' \cdot r^2} I_1(qq' \cdot r^2) \right] e^{-r^2/2(q-q')^2}$$

This means the transition probabilities W , Eq(1.23), are equal to Ref. [[4]]:

$$(1.34) \quad W_{jj'}^{(0)} = \frac{\hbar}{m^2 L^2} \left(\frac{\pi j}{L} \right)^2 \left(\frac{\pi j'}{L} \right)^2 4\pi l^2 R^2 \left[e^{-qq' \cdot r^2} I_0(qq' \cdot r^2) \right] e^{-r^2/2(q-q')^2}$$

$$(1.35) \quad W_{jj'}^{(1)} = \frac{\hbar}{m^2 L^2} \left(\frac{\pi j}{L} \right)^2 \left(\frac{\pi j'}{L} \right)^2 4\pi l^2 R^2 \left[e^{-qq' \cdot r^2} I_1(qq' \cdot r^2) \right] e^{-r^2/2(q-q')^2}$$

In dimensionless variables,

$$(1.36) \quad w_{jj'}^{(0)} = \frac{8\pi r^2}{\sqrt{2\pi h}} \left(\frac{\pi j}{h} \right)^2 \left(\frac{\pi j'}{h} \right)^2 \left[e^{-qq' \cdot r^2} I_0(qq' \cdot r^2) \right] e^{-r^2/2(q-q')^2}$$

$$(1.37) \quad w_{jj'}^{(1)} = \frac{8\pi r^2}{\sqrt{2\pi h}} \left(\frac{\pi j}{h} \right)^2 \left(\frac{\pi j'}{h} \right)^2 \left[e^{-qq' \cdot r^2} I_1(qq' \cdot r^2) \right] e^{-r^2/2(q-q')^2}$$

where the dimensionless roughness parameters and r and η can be used as free parameters in the identification of surface correlations. These two parameters are often sufficient to describe the surface roughness.

The dimensionless transition probabilities for exponential roughness can be written as

$$(1.38) \quad \Omega = 2r \sqrt{\frac{qq'}{1 + r^2 (q + q')^2}}$$

$$(1.39) \quad w_{jj'}^{(0)} = \frac{32r^2\eta^2}{\sqrt{2\pi}h^2} \left(\frac{\pi j}{h}\right)^2 \left(\frac{\pi j'}{h}\right)^2 \frac{E(\Omega)}{\left(1 + r^2 (q - q')^2 \sqrt{1 + r^2 (q + q')^2}\right)}$$

$$(1.40) \quad w_{jj'}^{(1)} = \frac{32r^2\eta^2}{\sqrt{2\pi}h^2} \left(\frac{\pi j}{h}\right)^2 \left(\frac{\pi j'}{h}\right)^2 \frac{(1 + r^2 (q + q')^2) E(\Omega) - (1 + r^2 (q - q')^2) K(\Omega)}{\left(1 + r^2 (q - q')^2 \sqrt{1 + r^2 (q + q')^2}\right)}$$

The diffusion of ultra-cold neutrons displays a strong directional upward bias in terms of the transitions between $j \rightarrow j'$. This bias is due to the rapid growth of the product of the wavefunctions on the boundary $|\psi_j(h)|^2 |\psi_{j'}(h)|^2$. This allows a growth of roughly as $j^2 j'^2$, see Eq.(1.23). There are two main consequences of this bias. The first one being that the strong upward bias may allow one to neglect particles returning back to the lowest states. And the second consequence is that the time necessary for a neutron in one of the lowest gravitational states to

diffuse upward towards the absorption barrier is spent almost entirely on the first transition.

In the next chapter we will examine more closely the process of diffusion, and expand upon and develop a more detailed theoretical approach.

CHAPTER 2

Diffusion Coefficient and Mean Free Path in a Rough Waveguide

2.1. Introductory Comments

Let us examine the transition probabilities which for the sake of the numerical computations need to be made dimensionless. Furthermore, we are going to define some parameters used in the numerical computations. In the context of our research, we want to look at both Gaussian and exponential roughness associated with the correlation functions ζ , which together with the wavefunctions at the wall form the transition probabilities, Eq.(1.36)-Eq.(1.37) , and Eq.(1.39)- Eq.(1.40).

The transition probabilities are proportional to the square of the amplitude of roughness η . Therefore, the scaling of the results with the roughness amplitude η is trivial and in most of the computations we simply assume $\eta = 1$. The scaling of the results with the correlation radius $r = R/l_0$ is complicated and is not known beforehand. One of our main goals is to find out the dependence of the diffusion parameters on r .

In relevant experiments the width of the channels leading to the cell is $H = 50 \mu\text{m}$, and the particle energy is $E = 150 \text{ neV}$; this makes $h = 8.52$, and $e = 2.49 \cdot 10^5$. The highest occupied quantum level j_{max} satisfies the inequality,

$$(2.1) \quad e - \frac{\pi^2 j_{\max}^2}{h^2} \geq 0$$

Solving for j_{\max} we get

$$(2.2) \quad j_{\max} = \sqrt{\frac{eh^2}{\pi^2}} = 1352$$

which means that the transport equation in this case reduces to a set of 1352 coupled equations.

2.2. The Diffusion Coefficient

The main purpose of this section of the work was to find the diffusion coefficient and the mean free path for UCN in rough channels. We are trying to examine how the diffusion coefficient changes under different conditions. More explicitly, we are interested in its dependence on r . Diffusion is a process that originates from random motion of particles when there is a net flow from one region to another. As a result, in our case, in the presence of a concentration gradient $\nabla\rho$ the diffusion equation reduces to

$$(2.3) \quad \frac{1}{Sm} \nabla\rho * Q_j = - \sum_{j'} \frac{v_{j'}}{\tau_{jj'}},$$

where ρ is the particle density. Its concentration gradient $\nabla\rho$ is a simple scaling parameter, which, in the end, cancels out from the equation for the diffusion coefficient. After this cancellation, the diffusion coefficient D becomes

$$(2.4) \quad D = -\frac{1}{m} \sum_{j'} Q_{j'} \nu_{j'}$$

The dimensionless diffusion coefficient

$$d = D/d_0 = \sum_{j'} d_j,$$

$$d_j = q_j \tilde{\nu}_j,$$

$$d_0 = \hbar/m = 6.3 \cdot 10^{-8} m/s^2.$$

The dimensionless distributions $\tilde{\nu}_j = \nu_j/l_0$ are obtained from numerically solving the transport equation.

2.3. Mean Free Path

We also want to calculate the particle mean-free path (MFP) in a rough waveguide. The mean free path in very basic terms is the average distance traveled between collisions. Here we define it with respect to the diffusion coefficient as

$$(2.5) \quad \mathcal{L} = D/v,$$

where v is the velocity. The dimensionless velocity

$$\tilde{v} = \frac{1}{v_0} \sqrt{\frac{2e_0}{m}} \sqrt{e}$$

where $v_0 = 1.5 \cdot 10^{-2} m/s$. The dimensionless mean free path $\ell = \mathcal{L}/l_0$,

$$\ell = \frac{2d_0}{l_0 v_0} \frac{d}{\tilde{v}} = \frac{2d_0}{l_0} \sqrt{\frac{m}{2e_0}} \frac{d}{\sqrt{e}}.$$

As one can clearly see the MFP is intimately related to the diffusion coefficient.

2.4. Numerical Results

Before presenting the results, let us summarize the dimensionless equations from above. The transport equation ,

$$(2.6) \quad q_j = -\frac{ml_0^2}{\hbar\tau_0} \sum_{j'} \frac{\tilde{v}_{j'}(q_{j'})}{\tilde{\tau}_{jj'}},$$

contains the transition times

$$(2.7) \quad \frac{2}{\tilde{\tau}_{jj'}} = m \sum_{j''} \left[\delta_{jj''} w_{jj''}^{(0)} - \delta_{j'j''} w_{jj'}^{(1)} \right].$$

The dimensionless harmonics of the transition probabilities for the exponential and Gaussian roughness correlators are given in explicit detail in the Appendix A.

For the overall and "partial" diffusion coefficients d and d_j the dimensionless equations are as follows

$$d = D/d_0 = \sum_{j'} d_j,$$

$$d_j = q_j \tilde{\nu}_j.$$

Finally, the MFP is

$$(2.8) \quad \ell = \frac{2d_0}{l_0} \sqrt{\frac{m}{2e_0}} \frac{d}{\sqrt{e}}.$$

Using the dimensionless equations for the transition probabilities from the previous section, we are now able to perform computations to get the diffusion coefficient and MFP. The computations are done in *Mathematica*, where we use the function **LinearSolve** [**m**,**b**] which finds an **x** that solves the matrix equation **m.x==b.** to get the ν values. This is the part of the program that is computationally the longest as it essentially solves a system of 1352 linear equations with complicated coefficients and varied parameters. After that, we calculate the dimensionless partial diffusion coefficients,

$$(2.9) \quad d_j = \tilde{\nu}_j q_j$$

and sum them to get the overall diffusion coefficient. We easily get the MFP by using Eq. (2.8).

In our numerical simulations we were using a fixed channel width $h = 8.52$ (the number given to us by GRANIT experimentalists) and were changing the correlation radius of surface inhomogeneities r . Before we go into the descriptions of the various curves, it is important to note that all the curves for $d(r)$ are expected to have the minimum at, approximately, $qr \sim 1$ for both Gaussian and exponential surface correlators. The experimental value of the particle energy is $E = 150$ neV, i.e., $e \approx 2.5 \times 10^5$, which makes $q_1 \approx 500$. This means that the minimum corresponds to very small values of r , $r \sim 0.002$, and cannot be resolved on many of the curves below. The explanation for this minimum is rather simple. The scattering by surface inhomogeneities is most effective at $qr \sim 1$ leading to a minimum in the diffusion coefficient $d(r)$. There could be several small minima at $q_j r \sim 1$ but all corresponding values of r are small. For this reason, below we will show mostly the results for noticeably larger values of r , i.e., to the right of the minimum.

Fig.[2.1] presents $d(r)$ around the minimum. The computation was done for Gaussian inhomogeneities.; the figures for the exponential correlation function look similar (Fig.[2.2]). Note that the values of the correlation radius close to the minimum $r \sim 0.002$ are too small to be studied experimentally.

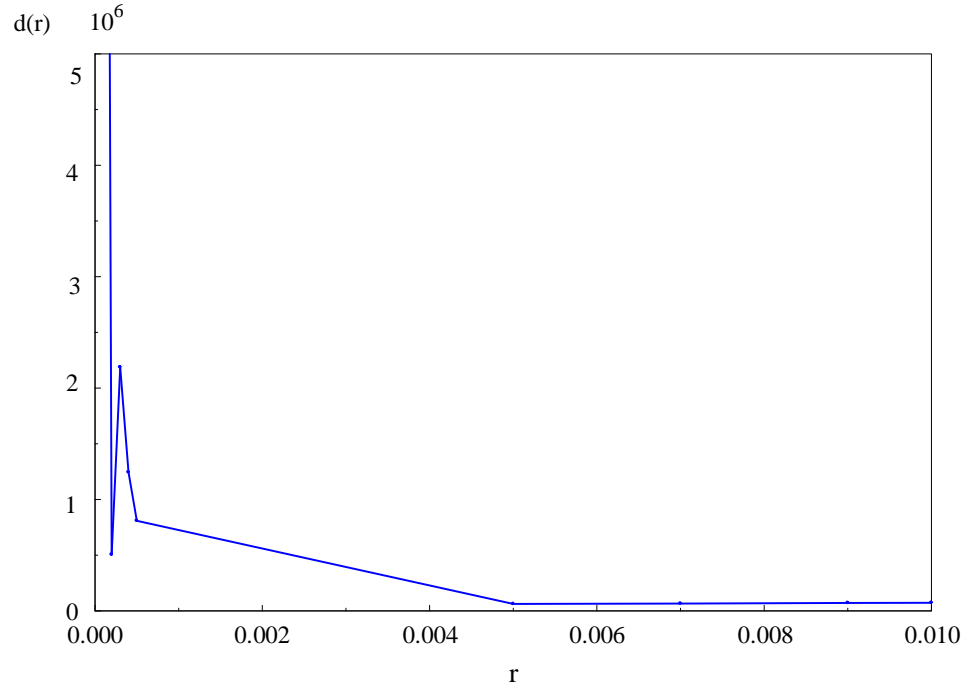


Figure 2.1. Minima of the diffusion coefficient $d(r)$ as a function of the correlation radius for the Gaussian inhomogeneities. The diffusion coefficient starts growing again at larger r .

Fig.[2.3] shows the total diffusion coefficient d as a function of the correlation radius r of Gaussian surface inhomogeneities plotted up to $r = 15$. The minimum $d(r)$ is barely noticeable on this scale. We see that the diffusion coefficient rapidly increases as the correlation radius increases. This is understandable: with increasing r the surface becomes smoother and the effective scattering cross-section decreases.

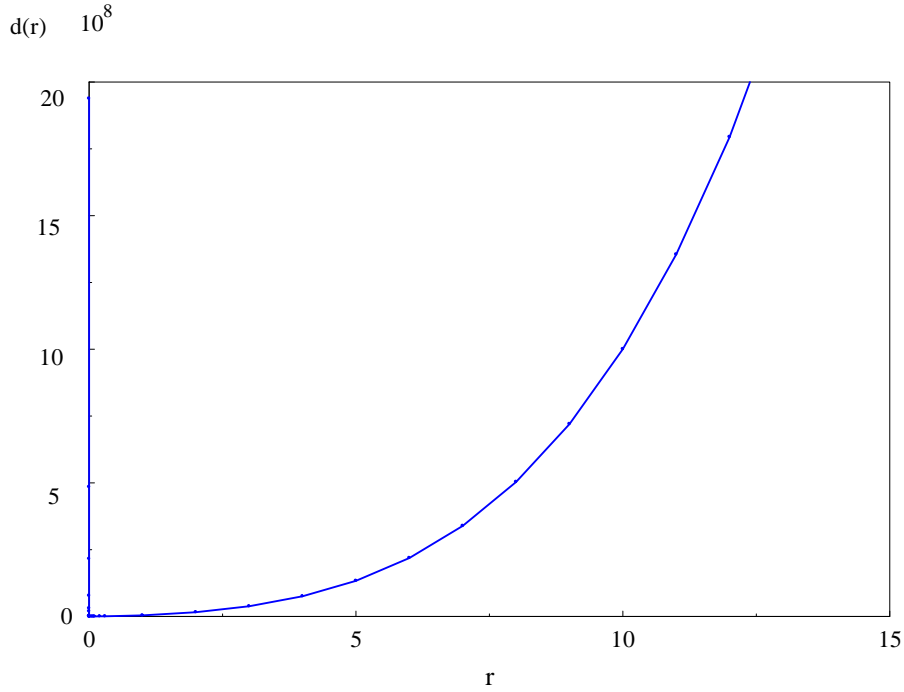


Figure 2.2. Diffusion coefficient $d(r)$ for the Gaussian surface correlator over large range of r . The minima in $d(r)$ cannot be resolved on this scale.

Figures [2.5] and [2.6] show the MFP $l(r)$ for Gaussian and exponential correlation functions of surface inhomogeneities. It is hard to plot the results for the exponential correlator on the same plot with the Gaussian one: $l(r)$ for the exponential correlator increases by orders of magnitude slower than for the Gaussian correlator due to the fact that the Gaussian function is much sharper than the exponential function. However $l(r)$ is increasing for both types of surface correlators. We tested this for several different values of h Fig.[2.8]: the shapes of the curves and the difference between them remained qualitatively the same.

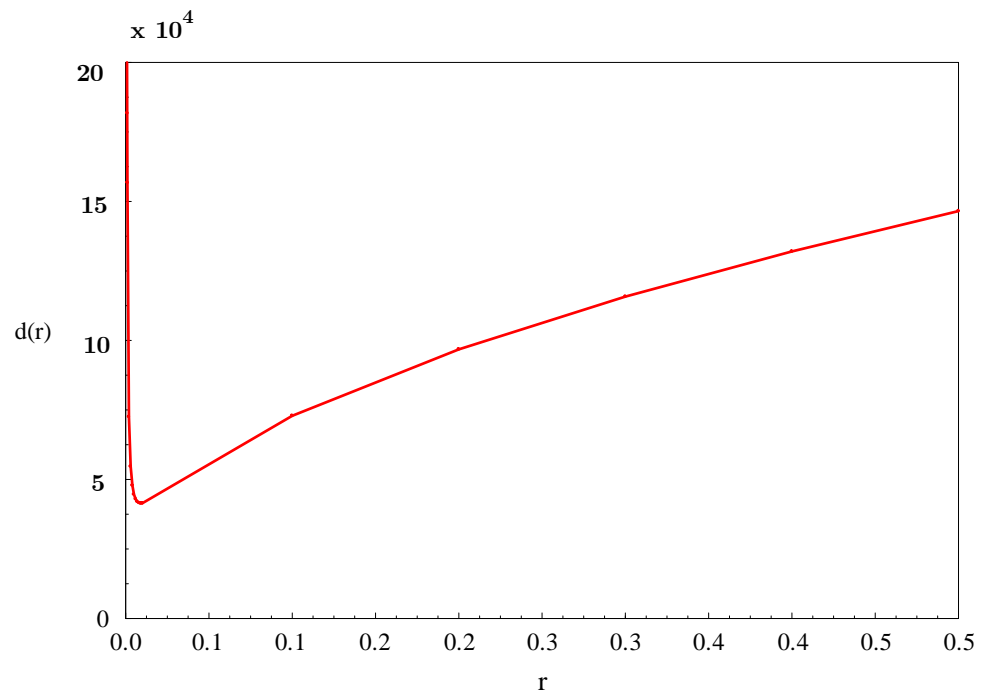


Figure 2.3. The next figure (Fig.[2.4]) shows the diffusion coefficient for the exponential correlation function of surface roughness.

Figure [2.7] compares the MFP for Gaussian and exponential surface correlation functions for a small range of r .

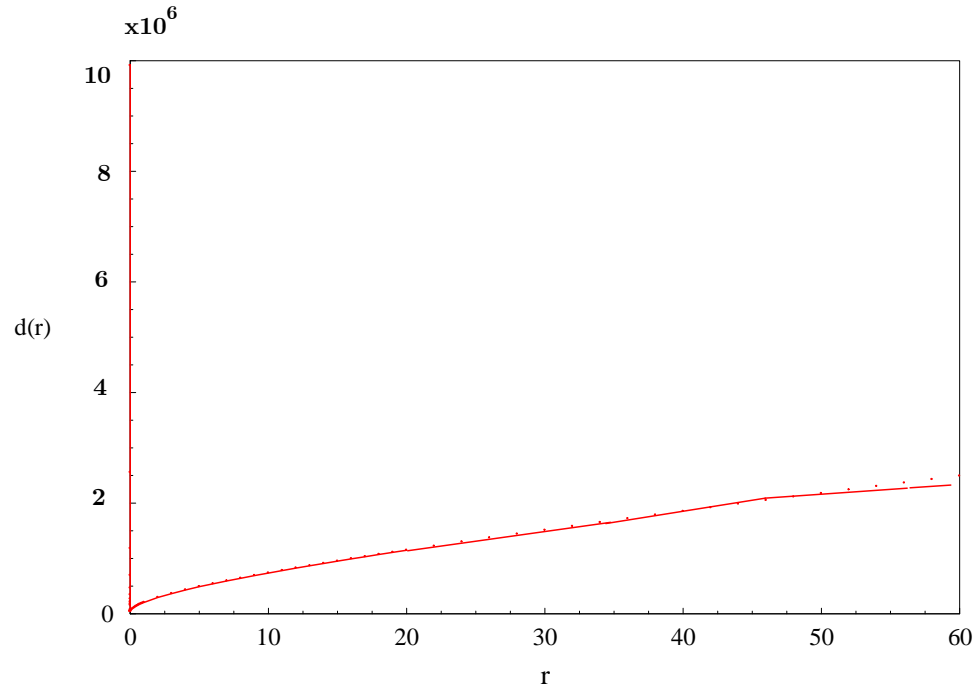


Figure 2.4. Diffusion for the surface inhomogeneities with the exponential correlation function over large range of r .

Similarly, Figure [2.9] illustrates the fact that the MFP $l(r)$ for the Gaussian and exponential correlation functions is more or less the same up to $r \sim 2$. Starting from this point the result for the Gaussian correlation function increases much faster than for the exponential function. We think the reason is that the Gaussian function decays much faster than the exponential which manifests itself at large values of r .

The next few curves, Figures.[2.10 – 2.12], illustrate fitting of the MFP curves for $l(r)$ by the power law functions. If we look at the Gaussian correlation function

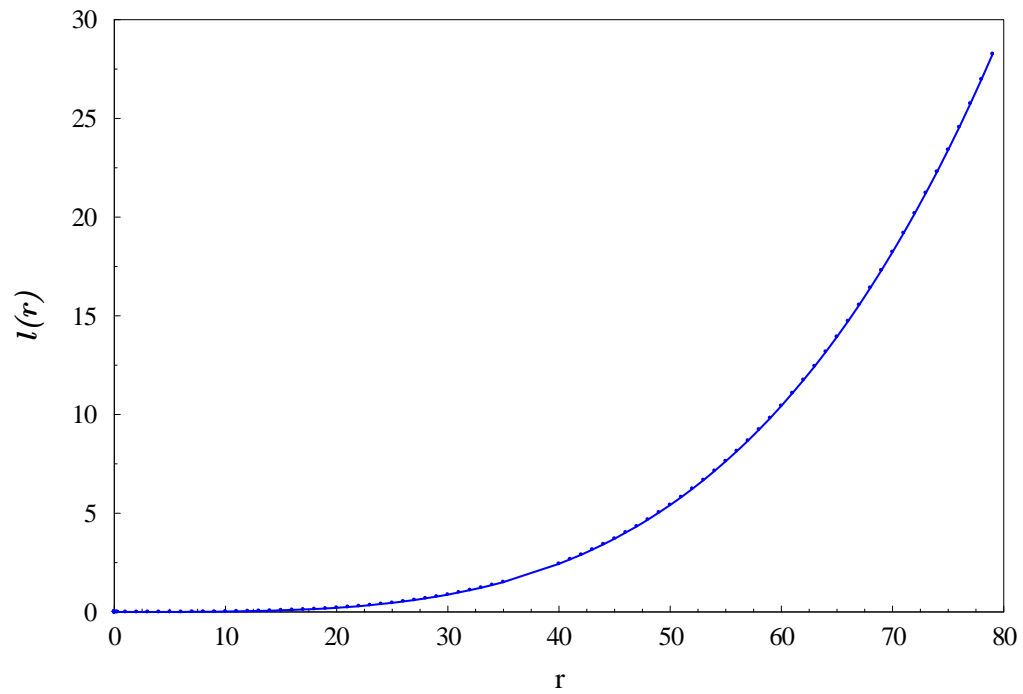


Figure 2.5. Mean free path $l(r)$ for the surface with Gaussian roughness over wider range of r .

$d(r)$ in the ranges of r from 1 to 20 we get a pretty good fit using the power function

$d(r) \propto r^p$ with the index $p = 2.7$.

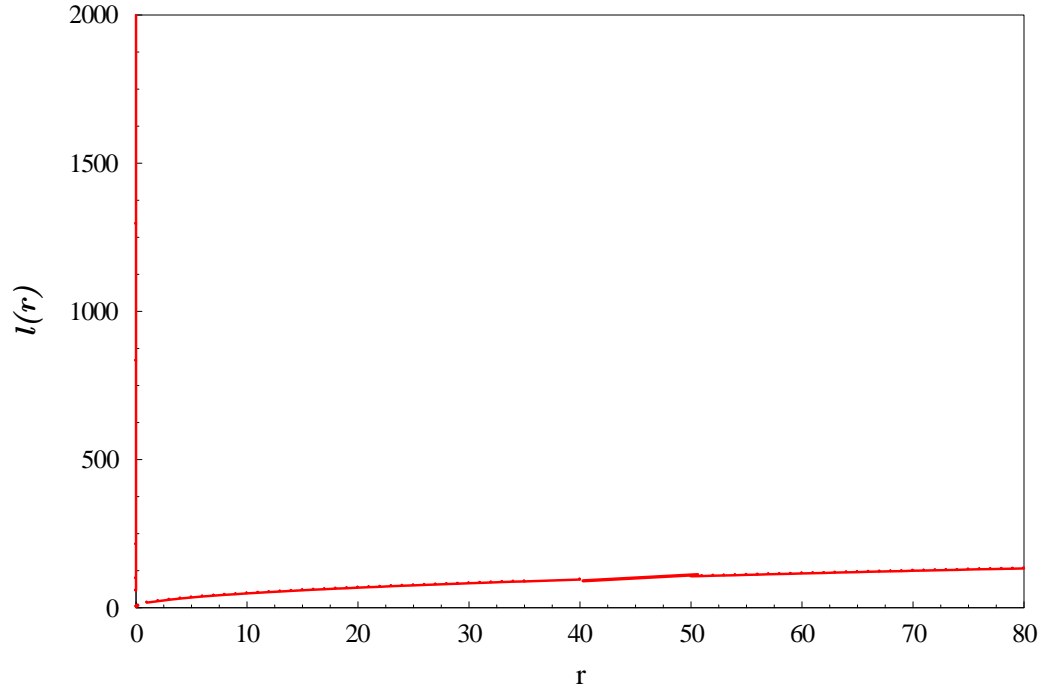


Figure 2.6. Mean free path for the surface with exponential roughness over wider range of r .

Looking at $d(r)$ in the range of $r \sim 20 - 60$, we also get a good fit using the power law, with the power $p = 3.5$. Looking at the exponential correlation function $d(r)$ in the ranges of r from 1 - 40, we see that we get a good fit using the power law, with the power $p = 2.95$.

2.5. Conclusions

- We calculated the diffusion coefficient and the mean free path for ultra-cold neutrons in narrow channels with random rough walls.

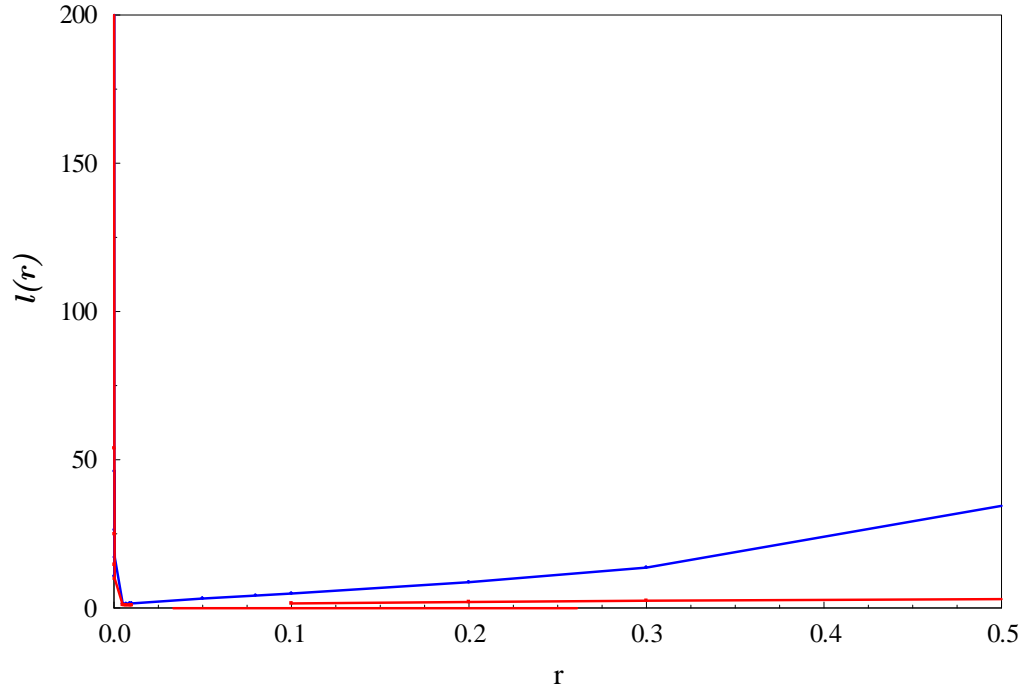


Figure 2.7. Mean-free path $l(r)$ for both Gaussian and exponential correlation functions for small r .

- We have concluded that there is a complicated minimum in $d(r)$ and $\mathcal{L}(r)$ for small correlation radius $r \sim 2 \times 10^{-4}$.
- We have also concluded that the diffusion coefficient and the MFP rapidly increase as the correlation radius r increases, though at different rates depending on the surface correlation function.
- The growth is not monotonic, there is more than one minimum at $q_j \sim 1/r$.
- We compared the behavior of $d(r)$ and $\mathcal{L}(r)$ for surfaces with the Gaussian and the exponential correlation functions of surface roughness.

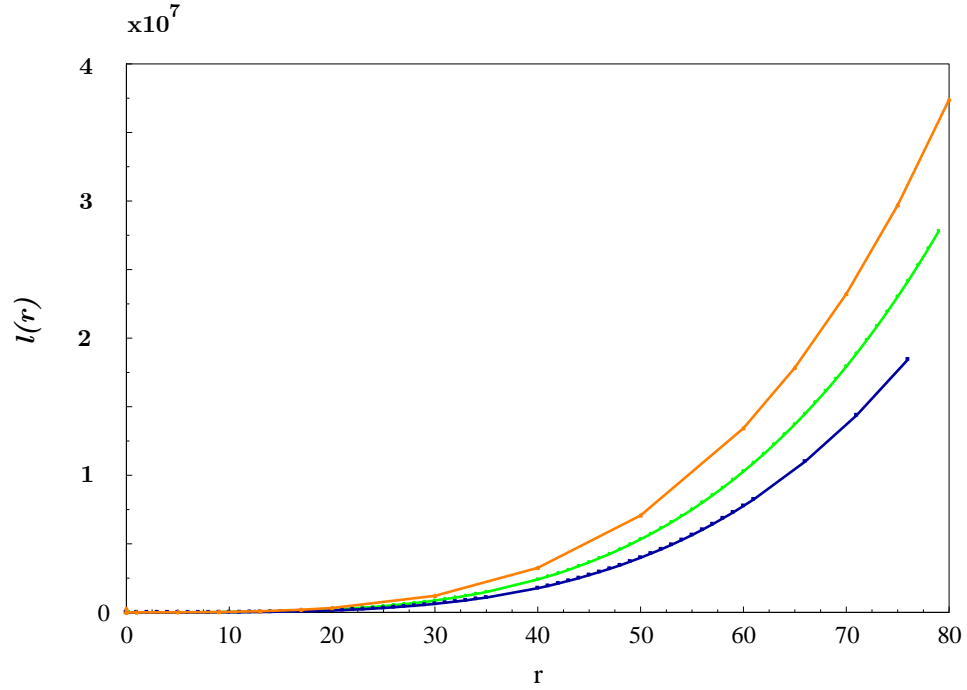


Figure 2.8. MFP for Gaussian correlation function for various channel widths $h = 16, 8, 4$.

- The function $d(r)$ behaves roughly as r^3 , though the exponent slightly drifts with r . This seems to be an important conclusion, though we do not have an explanation for this functional dependence.
- The computations were done for realistic values of the channel width $h = 8.52$. At different values of h the results were qualitatively the same.
- The growth of $d(r)$ and $\mathcal{L}(r)$ for the Gaussian surface correlation function is much slower than for the exponential correlation function.
- If one wants to effectively turn back the neutrons which got into the gaps in the channel junctions, one should make the correlation radius of surface

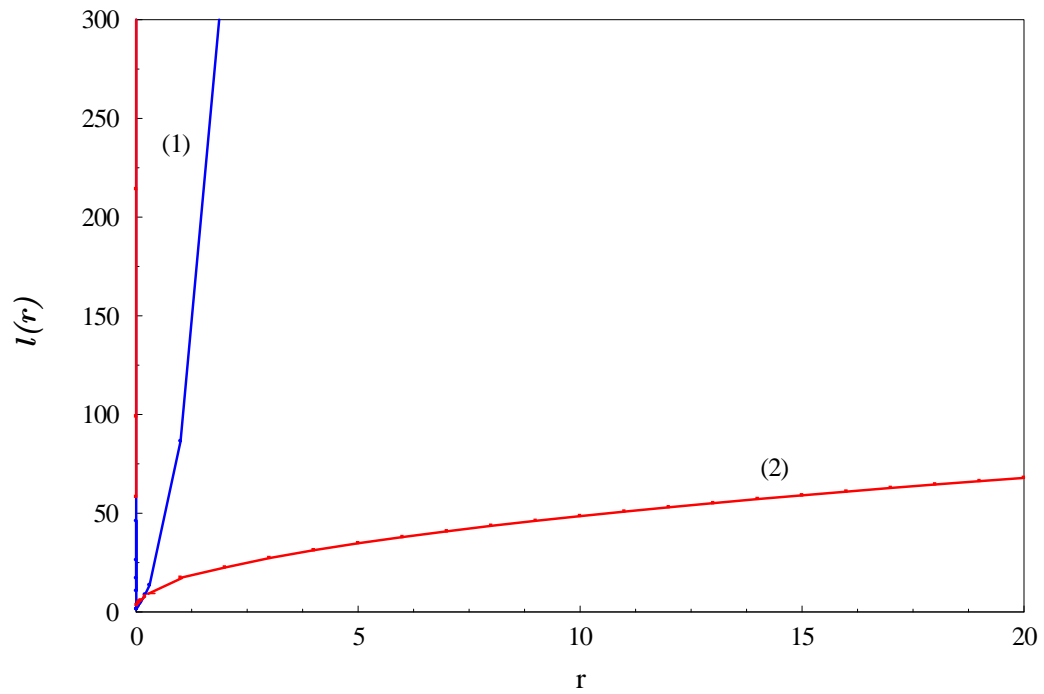


Figure 2.9. MFP for Gaussian (1) and exponential (2) surface correlation functions over a wide range of r .

roughness as small as possible, and, if possible, to have roughness with an exponential correlation function.

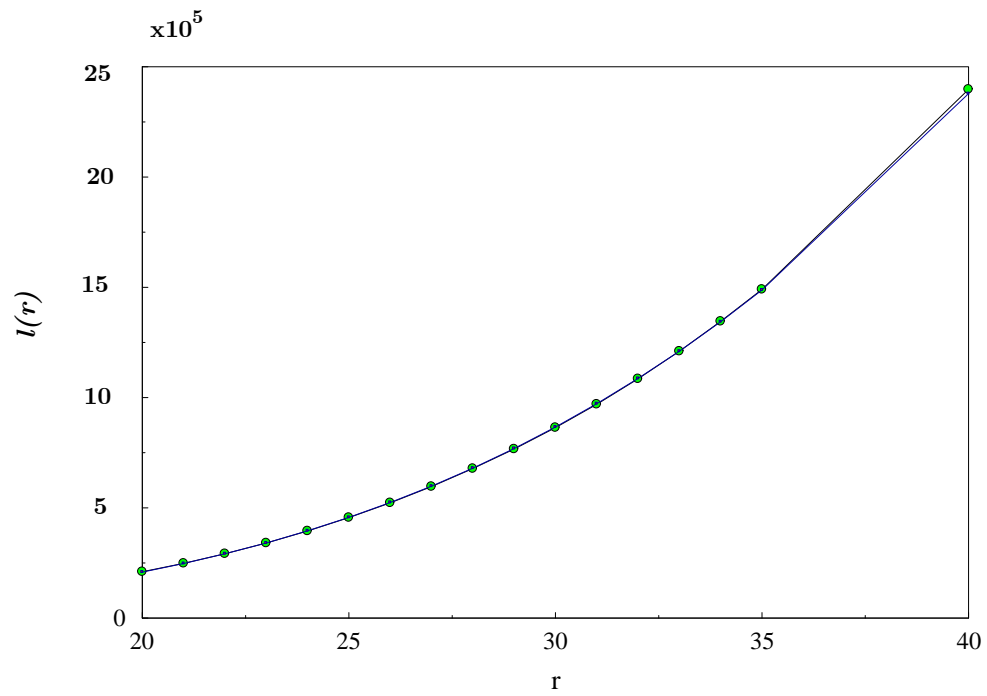


Figure 2.10. Power law fitting for the MFP $l(r)$ surfaces with the Gaussian correlation function for r from 20 to 40.

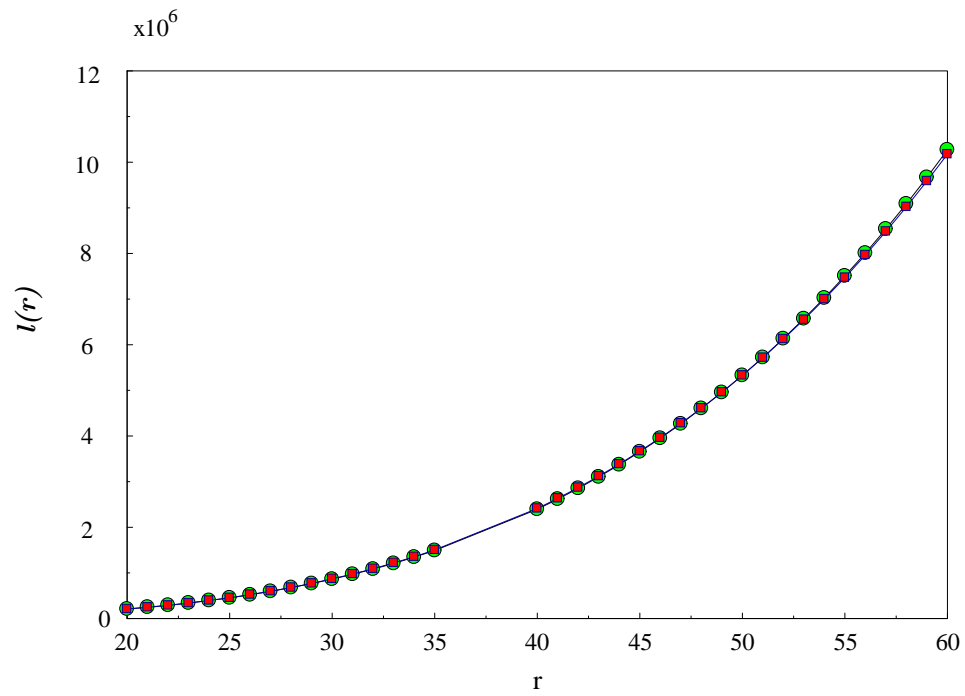


Figure 2.11. The power law fit for MFP $l(r)$ for Gaussian inhomogeneities over the range of r from 40 to 60

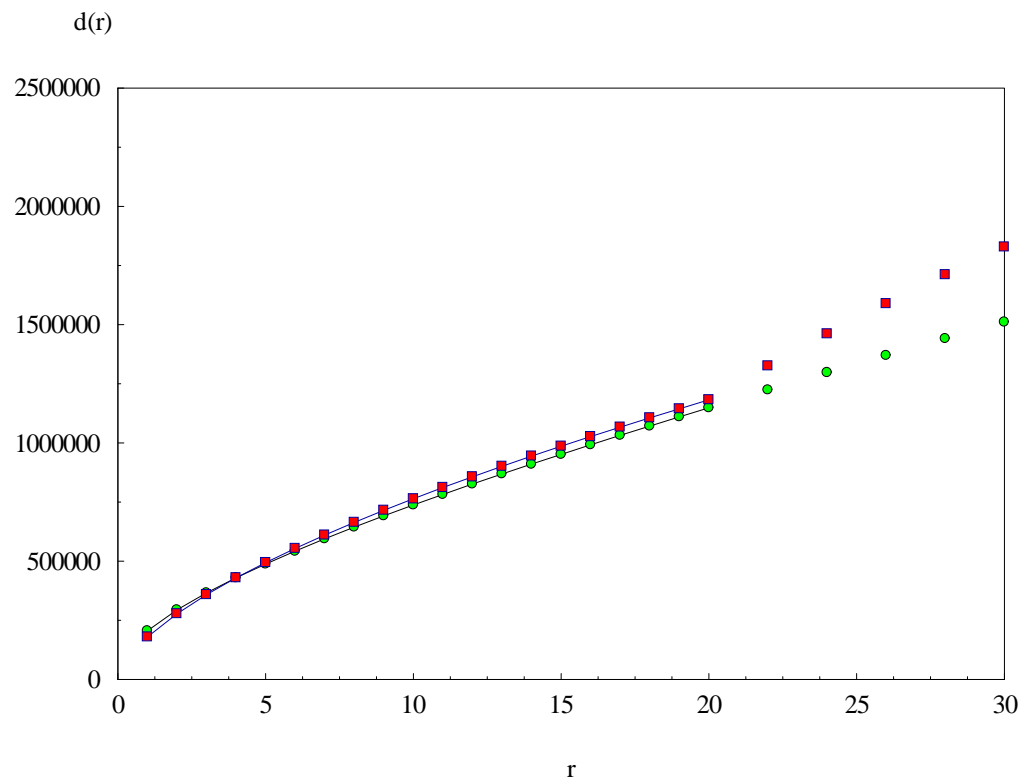


Figure 2.12. Power law fit for $d(r)$ the exponential surface correlation function over a large range of r .

CHAPTER 3

Neutron Beams between Absorbing Rough Walls: Square Well Approximation

3.1. Description of Problem

In this Chapter we deal with a slightly different UCN diffusion problem which is more directly related to the GRANIT experiments in the ILL, Grenoble. In experiments the UCNs travel between rough absorbing walls and the number of UCNs exiting the cell is measured as a function of the distance between the walls. We start from discussing the case without gravity because it is simple and will serve as a good reference point. By comparing numerical results obtained with and without gravity we will understand what part of the experimental results should be directly attributed to the Earth's gravitational field.

The neutrons in the cell are passing between the two mirrors, the perfectly smooth bottom mirror ("floor"), and the randomly rough upper mirror ("ceiling").

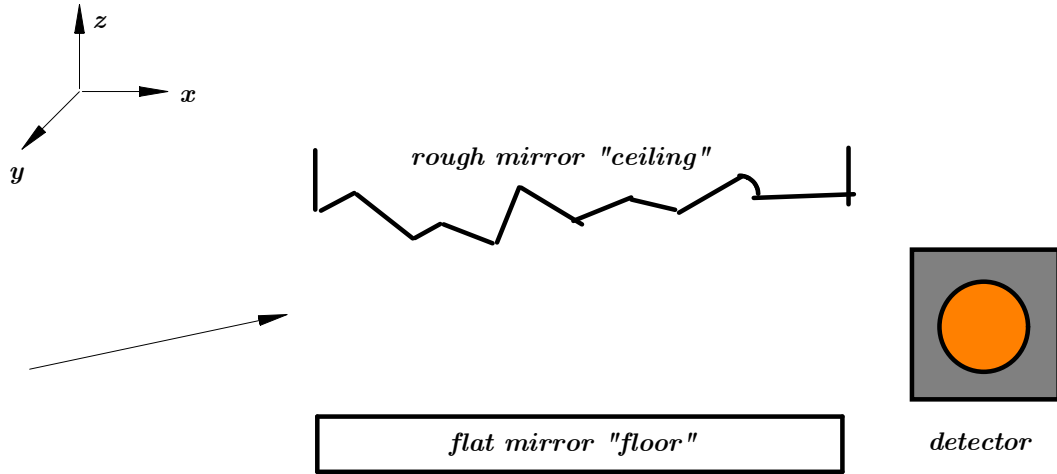


Figure 3.1. Sketch of neutron beam entering the experimental cell: the neutrons pass between rough "ceiling" and smooth "floor".

The UCNs entering the cell have a large horizontal velocity ($\sim 5 - 15$ m/s) and very small vertical velocities. When the neutrons scatter off the rough ceiling, the velocity vector with large horizontal component turns thus increasing the vertical component of the velocity. If the vertical velocity exceeds a certain velocity threshold (the critical velocity is ~ 4 m/s), the neutrons penetrate the wall, are absorbed, and do not reach the detector. The neutrons which manage to make it through the cell without reaching the critical vertical velocity are not absorbed and reach the neutron detector at the end of the cell.

The parameter that can be easily manipulated in experiment (and, of course, in calculations) is the cell width H . In computations we look at about 1000 values of dimensionless $h = H/l_0$ between 0 and 9. This problem differs from the setup mentioned in the section above where we are studying the diffusion coefficient $d(r)$

and the MFP not only in the fact that we are now measuring the exit neutron count, but also in the fact that we are now dealing with absorbing walls and time-dependent numbers of neutrons. Again, the main difference with regard to the previous chapter on diffusion is that previously we were letting the neutrons just bounce around without disappearing (they decay naturally at around 900 s). Now the neutrons disappear forever as the component of the velocity normal to the wall reaches a threshold value $\sqrt{2mU_c}$ and the number of neutrons becomes time-dependent as well.

The quantization of restricted motion is a well-known quantum phenomenon. In the absence of gravity we are dealing with the simplest square well potential with the energy levels

$$(3.1) \quad E_j = \frac{1}{2m} \left(\frac{\pi \hbar j}{H} \right)^2 .$$

If one adds weak gravity, the square well gets distorted by the appearance of a linear potential near the bottom, mgz (see Fig.[4.1]). With the presence of a linear potential the problem still remains solvable, though there is no simple analytical expression for the energy levels.

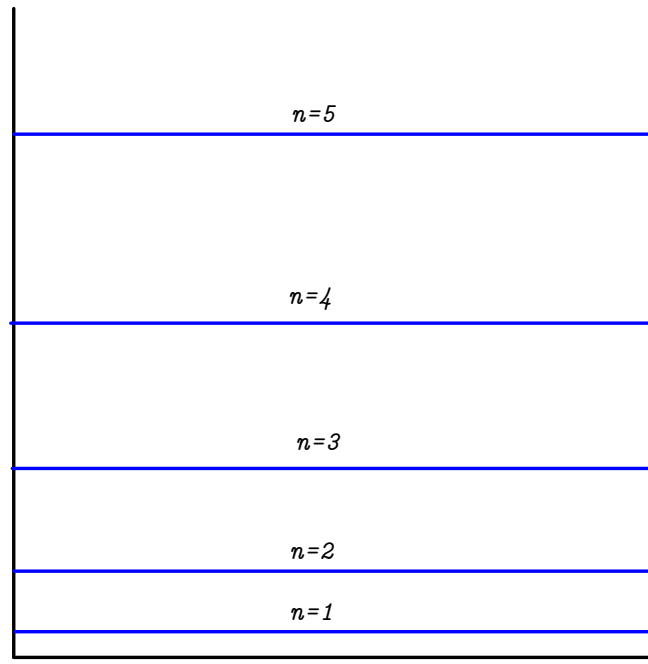


Figure 3.2. Square well levels.

To recap from the experiment briefly, we are dealing with a collimated beam being sent between two horizontal solid plates (one which is an almost ideal mirror and the other is rough) that are at a distance of several micrometers apart. We know that the neutrons hitting the wall with the normal velocity above 4 m/s get absorbed by the plates. Below this threshold velocity the neutrons get reflected. The reflection is specular locally.

First, we will neglect the presence of gravity. The effects of gravity will be introduced later, in the next chapter.

3.2. Wavefunction for the Square Well

We start by introducing the equation for the wavefunction on the wall in the square well,

$$(3.2) \quad \psi_j(H) = \sqrt{\frac{2}{H}} \sin\left(\frac{\pi j \hbar}{H q_j}\right)$$

where H is the width of the waveguide. Below we will use the same dimensionless variables as in the previous chapter.

To determine the roughness-driven transition probabilities, Eq.(3.7), we need the value of the square of the wavefunction at the upper wall. The equations that we are using can be written in terms of b_j Eq.(3.3) and since it is the quantity that has been used throughout the years in the papers by *Meyerovich et al*, Ref. [[1]-[8]] it is also the notation that we will be using from here on out in this thesis. Hence, we define the b_j in dimensionless units as follows,

$$(3.3) \quad b_j(H) = 10^5 \frac{l_0 \psi^2(H)}{2}.$$

In the case of the square well this reduces to

$$(3.4) \quad b_j = 10^5 \frac{\lambda_j}{h u_c},$$

where λ_j is defined as

$$(3.5) \quad \lambda_j = \left(\frac{\pi j}{h} \right)^2.$$

The values of b_j 's in the gravitational potential we will get from the Airy functions, which will be discussed more in the next section. The constant 10^5 is here merely as a scaling factor to avoid dealing with very small numbers.

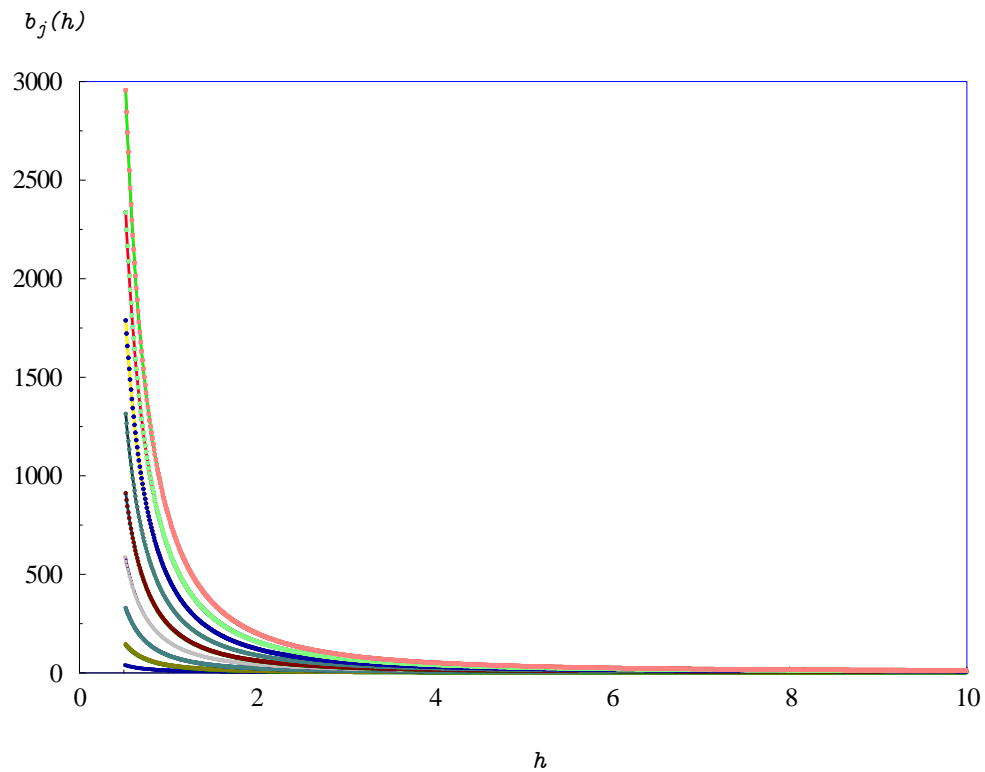


Figure 3.3. Coefficients $b_j(h)$ Ref[3.3] as a function of the width of the channel h for the square well.

In Fig.[3.3] we see the values of wavefunctions squared on the wall as a function of the width of the channel h .

3.3. Transition Probabilities and Neutron Count

As mentioned above, we are dealing with the same set of transport equations as in the previous Chapter of diffusion and mean-free path. Here again, we start

with the transport equation,

$$(3.6) \quad \frac{\partial N_j}{\partial t} = \frac{m}{2\pi} \int d\theta W_{jj'} (|\mathbf{q}_j - \mathbf{q}_{j'}|) (N_{j'} - N_j).$$

In this section we are looking only at the exponential correlation function of the surface inhomogeneities and are not interested in the potential Gaussian correlations. The reason for this is that recent analysis of the surface roughness of the new "rough" mirror have led us to believe that the surface roughness is exponential rather than Gaussian Ref.[9] We therefore use the transition probabilities with the exponential correlation function. Since we previously introduced the transition probabilities, we will write them directly in dimensionless variables,

$$(3.7) \quad w_{jj'}^{(0)} = \frac{32r^2\eta^2}{\sqrt{2\pi}h^2} \left(\frac{\pi j}{h}\right)^2 \left(\frac{\pi j'}{h}\right)^2 \frac{E(\Omega)}{\left(1 + r^2(q - q')^2 \sqrt{1 + r^2(q + q')^2}\right)}$$

$$(3.8) \quad w_{jj'}^{(1)} = \frac{32r^2\eta^2}{\sqrt{2\pi}h^2} \left(\frac{\pi j}{h}\right)^2 \left(\frac{\pi j'}{h}\right)^2 \frac{(1 + r^2(q + q')^2) E(\Omega) - (1 + r^2(q - q')^2) K(\Omega)}{\left(1 + r^2(q - q')^2 \sqrt{1 + r^2(q + q')^2}\right)},$$

where

$$(3.9) \quad \Omega = 2r \sqrt{\frac{qq'}{(1 + r^2(q + q')^2)}}.$$

and $E(\Omega)$ and $K(\Omega)$ are elliptical integrals.

As above we use the transition probabilities to get the dimensionless transition frequencies $\tau_{jj'}^{-1}$,

$$(3.10) \quad \frac{1}{\tau_{jj'}} = \sum_{j''} \left[\delta_{jj'} w_{jj''}^{(0)} - \delta_{j'j''} w_{jj''}^{(1)} \right]$$

we can now write the neutron exit count in terms of these relaxation times in a simple form

$$(3.11) \quad \frac{N_e(L)}{N_0} = \sum_{jj'} \exp\left(-\frac{t_L}{\tau_j}\right),$$

where t_L is the time of flight of the UCN between the mirrors and τ_j are the eigenvalues of Eq. (3.10).

3.4. Numerical Results

Initially, we want to start off by defining and discussing the parameter that we introduce, $S1$. The $S1$ parameter is a cutoff parameter. If we were to numerically solve the above equations for the whole system, we would be solving more than 10^3 coupled linear equations with complicated coefficients. Solving a system of that many equations is computationally very expensive time-wise even with modern computers, as each value takes approximately 30 min, and we do 900 iterations over values of h from 9 to 1 for each r . Therefore, we wanted to examine if there were a reasonable cutoff, which would keep enough equations to not lose much accuracy in the calculations, while also being much less expensive time-wise

computationally. To identify the $S1$ cutoff, we simply run the computations using more and more equations until we see that there is a saturation in the results. The saturation point becomes our cutoff point. We define that parameter as $S1$. In this section we are presenting some of our numerical results.

As we see in the figures below, Fig.[3.4]-Fig.[3.9], we are plotting the number of neutrons exiting the waveguide as a function of the size of the matrix $S1$. As one can see from all these figures presenting the exit neutron count as a function of $S1$ for various values of r and h , in all the cases $S1 \sim 300$ can serve as a good cutoff parameter. From this point onward, we choose in all computations $S1 \sim 300$ and just occasionally check the results for larger matrices.

As a next step, we compute the dependence of the exit neutron count N_e on r and h . The following figures show $N_e(h)$ for $r = 1; 5; 10; 30$. The data in the figures show that, in principle, the neutron count is very sensitive to both r and h . The common feature is that the exit neutron count is always extremely small except for very small values of h and large values of r . For practical purposes this means that taking into account the small number of ultra-cold neutrons entering the waveguide, we should not expect any neutrons exiting at all. The obvious conclusion is that the existence of neutrons exiting the cell in the Grenoble experiments is due only to the Earth gravitational field (see the next section). Though this gravitational field is extremely weak, without it the neutron count would have shown zero neutrons exiting the cell with rough walls.

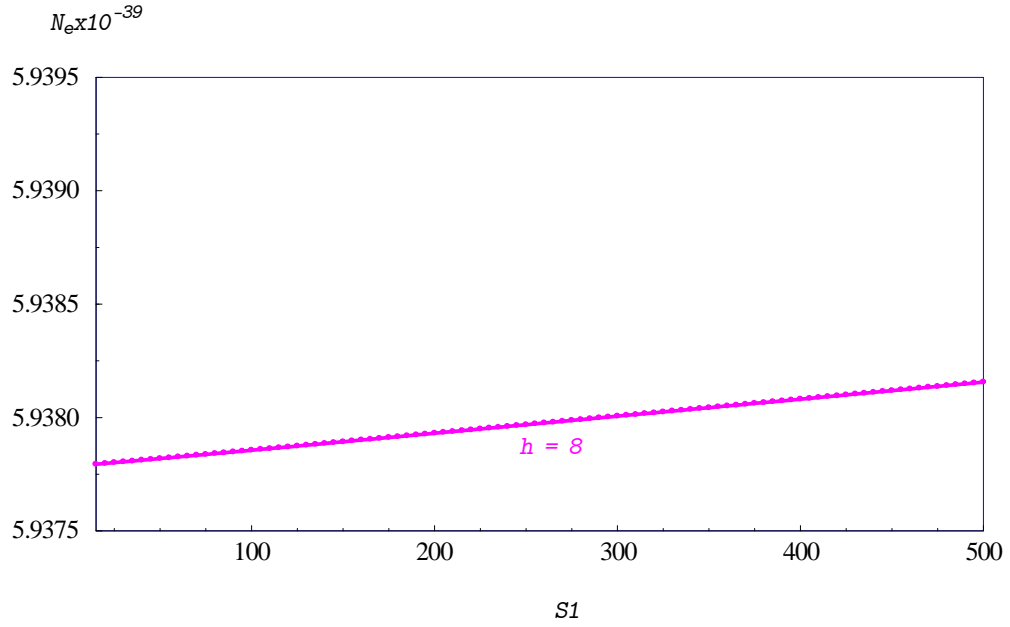


Figure 3.4. N_e as a function of the cutoff parameter $S1$ for $h = 8$ and $r = 0.65$. Here we can see the initial increase.

As we can see from the plot, Fig.[3.10], representing the total neutron count as a function of h for very small $r = 0.1$, already at large h the number of surviving neutrons goes to zero almost immediately when we have such a small correlation radius.

For $r = 1$, Fig.[3.11], we see that the depletion of the total neutron count to zero is slightly less rapid, though it also goes to zero very quickly around $h = 9.4$. Though again, if one pays attention to the $N_e(h)$ axis, we see that the number starts from what is essentially zero to begin with.

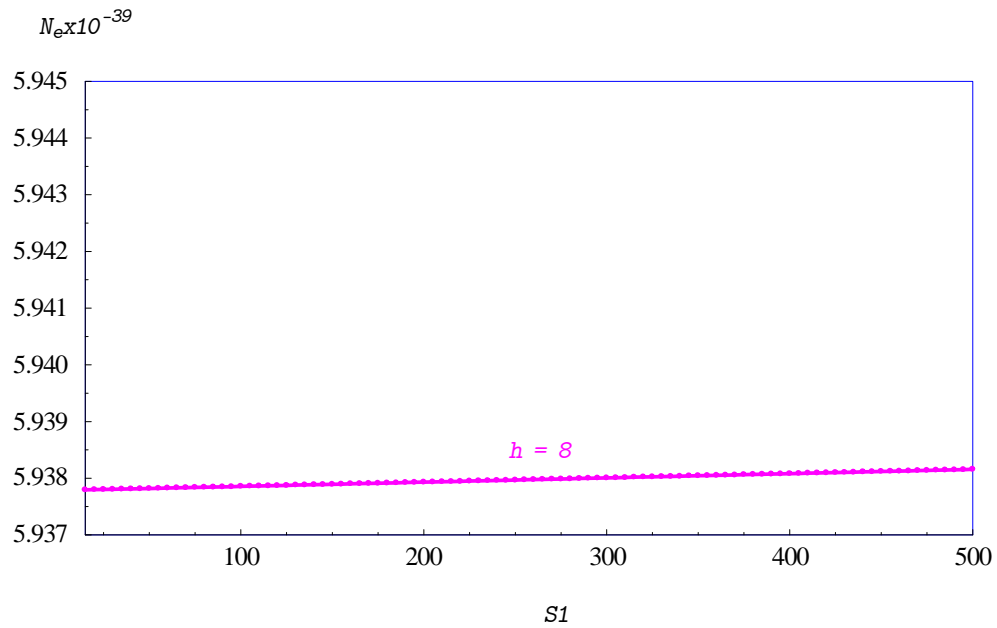


Figure 3.5. Neutron count as a function of the size of the matrix $S1$ for $h = 8$ and $r = 0.65$. We can see how it saturates nicely, at about $S1 = 300$. In this plot we are looking at N_e over a larger scale.

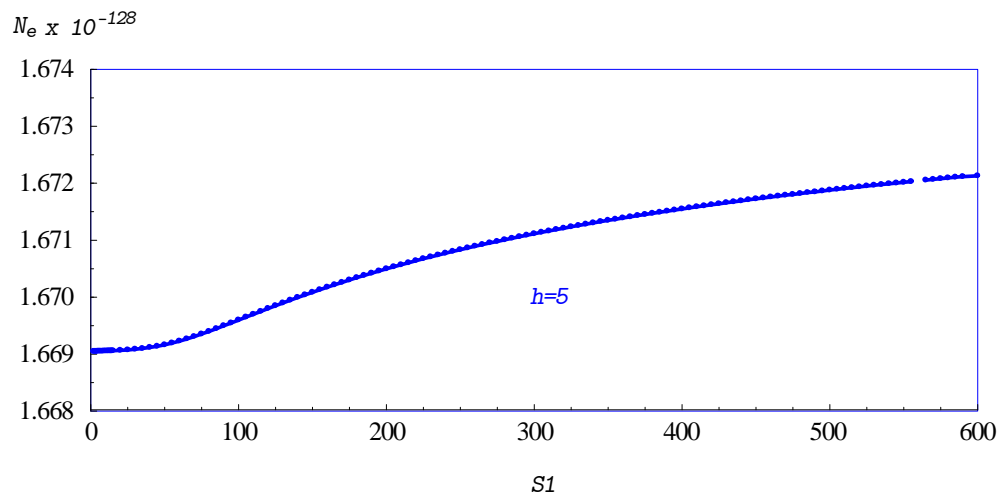


Figure 3.6. N_e as a function of the size of the matrix $S1$ for $h = 5$ and $r = 0.65$. We are looking at N_e closer scale, so that we can see the initial increase and gradual saturation.

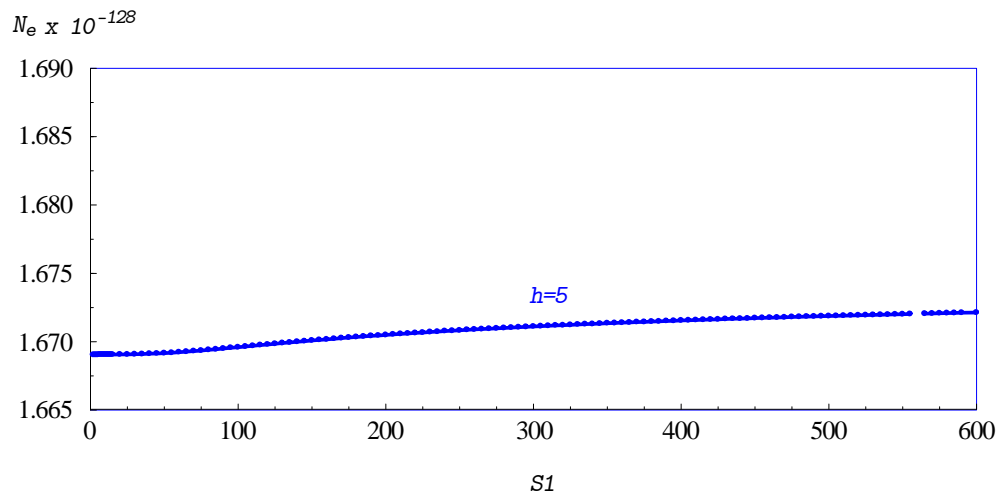


Figure 3.7. Saturation of the neutron count as a function of the size of the matrix $S1$, for $h = 5$ and $r = 0.65$.

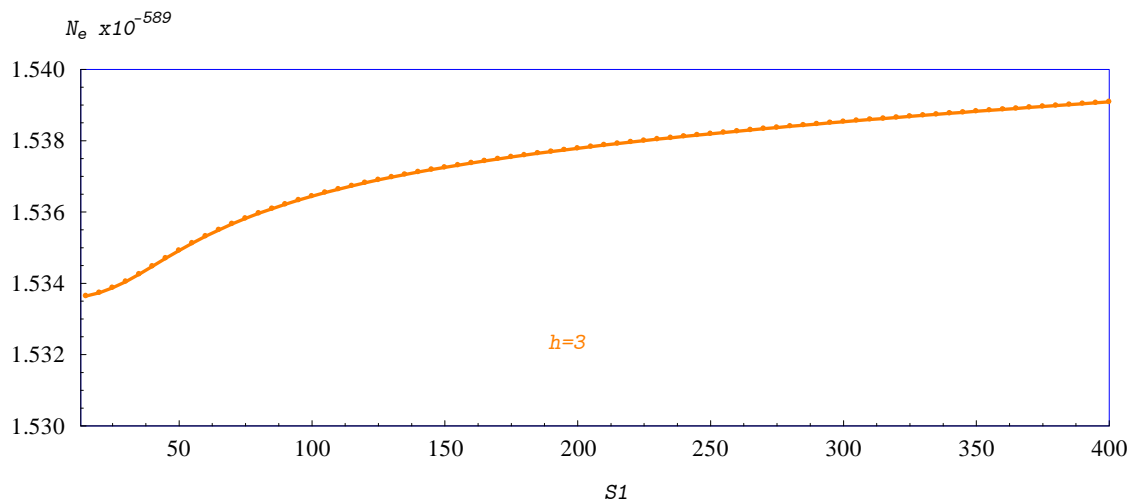


Figure 3.8. N_e as a function of the matrix size $S1$ for $h = 3$ and $r = 0.65$. We are looking at N_e closer scale, so that we can see the initial increase and gradual saturation.

The results for the total neutron count for $r = 5$, Fig.[3.12] are consistent with the above results, though now the neutron count goes to zero for the width size of $h = 8.7$.

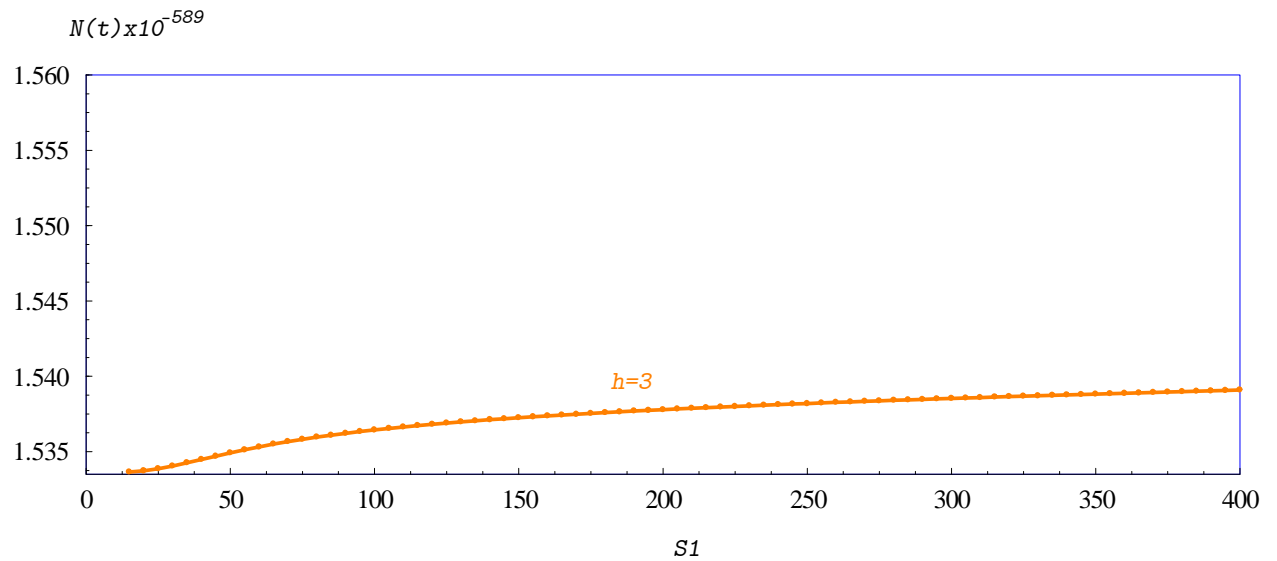


Figure 3.9. Neutron count as a function of the cutoff parameter $S1$ and $r = 0.65$ for $h = 3$.

In the last two plots, we are computing the total neutron count $N_e(h)$ over the full range of h for $r = 10$ (Fig.[3.13]) and $r = 30$ (Fig.[3.14]). As with all the results that we presented previously for varying r , we observe again that as we increase the radius of roughness the total neutron count goes to zero slower which here means at a smaller width size h .

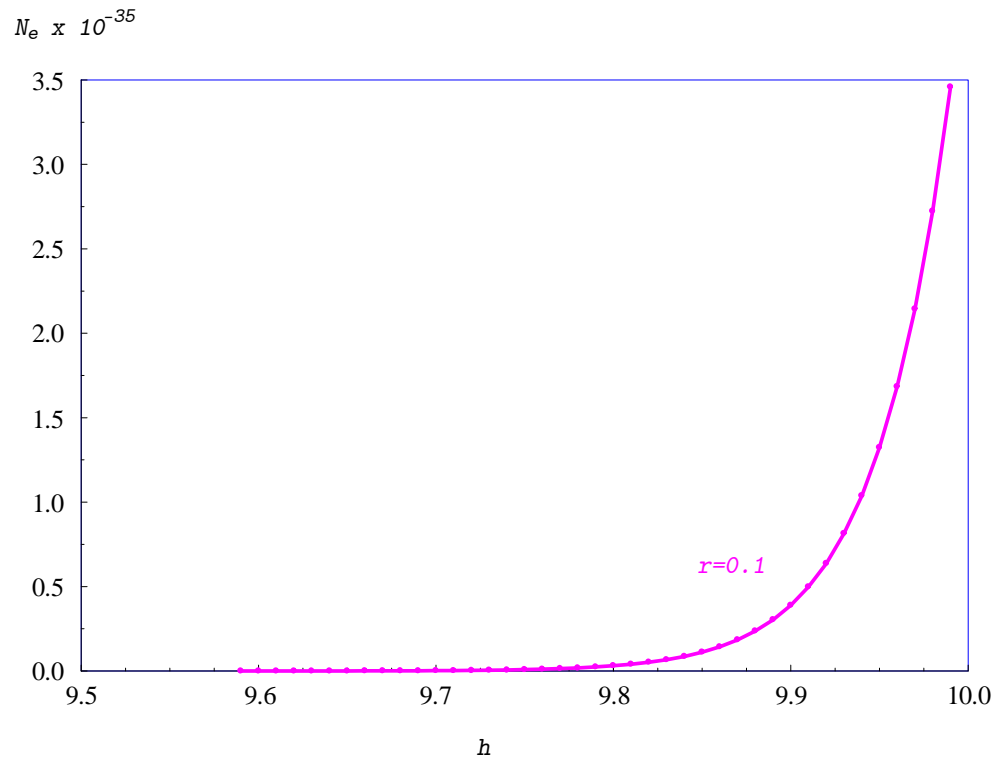


Figure 3.10. $N_e(h)$ as a function of h for $r = 0.1$.

We see in Fig.[3.15] the total neutron count as a function of the radius of roughness r . It's clear that only as the radius increases and becomes very large, the total neutron count becomes noticeable. The explanation is relatively simple. At very large r the walls become essentially flat and reflection is practically specular. Under these conditions the normal component of velocity remains small and neutrons do not penetrate the walls.

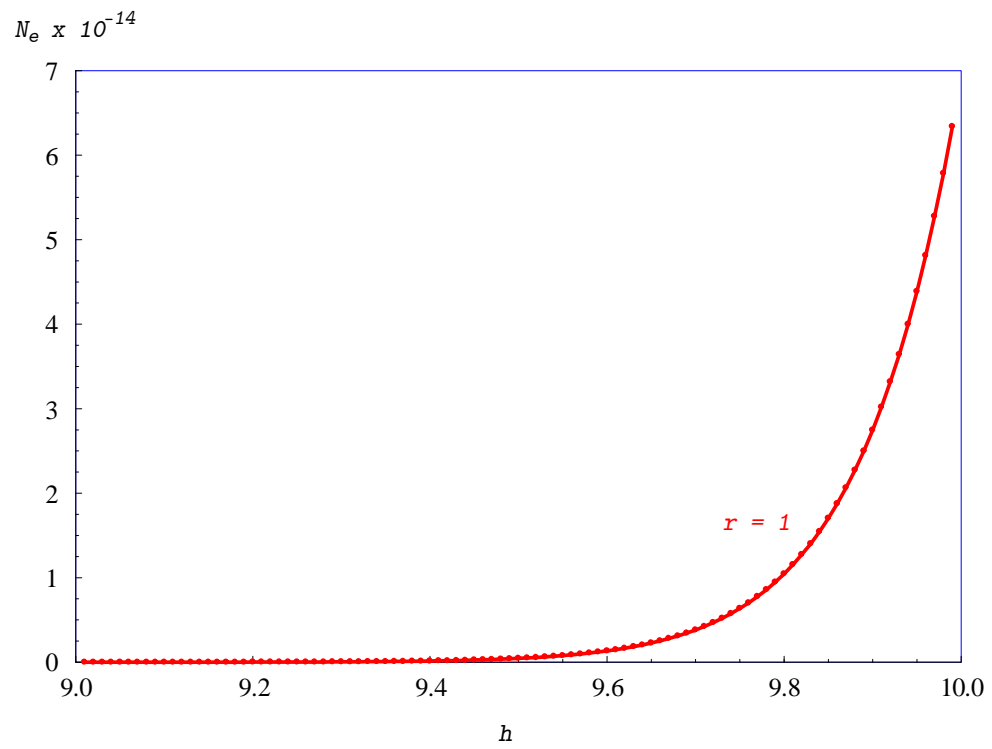


Figure 3.11. $N_e(h)$ as a function of h for $r = 1$.

Figure [3.16] similarly shows the total neutron count over various r , for $h = 5$.

Again only for large r does the neutron count become non-zero.

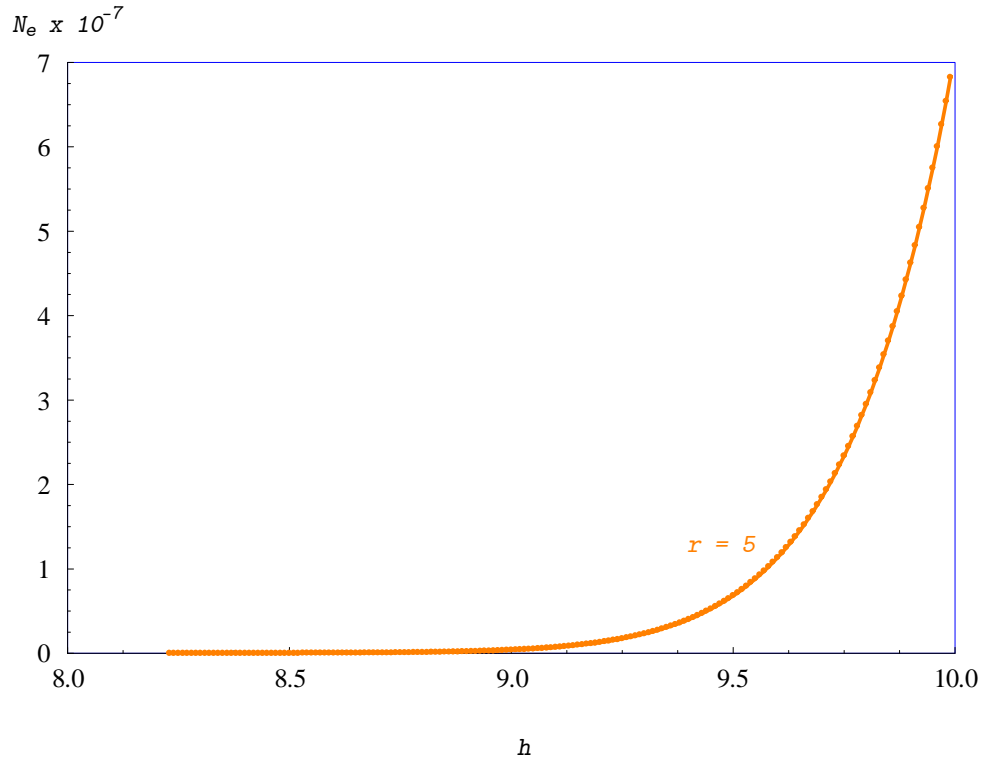


Figure 3.12. $N_e(h)$ as a function of h for $r = 5$.

The last two figures, Fig.[3.17]. and Fig.[3.18]., show that, as in the previous ones, the neutron count becomes non-negligible only for large r for $h = 7$ and $h = 9$, respectively. This is consistent with the theory that, for large enough r or in the limit that $r \rightarrow \infty$ we will not have any roughness and therefore all the neutrons will make it to the detector.

3.5. Conclusions

The main conclusions for this section are as follows.

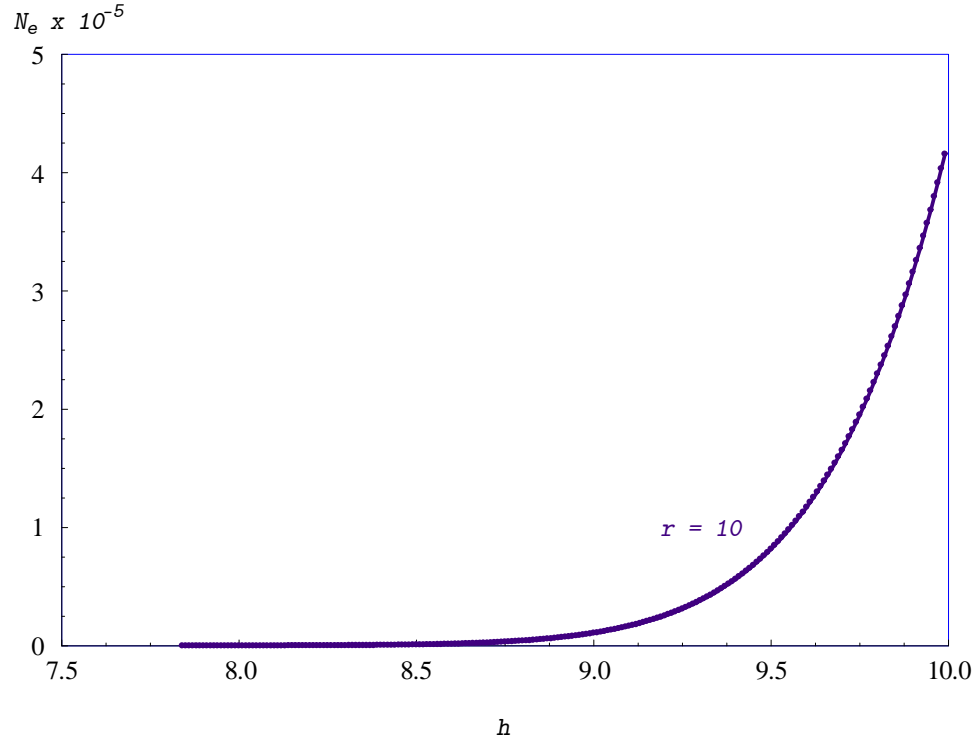


Figure 3.13. $N_e(h)$ as a function of h for $r = 10$.

- Irrespective of the well width and the correlation radius, a good cutoff parameter for all computations is around $S1 = 300$.
- As we increase the radius of roughness r , the total neutron count goes to zero for at a slower rate, meaning for smaller and smaller values of h .
- However, as we can see from the plots, the numbers that we get for $N_e(h)$ are always extremely small, so essentially all the neutrons die almost immediately.
- As we will see in the following section, this is not the case for the gravitational well. Hence, we can say that the square well approximation is very

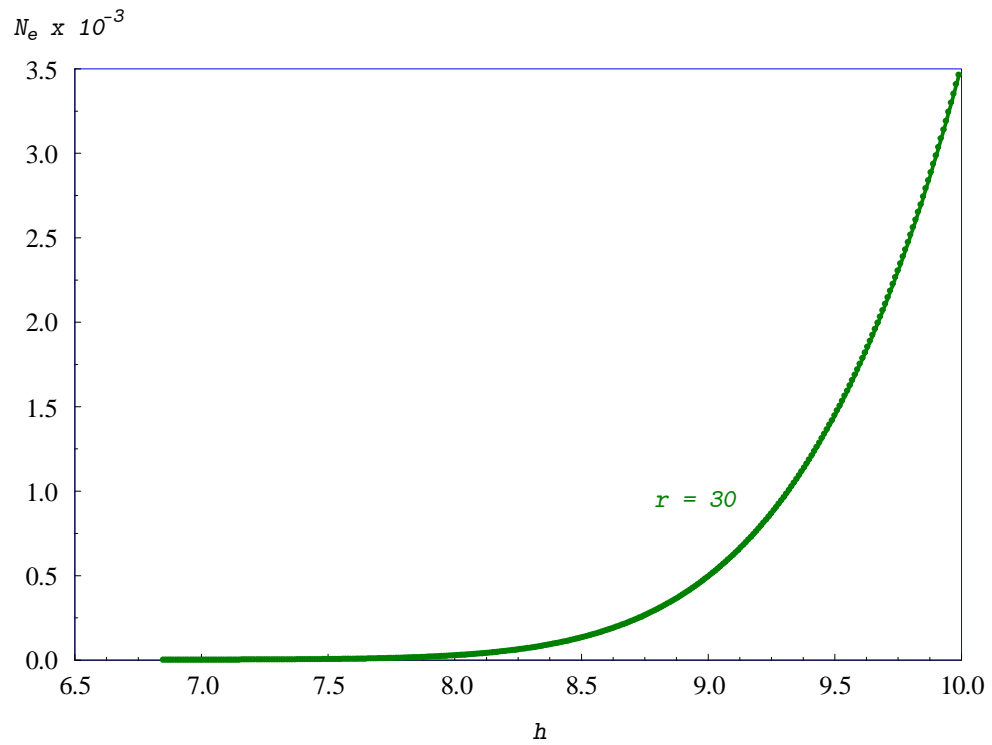


Figure 3.14. $N_e(h)$ as a function of h for $r = 30$.

poor for this particular problem: though the weak Earth gravitational field introduces only a small distortion near the bottom of the potential well, its effect on the neutron survival rate is very profound.

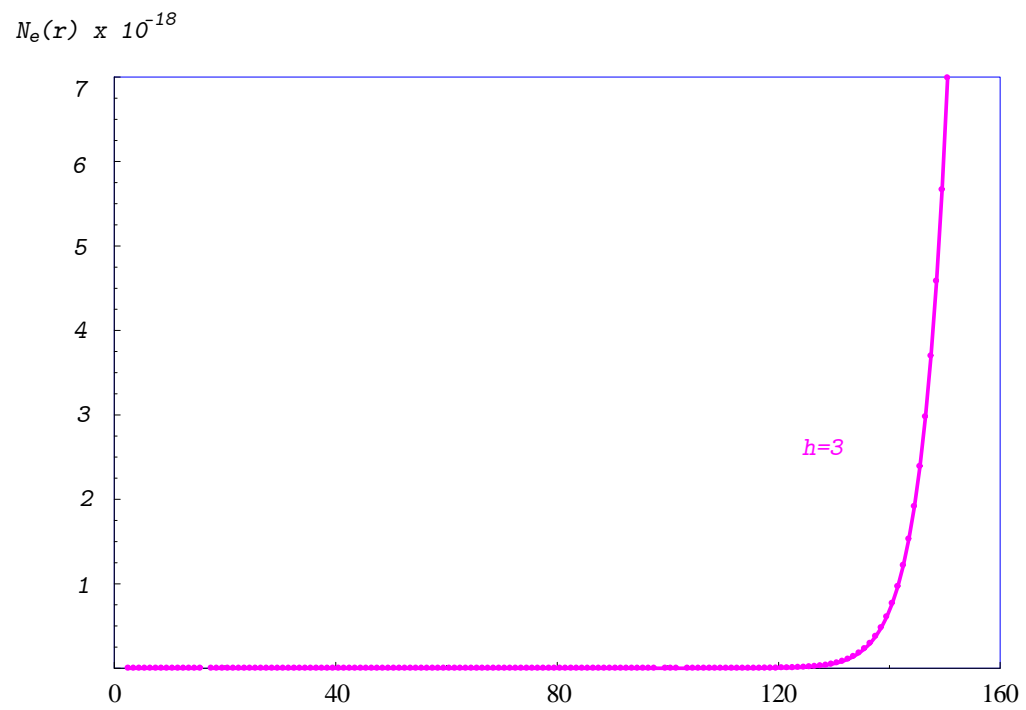


Figure 3.15. Total neutron count N_e as a function of different correlation radii r for small well width $h = 3$.

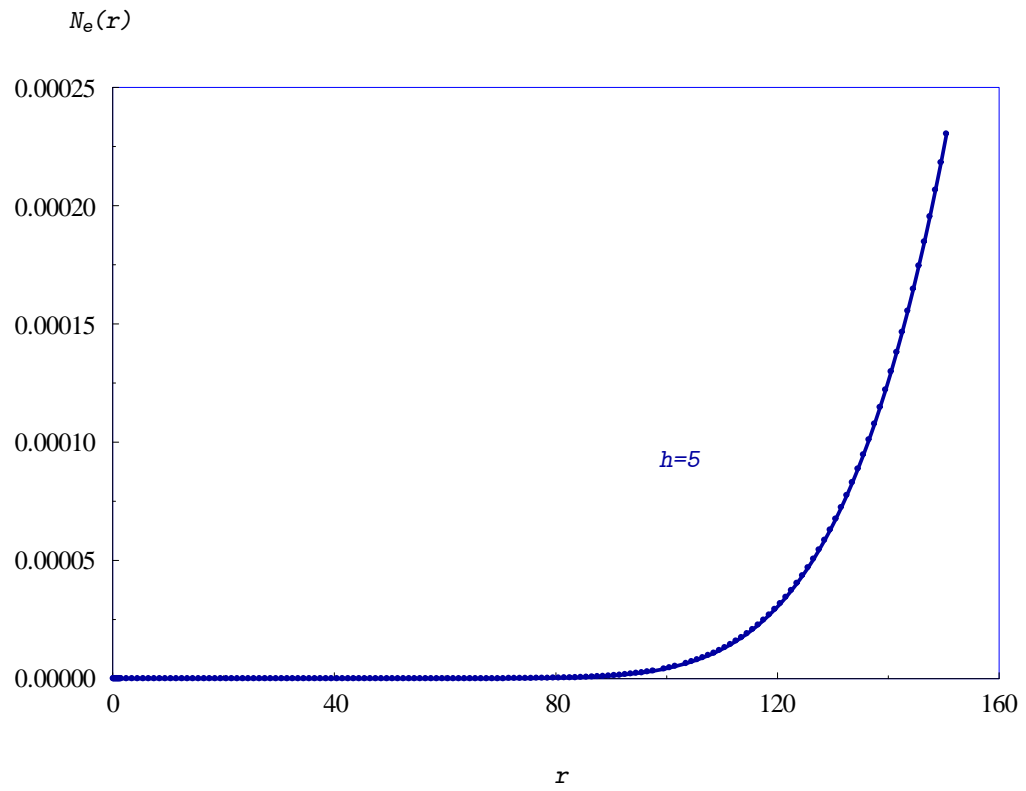


Figure 3.16. Total neutron count N_e as a function of different correlation radii r for well width $h = 5$.

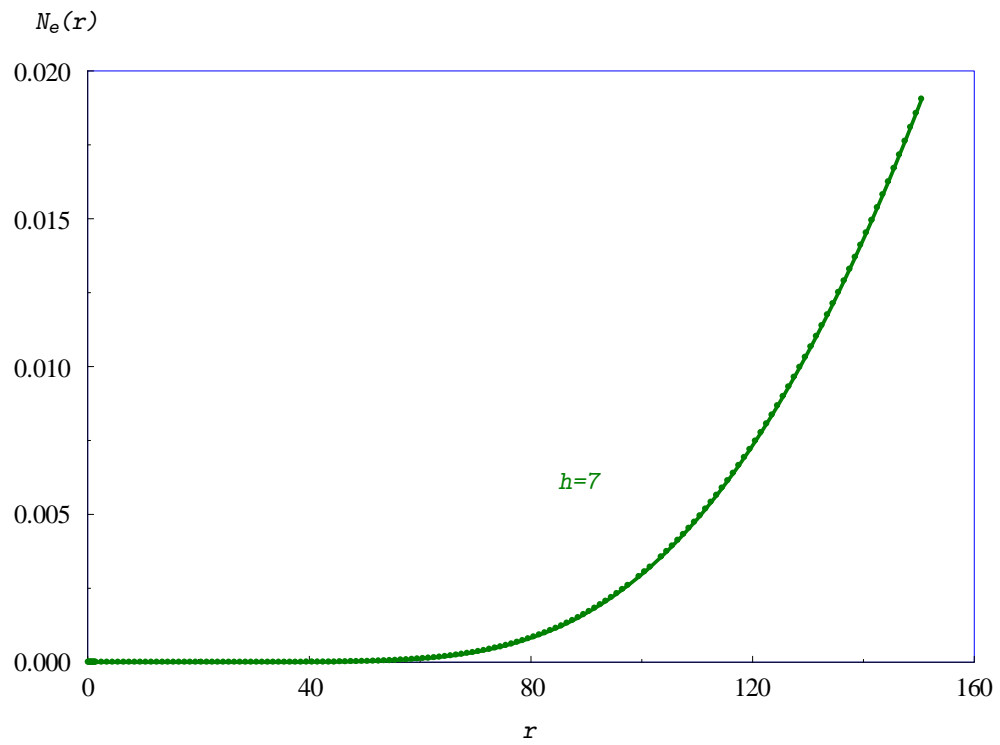


Figure 3.17. Total neutron count N_e as a function of different correlation radii r for well width $h = 7$.

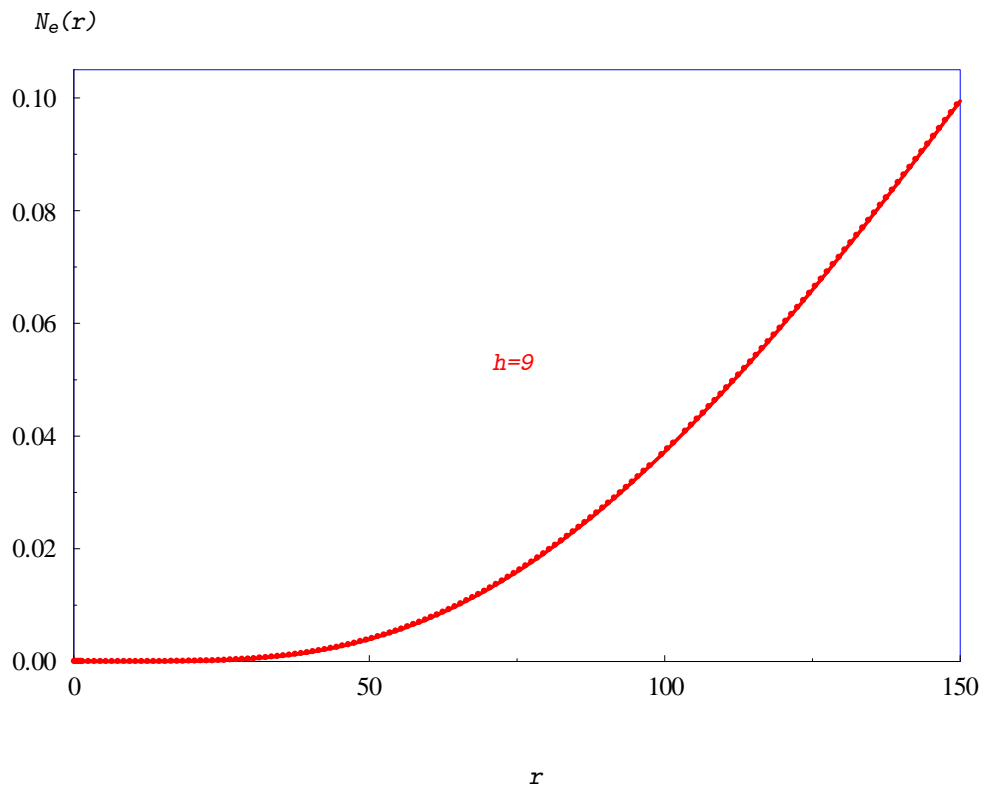


Figure 3.18. Total neutron count N_e as a function of different correlation radii r for well width $h = 9$.

CHAPTER 4

Neutrons in the Rough Waveguide in the Presence of Gravity

4.1. Gravity-Imposed Changes: Similarities and Differences with the Previous Chapter

In this Chapter we are looking at the same setup as in the previous Chapter but in the presence of the Earth's gravitational field. The purpose is twofold: to give an accurate description of the experiments of the Grenoble group and to understand what part of the observed anomalies can be attributed to the gravitational field. In the case of the gravitational well, we are dealing with a slightly different geometry than the square well. Of course, this change is due to the effect of the gravitational field. A sketch of this potential well is provided below (Fig.[4.1]). For the sake of comparison, the next figure (Fig.[4.2]) shows the dependence of the lowest energy levels on h for both the square well and the gravitational well.

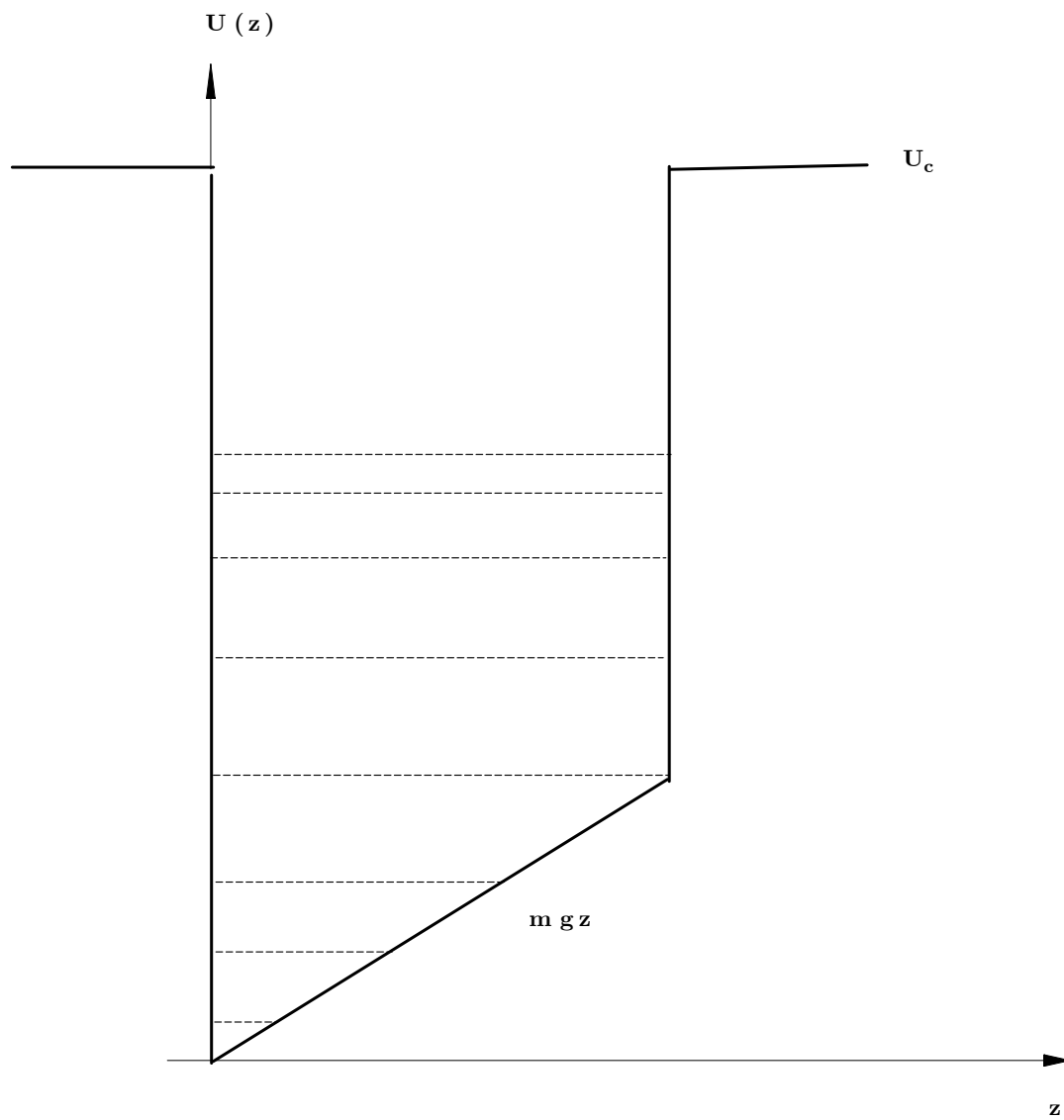


Figure 4.1. Sketch of the gravitational well as a function of z .

As we can see in the Figure below, we are looking at the first three eigenvalues for both the square well and gravitational potentials as a function of the width h . It is clear from this figure that for small h there is hardly any difference between

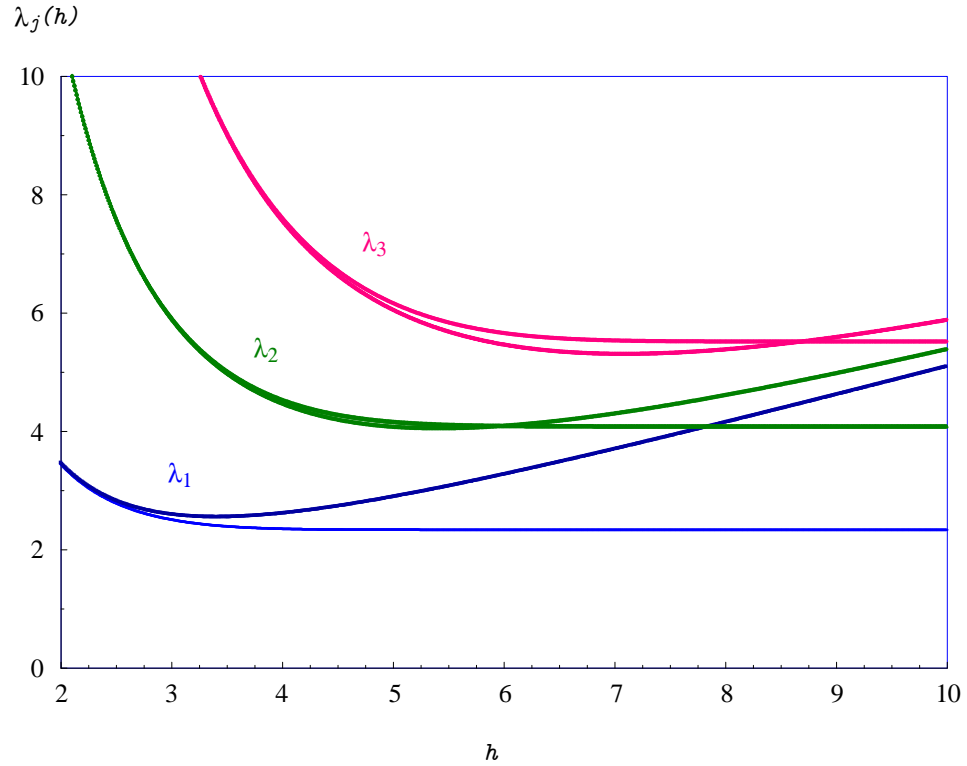


Figure 4.2. The first three eigenvalues for both the square well and the gravitational well as a function of the well width h . For better comparison, the bottom of the square well is chosen in the middle of the bottom of the gravitational well, $mgh/2$, and is drifting with h . The eigenvalues for the gravitational well are the lower curves, for the SW-the upper.

the lowest eigenvalues of these two potentials; for larger h the differences become significant.

Formally the transport equations for the rough waveguides with and without gravity are the same as Eq.(1.14). However, the transition probabilities are different. This difference, though significant, is related mostly to the values of the wavefunctions on the walls, i.e., to the coefficients $b_j(h)$, Eq.(4.2).

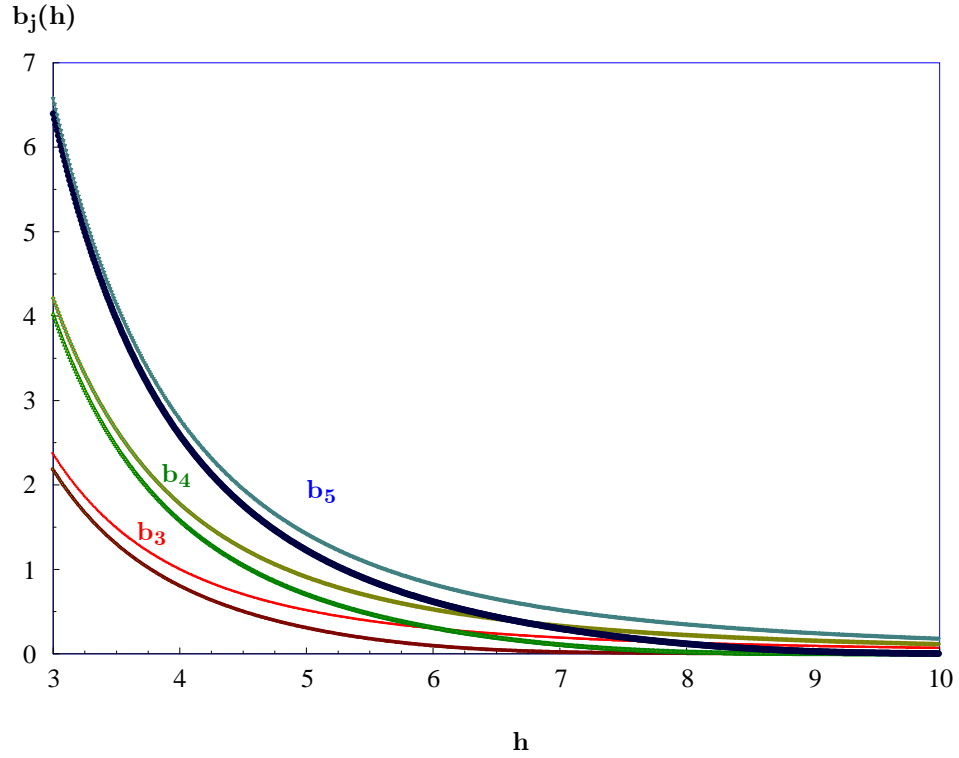


Figure 4.3. A few coefficients b_j 's as a function of well width size h for both the square (lower curves) and the gravitational wells (upper curves).

4.2. Results from the Preceding Work: the Biased Diffusion Approximation

The preceding work used what the authors called the biased diffusion approximation. Since the transitions $j \rightarrow j'$ show a strong upward bias due to the factor $b_j b_{j'}$ in the transition probabilities $W_{jj'}$ (essentially the factor $j^2 j'^2$ in Eq.(1.23)), the probabilities for the neutrons to return back to the lower states j after they jump to a higher state j' appear to be small and can be neglected. Then the

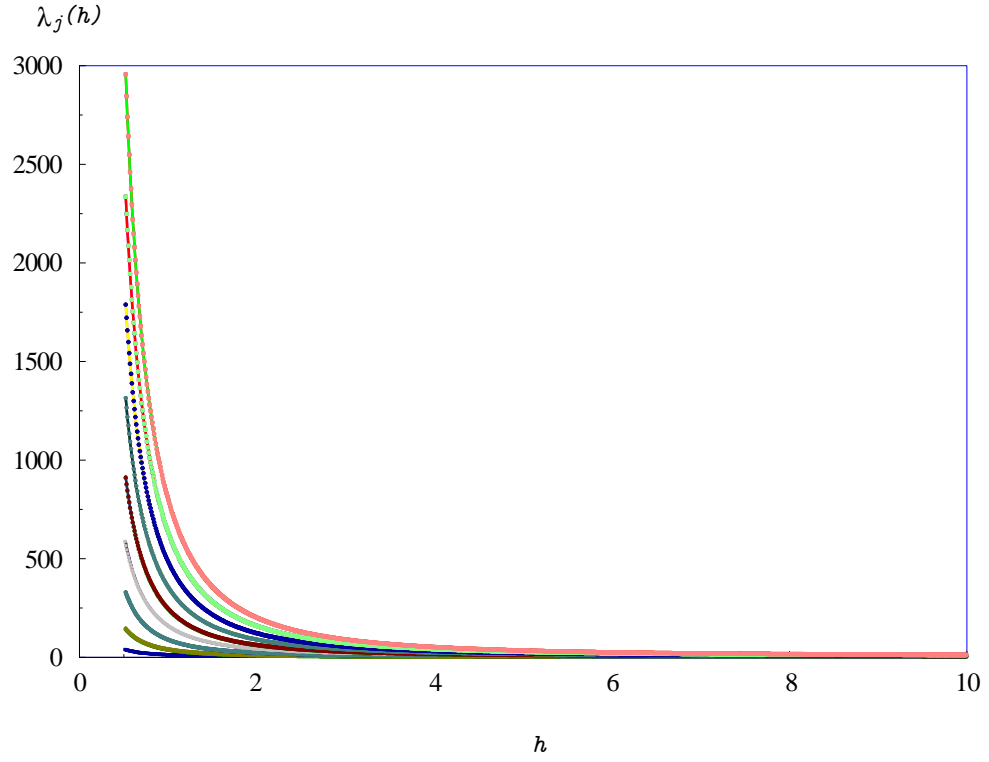


Figure 4.4. The first nine coefficients b_j as a function of the width of the channel h for the gravitational well. The lowest curve is b_1 and the highest b_9 .

absorption times τ_j are

$$(4.1) \quad \frac{1}{\tau_j} = m \sum_{j>j'} \int \frac{d\theta}{2\pi} W_{jj'}(|\mathbf{q}_j - \mathbf{q}_{j'}|),$$

where θ is the angle between \mathbf{q}_j and $\mathbf{q}_{j'}$. Note, that since the absorption threshold u_c is very high ($\sim 10^5$), direct transitions from the lower levels over the threshold are negligible.

What is more, the absorption times for neutrons that initially occupy some of the lowest minibands j differ from each other mostly by the values of the coefficients b_j ,

$$(4.2) \quad b_j = \frac{10^5 l_0 \psi_j^2 (H)}{2}$$

and therefore the above equation Eq.(4.1) becomes,

$$(4.3) \quad \frac{1}{\tau_j} = \frac{b_j}{b_1} \frac{1}{\tau_1}$$

where τ_1 is the depletion time for the neutrons in the first (or lowest) gravitational state. Note that this equation loses its accuracy for large values of j . Here we also note that the b_j are the dimensionless values of $\psi_j^2 (H)$.

The justification for biased diffusion is that the transition rates ($\tau_{jj'}^{-1}$) between the states (j and j') rapidly increase with both of these quantum numbers. Since the rates of the direct absorption processes also rapidly increase as j gets larger, this means that the neutron lifetimes in the higher states are orders of magnitude shorter than the lifetimes in the lower states. Therefore the diffusion of a neutron between energy levels has a strong upward bias. The increase in the jump rate from j to j' is moderated only by the correlation function, which is determined by the correlation radius r and starts rapidly decreasing at large $|j - j'| r$. This is why $w_{jj'}$ acquires a narrow peak centered at $j_1 \gg j$ Fig.[4.5] The bias is so strong that almost all the time τ_j spent for the neutron in a low gravitational state to

transition up to higher states and over the absorption barrier is spent in the first transition upwards.

The values of τ_j determine the depletion time of each quantum state. The overall exit neutron count is

$$(4.4) \quad N_e = \sum N_j = \sum N_j(0) \exp(-L/v_j \tau_j),$$

where $N_j(0)$ is the number of neutrons in a state j entering the waveguide of length L . Additionally, for the lowest levels the velocities v_j are almost the same, $v_j \approx \sqrt{\epsilon} v_0$. The equation above can be rewritten using $v_j \approx \sqrt{\epsilon} v_0$ and we can directly get all the τ_j . Then it is easy for us to get the total neutron count which is just a sum over all j . In the end, in the biased diffusion approximation all the pertinent parameters of roughness and the waveguide entering the exit neutron count collapse into a single variable Φ Ref[8] and we get an analytical solution,

$$(4.5) \quad \frac{N_e(h)}{N_0} = \sum_j \exp(-\Phi b_j(h))$$

where Φ is a complicated weighted integral of the correlation function that is dependent on the correlation radius. If the roughness is two-dimensional,

$$(4.6) \quad \Phi = A_2 \eta^2 r^2 \int_0^1 z^2 \psi_2(y_1, y(z)) dz$$

and

$$(4.7) \quad A_2 = \left(\frac{2}{\pi}\right)^{3/2} \times 10^{-5} \frac{t_L}{\tau_0} u_c \epsilon^{3/2},$$

where $\psi_2(y_1, y)$ is the dimensionless zeroth harmonic of the correlation function $\zeta(|\mathbf{q}_j - \mathbf{q}_{j'}|)$ over the angle between the vectors \mathbf{q}_j and $\mathbf{q}_{j'}$, and $y_1 = r\sqrt{\epsilon}$, $y(z) = y_1\sqrt{1-z^2}$.

We can write the relaxation time τ_1 for the lowest gravitational state as

$$(4.8) \quad \frac{1}{\tau_1} = m \sum \int \frac{d\theta}{2\pi} W_{1j'}(|\mathbf{q}_1 - \mathbf{q}_{j'}|),$$

where θ is the angle between the vectors \mathbf{q}_1 and $\mathbf{q}_{j'}$. Finally, after replacing the summation by the integration.

$$(4.9) \quad \frac{\tau_0}{\tau_1} = 2 \times 10^{-5} u_c^2 \left(\frac{\eta}{r}\right)^2 b_1(h) F_2(r, h).$$

where

$$(4.10) \quad F_2(r, h) \simeq r^4 \sqrt{\frac{2u_c}{\pi\chi^3}} \int_0^1 dz z^2 \psi_2(y_1, y).$$

When we combine the equations Eq.(4.9) and Eq.(4.10) we get the following equation,

$$(4.11) \quad \Phi(\eta, r) = A_2 \eta^2 r^2 \int_0^1 dz z^2 \psi_2(y_1, y)$$

This concludes the description of the preceding work, which provides the approximate analytical expression to the exit neutron count. We will now describe how we deal with the same problem computationally without relying on the biased diffusion approximation.

4.3. Exact Calculation of the Absorption Time

In our case we are not using the biased diffusion approximation, but actually using the brute force technique to solve the full set of transport equations numerically.

As a result, we do not get a nice analytical solution to the problem. Instead we use the full matrix, meaning the matrix with transitions upwards and downwards, for which we can only get a numerical solution. The structure of the diagonal and off-diagonal elements in the matrix transport equations is different. The diagonal elements have the structure defined below in Eq.(4.12), where for an element in row j we are summing over all the elements j' . The off-diagonal elements are simpler: these are simply $w_{jj'}$. We rewrite the transition probabilities $W_{jj'}$ defined in Eq.(1.22) that represent the diagonal elements of the matrix, in a notation that is closer to the one that was used in the most recent papers in this field. Therefore specifically for diagonal elements of our matrices, when $j = j'$, we write,

$$(4.12) \quad F_j(r, h) = \sqrt{\frac{2}{\pi}} \times 10^{-5} r^4 b_j \sum_{j' \neq j} b_{j'} \psi_2(y_1, y_{j'}),$$

where $\psi_2(y_1, y_{j'})$ here also represents the dimensionless zeroth harmonic of the correlation function over the angles between the vectors \mathbf{q}_j and $\mathbf{q}_{j'}$. Since we are not working under the context of biased diffusion, we can only perform our computations numerically.

We have off-diagonal elements in our matrix for square well are defined in dimensionless units as

$$(4.13) \quad w_{jj'} = \frac{32r^2\eta^2}{\sqrt{2\pi}h^2} \left(\frac{\pi j}{h}\right)^2 \left(\frac{\pi j'}{h}\right)^2 \frac{E(\Omega)}{\left(1 + r^2(q - q')^2 \sqrt{1 + r^2(q + q')^2}\right)},$$

where

$$(4.14) \quad \Omega = 2r \sqrt{\frac{qq'}{(1 + r^2(q + q')^2)}}.$$

Hence our total matrix, which we will call $M_{jj'}$ looks like

$$(4.15) \quad M_{jj'} = \begin{pmatrix} F_{11} & w_{12} & \dots & \dots & w_{1s \max} \\ w_{21} & \dots & \dots & \dots & w_{2s \max} \\ \dots & \dots & \dots & \dots & \dots \\ \dots & \dots & \dots & \dots & \dots \\ w_{2s \max} & \dots & \dots & \dots & F_{s \max, s \max} \end{pmatrix}.$$

More detailed mathematics regarding the $F_{jj'} = F_j(r, h)$ for the discrete case will be available in Appendix C.

We do not have a simple analytical description of the gravitational states similar to that for the square well states in the previous chapter. However, for the states with high index j , and especially at small h , the difference between the gravitational and square well states is negligible. Therefore, for higher states we can replace the gravitational states by the square well states.

As a result, our square matrix of transition probabilities acquires a block structure. One block representing the transitions between gravitational states, two of the blocks represent the transitions between the lower gravitational states and higher square well states, and the third block represents the transitions between higher square well states. Once we have the total matrix with all the block components, we are numerically computing the eigenvalues and eigenvectors of the total matrix. We can write the neutron exit count in terms of these absorption times τ_j in quite a simple form,

$$(4.16) \quad \frac{N_e(h)}{N_0} = \sum_j \exp\left(-\frac{t_L}{\tau_j(h)}\right),$$

where t_L is the time of flight of the UCNs between the mirrors. Note that the above equation was introduced in the previous section and chapter as it is a general equation that can be used with and without the biased diffusion approximation.

It is interesting to note that the center of the peak of the transition probabilities $W_{jj'}$ for transitions from j to j' is located at some $j_1 \gg j$, see Fig.[4.5] for example.

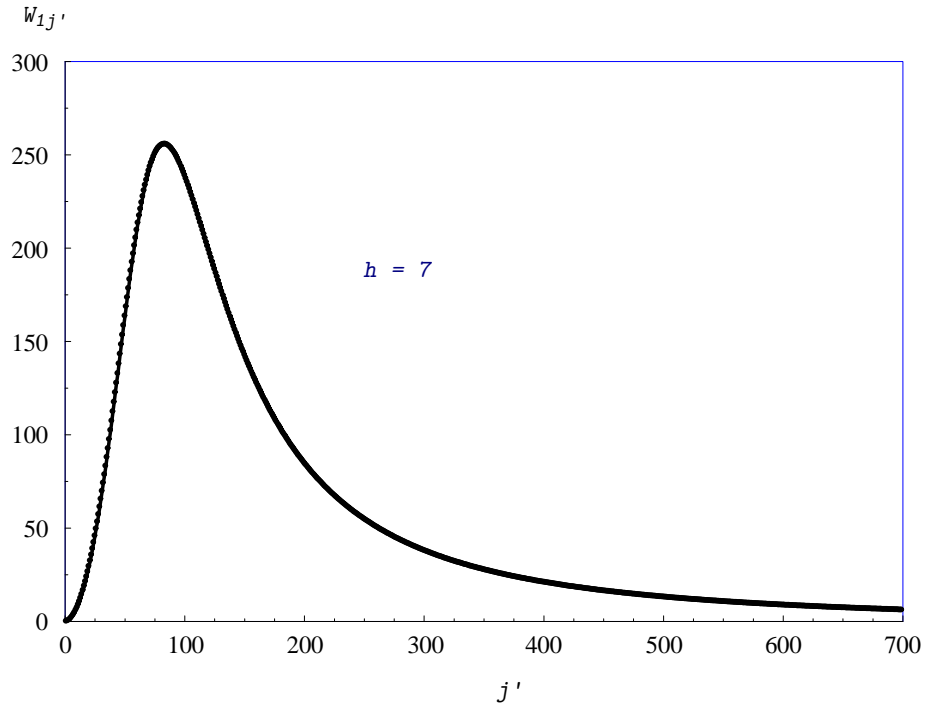


Figure 4.5. The transition probabilities $W_{1j'}$ as a function of j' exhibit the peak around $j' = 100$.

The peak is very high and relatively narrow.

4.4. Numerical Results

In this section we present the main results of the thesis as pertaining to the Grenoble experiments. As in the previous section regarding the square well potential, we are now looking at the exit neutron count in the gravitational potential. The gravitational potential was introduced in a previous chapter. However, we will reproduce a schematic figure here. In this figure, the particles on the lowest three levels "classically" do not reach the rough ceiling, do not scatter, and survive for a

long time. The particles from the higher levels are actively scattered on the rough ceiling, go rapidly upwards, and get absorbed by the walls. When the width of the waveguide h becomes smaller, all the levels are rapidly squeezed up (see Fig. below).

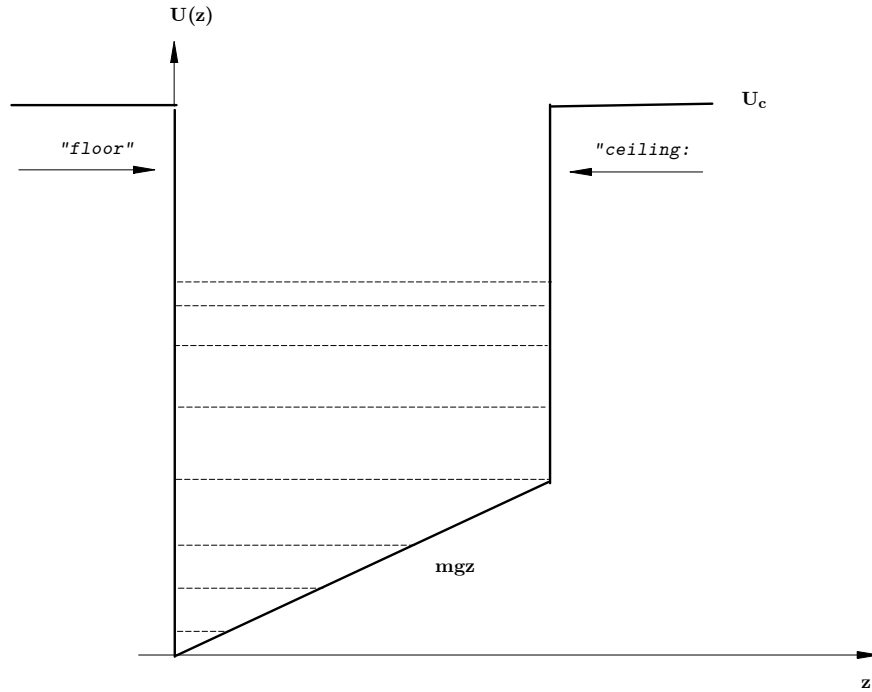


Figure 4.6. Potential with Earth's gravity field.

Though here we do not present a figure to show the saturation of the total neutron count as a function of the cutoff parameter $S1$, after doing many numerical simulations, it was determined from the results that the cutoff parameter was more or less the same as in the case of the square well potential, meaning that $S1 = 300$ is a good cutoff size to maintain high accuracy in the calculations, while simultaneously keeping the computation time sufficiently short.

The series of figures below present the neutron count N_e as a function of h for several values of the correlation radius r . In all figures the roughness correlation function is assumed to be exponential with the average amplitude $\eta = 1.02$. The

current rough mirror used by the Grenoble group probably has $r = 0.65$ and $\eta = 1.02$. As one can see, all the figures are similar, though the curves slowly shift to the left with increasing r . This is understandable: the surface becomes flatter with increasing r and the neutrons survive longer.

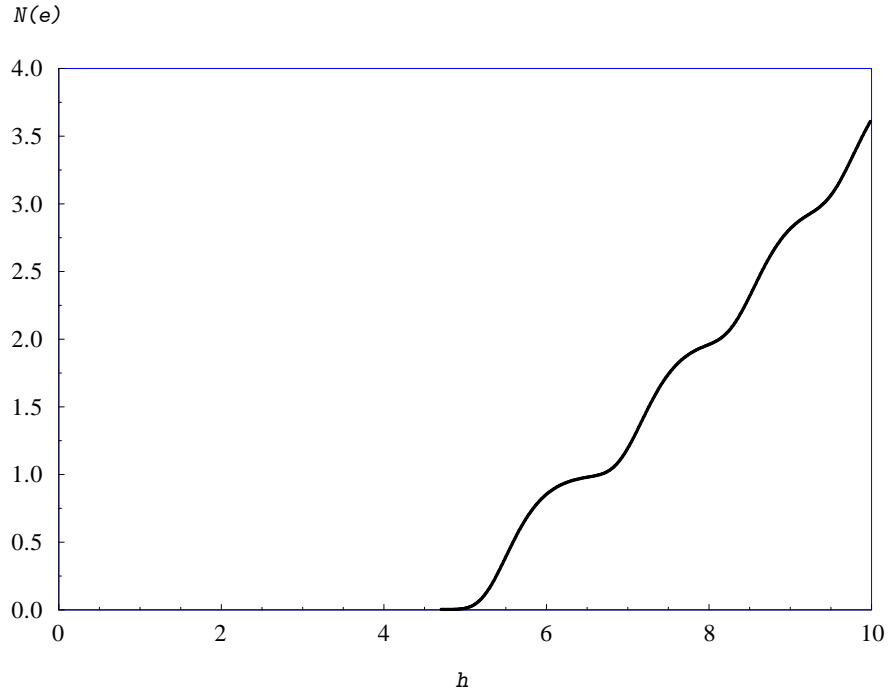


Figure 4.7. Neutron exit count as a function of h , for experimental parameters.

Figure [4.6] shows the neutron count $N_e(h)$ as a function of the width of the well h . The results are slightly different when you increase r , though we can see that for small h the difference is insignificant. Even for large h the difference is not huge, especially when you consider that the experimental $r = 0.65$ (Fig.[4.6]) is very small compared to $r = 5$ (Fig.[4.9]) or $r = 10$ (Fig.[4.10]). When we compare the figures of neutron count as a function of well width, we see one main feature; that is that as r increases, the curves becomes increasingly smoother. From these figures we see, much like with the square well potential, when you increased the radius of roughness r , the neutrons lived longer and they can be detected even for very

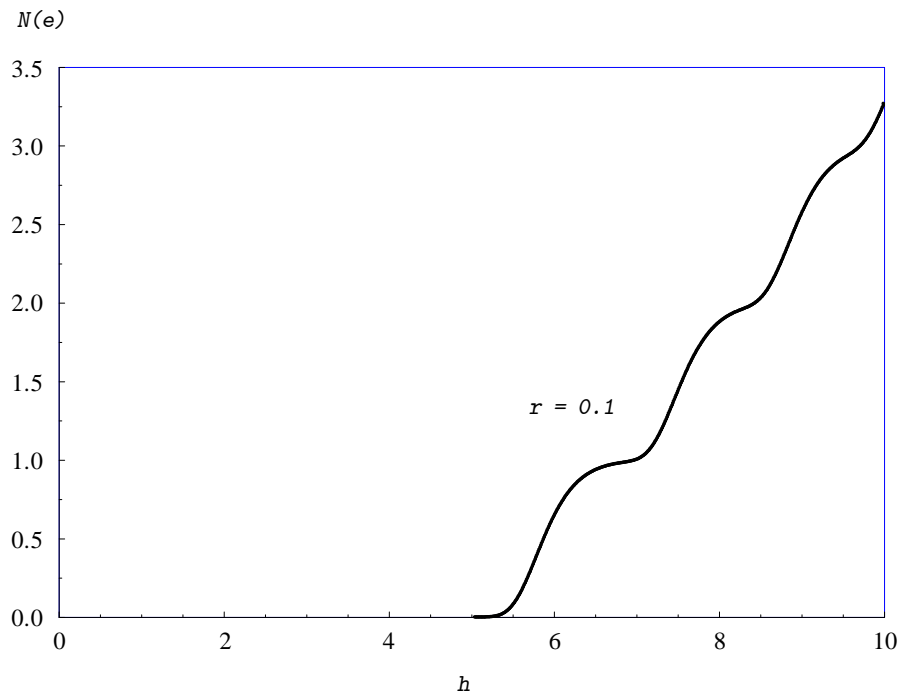


Figure 4.8. Neutron count as a function of h for correlation radius radius of roughness $r = 0.1$.

small width h . This is happening as well in the case of the gravitational potential. We see that as the radius of roughness gets larger and larger, the neutrons survive for smaller and smaller well width sizes.

For very large r , for example in the figures where $r = 500$ (Fig.[4.15]) and $r = 1000$ (Fig.[4.16]), we see that the curve flattens and we don't have the well defined steps that we see at smaller values of r , implying that the discrete energy levels cannot be detected so easily as with smaller r . However, it should be noted that this flattening happens only for unrealistically large r . In general the steps on the curves are very robust and the first bump remains detectable even for very

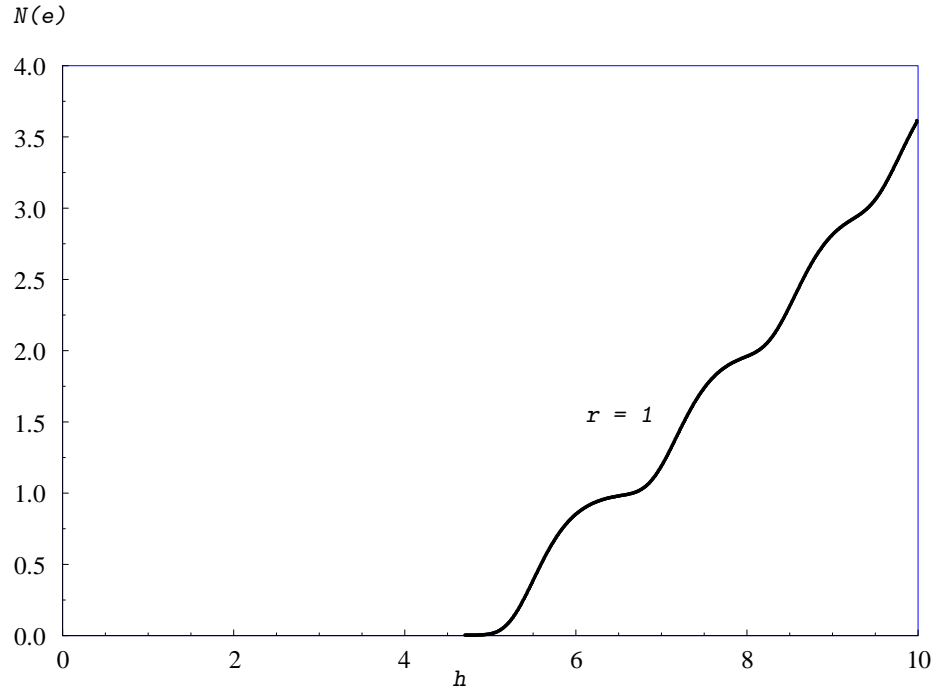


Figure 4.9. Neutron count as a function of h for correlation radius of roughness $r = 1$. This is approximately twice the experimental value of r .

large r . This of course is due to the fact that the neutrons are not scattering and dying but instead can easily make it to the end of the cell and to the detector since they are not influenced by roughness for large r . The ideal conditions for scattering are at $qr \sim 1$. From this condition we know that as r gets larger and larger and goes to infinity, we will have specular reflection.

The last figures, Fig.[18 – 20] show the neutron exit count for fixed widths $h = 9, 5, 3$ respectively. As we can see for all three widths, the neutron exit count increases as the correlation radius increases. This is because as we increase

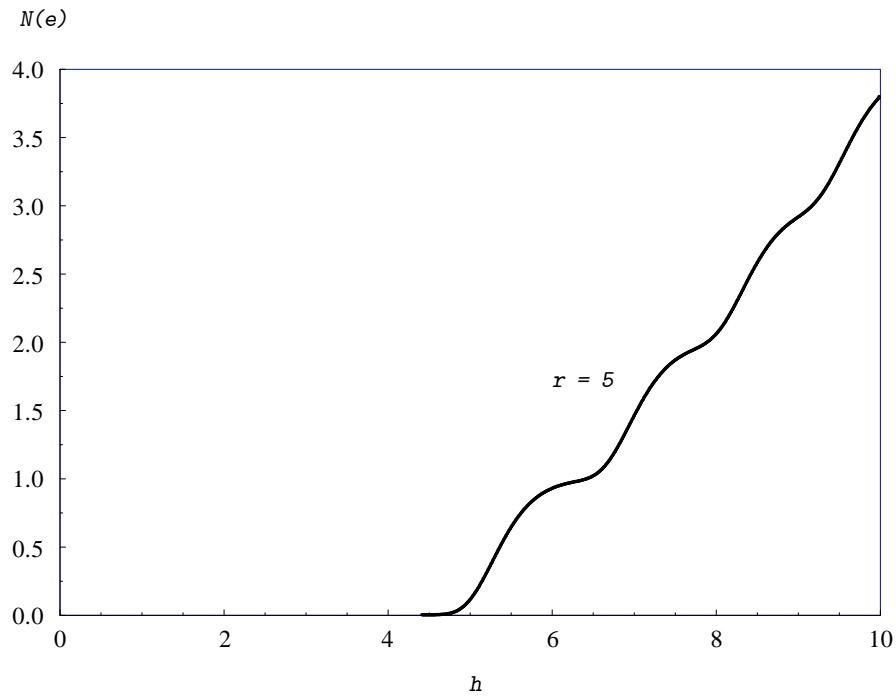


Figure 4.10. Neutron count as a function of h for correlation radius of roughness $r = 5$.

the correlation radius, the ceiling becomes smoother, and therefore there is less scattering and absorption by the rough wall.

4.5. Conclusions

It is interesting to compare these results with the previous results without gravity in the square well section.

- The dependence of the exit neutron count on r was much more significant in the case of the square well potential: $N_e(r)$ at fixed h changed by many orders of magnitude.

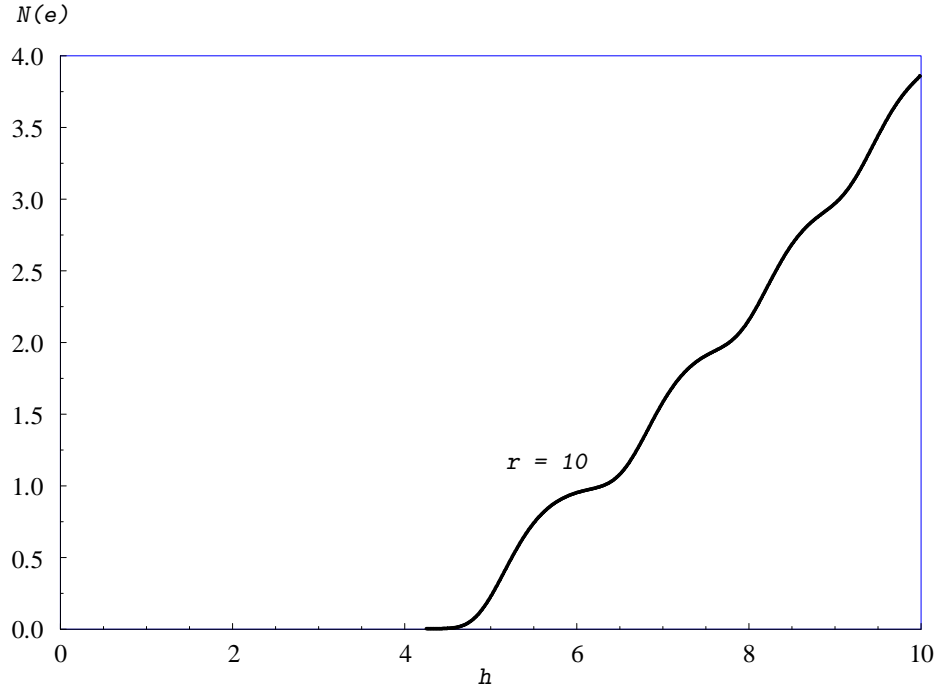


Figure 4.11. Neutron count as a function of h for correlation radius of roughness $r = 10$.

- It is interesting to note that the ratio of the relaxation times for the diagonal case (in which we do not take into account the transitions between the states, meaning the cases where $j \neq j'$) and the case described in this section (where we allow all the transitions, and not just the biased ones, to be taken into account) τ_{diag}/τ_{full} is close to 1. This was rather unexpected.
- It is also interesting to note that the ratio of the results for the matrix in the square well potential and the matrix in the gravity potential goes to one as h goes to 0, $\tau_{jSqwell}/\tau_{jgrav} \rightarrow 1$ as $h \rightarrow 0$ since all the levels are

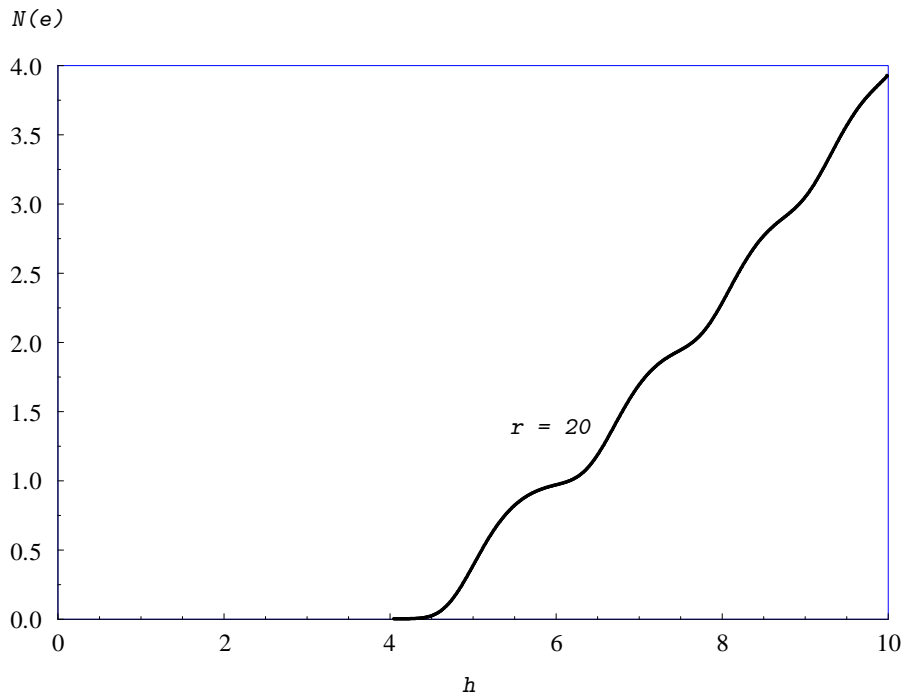


Figure 4.12. Neutron count as a function of h for correlation radius of roughness $r = 20$.

being squeezed up and the difference in potentials near the bottom of the well loses its significance.

- The major result of this section is the exit neutron count in the presence of gravity. It illustrates the total neutron count $N_e(h)$ as a function of the width of the channel h . When comparing this result to the work done previously using the biased diffusion approximation, we see that the curves are similar. This means that the biased diffusion approximation is indeed a very robust approximation.

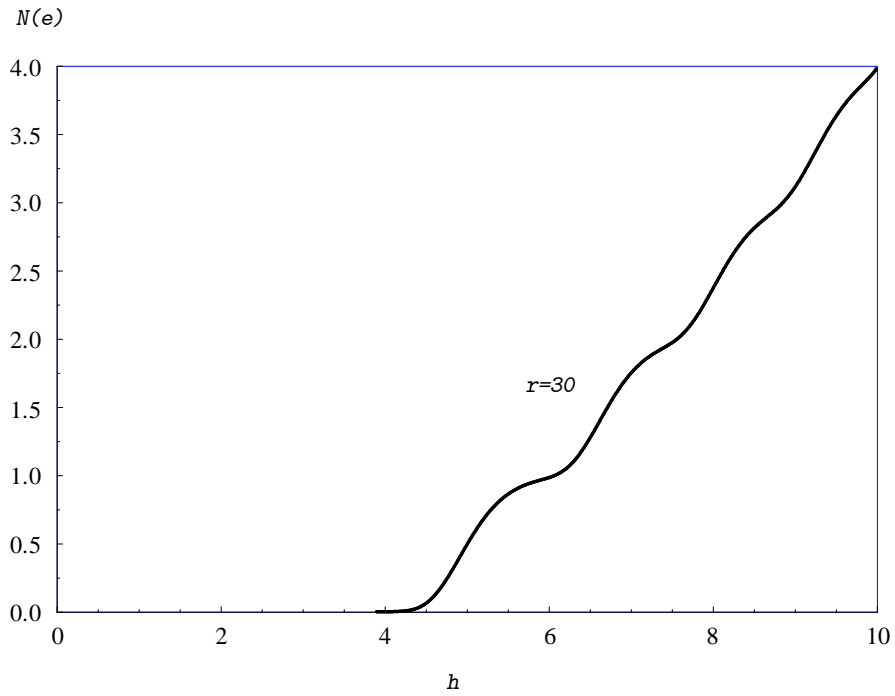


Figure 4.13. Neutron count as a function of h for correlation radius of roughness $r = 30$.

- In almost all computations the exit neutron count as a function of cell width $N_e(h)$ retained the step-wise nature. This may be considered as a unequivocal proof of quantization of neutron motion by the Earth gravitational field.

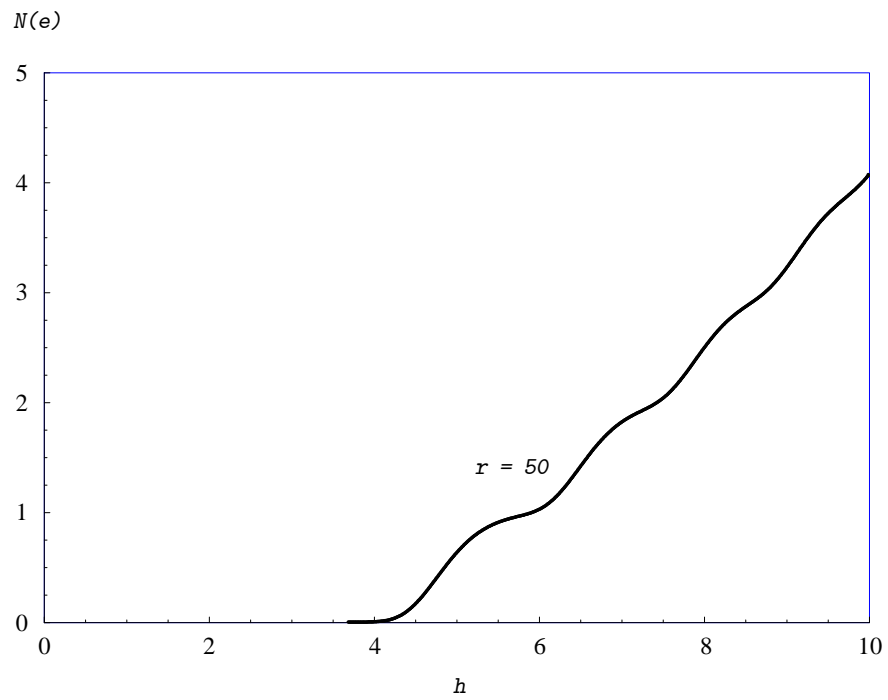


Figure 4.14. Neutron count as a function of h for correlation radius of roughness $r = 50$.

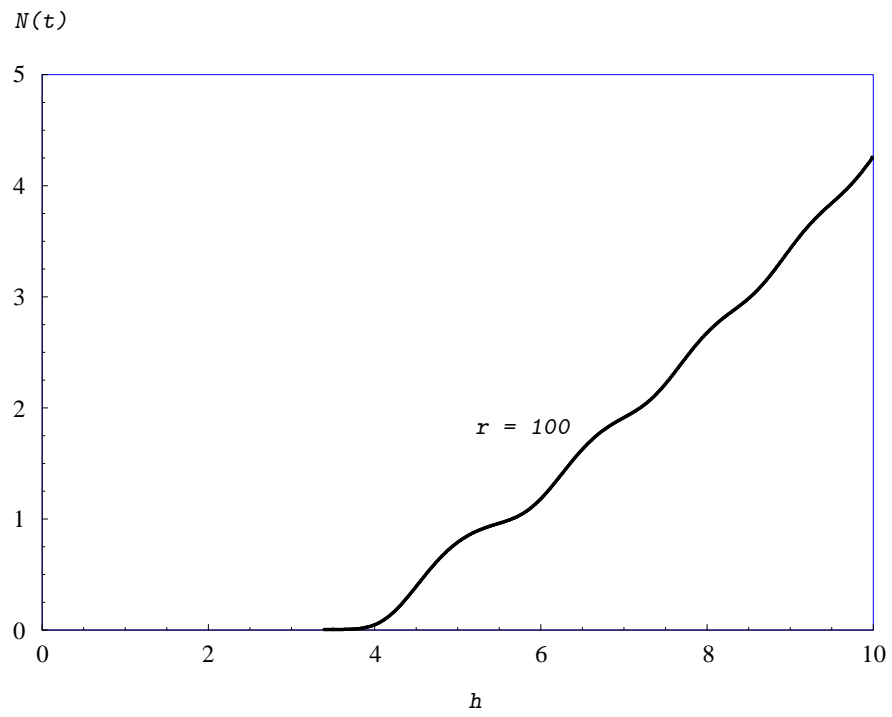


Figure 4.15. Neutron count as a function of h for correlation radius of roughness $r = 100$.

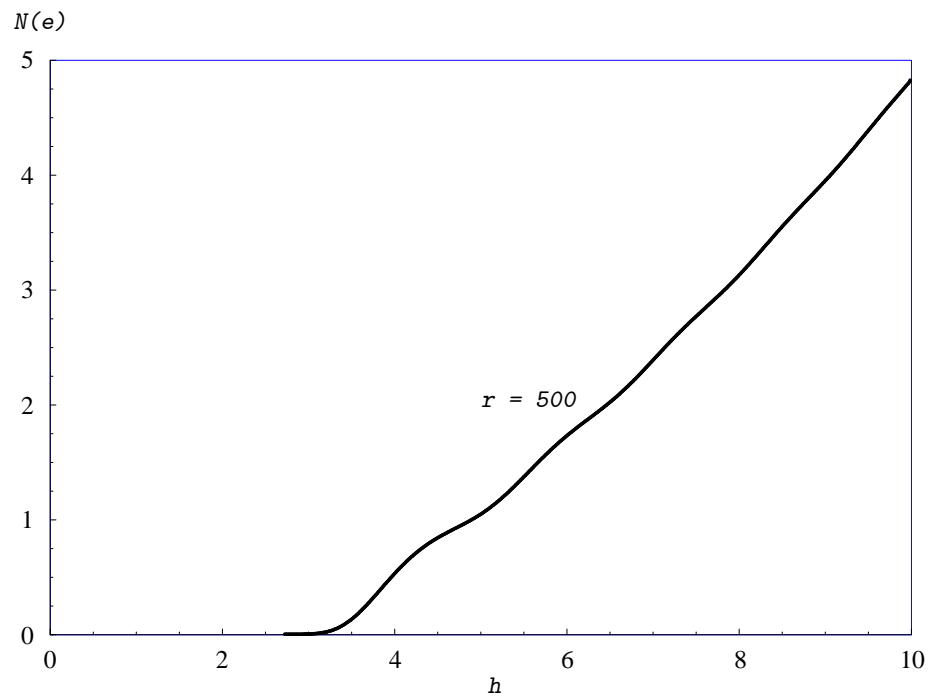


Figure 4.16. Neutron count as a function of h for correlation radius of roughness $r = 500$.

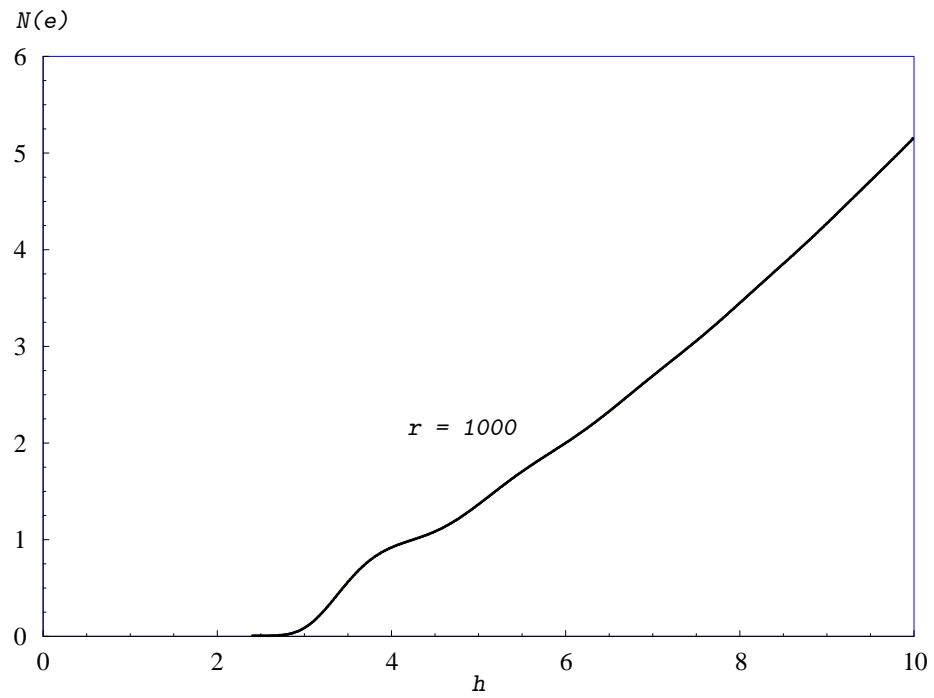


Figure 4.17. Neutron count as a function of h for correlation radius of roughness $r = 1000$.

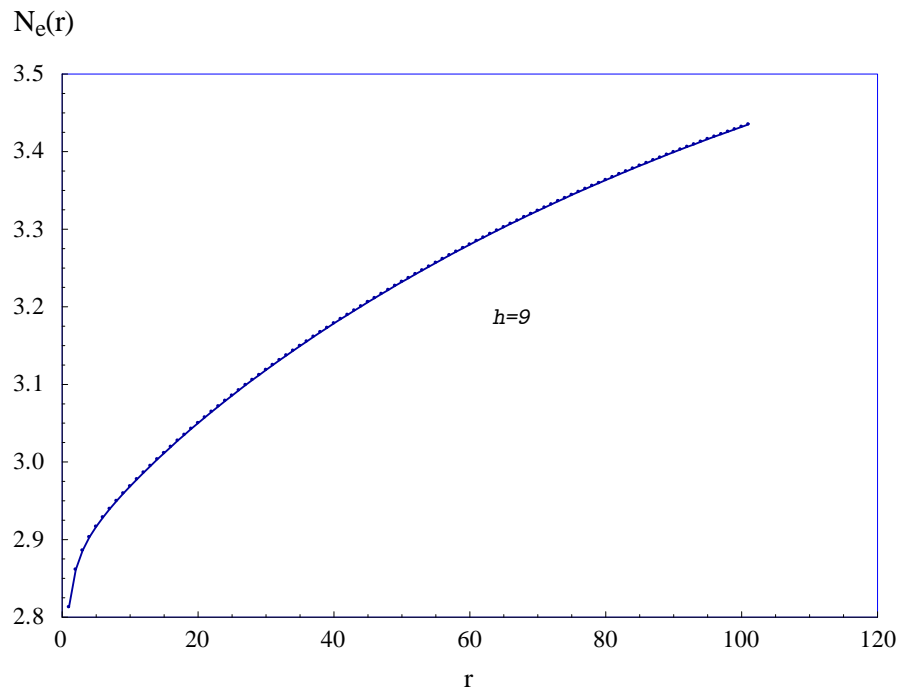


Figure 4.18. Neutron exit count for fixed well width at $h = 9$, over a large range of r .

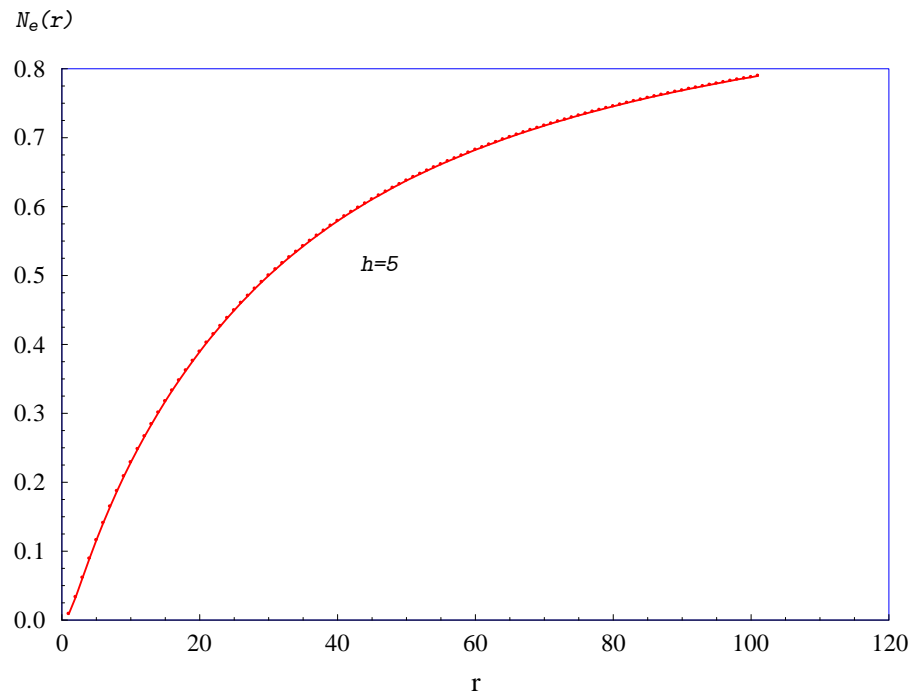


Figure 4.19. Neutron exit count for fixed well width at $h = 5$, over a large range of r .

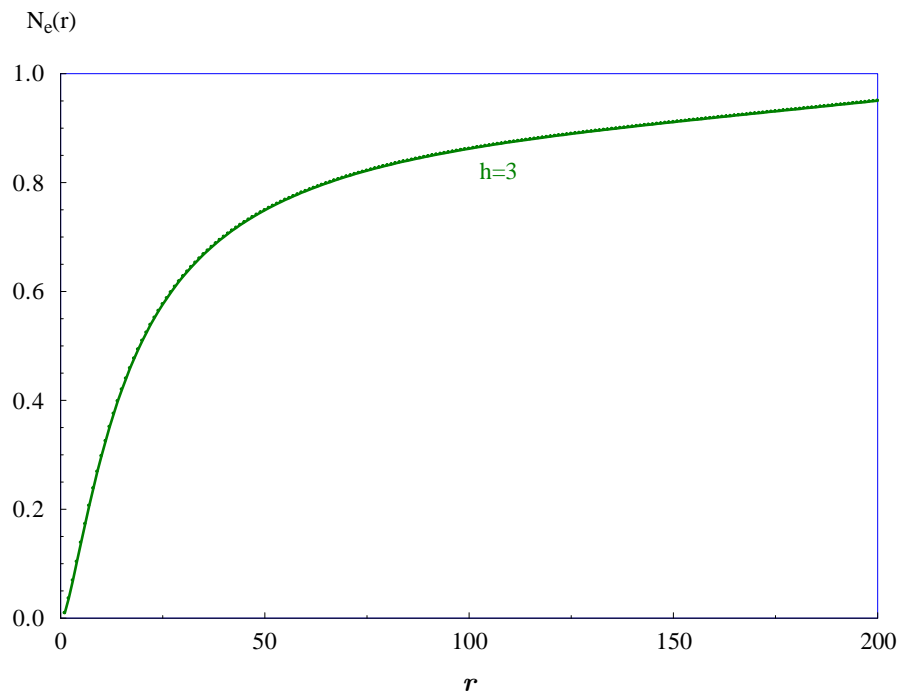


Figure 4.20. Neutron exit count for fixed well width at $h = 3$, over a large range of r .

CHAPTER 5

Summary and Conclusions

5.1. Main Conclusions

In summary, the main goal of this thesis was to provide a rigorous theoretical description for the diffusion of ultra cold neutrons (UCN) through narrow rough channels. We used the general transport theory of particles along rough surfaces to the gravitationally quantized diffusion of UCN in a rough waveguide. We looked at two separate problems: diffusion of the neutrons through rough waveguides on the way from the reactor to the experimental cell and the neutron count for neutrons exiting experimental cell with absorbing walls in the square well potential as well as the gravitational potential. We used numerical calculations to investigate the effect of two types of random roughness on the diffusion coefficient, as well as to evaluate the neutron count using the experimental input parameters in both potentials.

The main content of Chapter 2 is the calculations of the diffusion coefficient and the mean free path for ultra-cold neutrons in narrow channels with random rough walls. We determined that if one wants to effectively turn back the neutrons which got into the gaps in the channel junctions, one should make the correlation radius of surface roughness as small as possible. We compared the behavior of $d(r)$

and $l(r)$ for surfaces with the Gaussian and the exponential correlation functions of surface roughness. We found that there is a complicated minimum in $d(r)$ and $l(r)$ for small correlation radius $r \sim 2 \times 10^{-4}$. Additionally we found that the diffusion coefficient and the MFP rapidly increase as the correlation radius r increases, though at different rates depending on the surface correlation function. The growth of the diffusion coefficient and MFP is not monotonic, there is more than one minimum at $q_j \sim 1/r$. We saw that at large r the function $d(r)$ behaves roughly as r^3 , where the exponent slightly drifts with r . The computations were done for realistic values of the channel width $h = 8.52$. At different values of h the results were qualitatively the same. The growth of $d(r)$ and $l(r)$ for the Gaussian surface correlation function is much faster than for the exponential correlation function. As a result, it is preferable to have the junction walls with exponential correlation of inhomogeneities.

The conclusions for Chapter 3 regarding the UCN in the square well potential are as follows: Irrespective of the well width and the correlation radius, a good cutoff parameter for all computations is around $S1 = 300$. We see that as the radius of roughness r increases, the total neutron count goes to zero for smaller and smaller values of h . However, as we can see from the plots, the numbers that we get for $N_e(h)$ are always extremely small, so essentially all the neutrons die almost immediately. As we will see in this Chapter, this is not the case for the gravitational well. Hence, we can say that the square well approximation is very poor for this particular problem: though the weak Earth gravitational field

introduces only a small distortion near the bottom of the potential well, its effect on the neutron survival rate is very large.

The main conclusion for Chapter 4 is the exit neutron count in the presence of gravity. It illustrates the total neutron count $N_e(h)$ as a function of the width of the channel h . When comparing this result to the work done previously using the biased diffusion approximation, we see that the curves are similar. This means that the biased diffusion approximation is a very robust approximation. This result was a somewhat surprising result. Other conclusions include the following. The dependence of the exit neutron count on r was much more significant in the case of the square well potential where $N_e(r)$ at fixed h changed by many orders of magnitude. It is interesting to note that the ratio of the relaxation times for the diagonal case (in which we do not take into account the transitions between the states, meaning the cases where $j \neq j'$) and the case described in this Chapter (where we allow all the transitions, and not just the biased ones to be taken into account) τ_{diag}/τ_{full} is close to 1. This was rather unexpected. It is also interesting to note that the ratio of the results for the square well potential and the gravitational potential goes to one as h goes to 0, $\tau_{jSquarewell}/\tau_{jgrav} \rightarrow 1$ as $h \rightarrow 0$ since all the levels are being squeezed up and the difference in potentials near the bottom of the well loses its significance, see Figure above.

5.2. Recommendations for Future Work

Using rough mirrors as a quantum state selector can be extended beyond this series of GRANIT experiments. Some of the more exciting experiments include the observation of quantum gravitational states for other ultra-cold particles and anti-particles in the context of the GBAR experiment at CERN.

One of the main goals of the GBAR experiments is to measure the acceleration in free fall of ultra-cold neutral anti hydrogen atoms in the Earth's gravitational field. The experiment entails using anti hydrogen ions, which consist of one anti-proton supplied by the ELENA deceleration ring at CERN and two positrons created by the linac, and cooling them below $10 \mu\text{K}$ with Beryllium plus ions. Their positive charge makes them easier to manipulate. Using lasers, their velocity can be reduced to half a meter per second. Once they are trapped by an electric field, one of their positrons will be removed with laser, which will make it neutral. Hence, at this point the Earth's gravitational field will be the only force acting upon them, and they will be able to free fall a given distance, and their time of fall could be measured. The results of this experiment are much anticipated, because it could potentially mean that gravity might have a different effect on antimatter than it does on matter.

For the past 60 years, there has also been an ongoing search for the neutron electric dipole moment (nEDM). Over the course of the decades the accuracy of (negative) results has been improved by many orders of magnitude. The nEDM

potentially violates CP symmetry, meaning that it violates the presumption that if a particle and a respective anti particle are interchanged, while their spatial coordinates are inverted, then the laws of physics should remain the same. The goal of these ongoing and future nEDM experiments is to improve the sensitivity for detection nEDM by orders of magnitude. One of the experiments being done at Oak Ridge National Laboratory is to create a three-component fluid described as isotopically purified Helium-4, a trace amount of spin-polarized Helium-3, and spinpolarized ultra-cold neutrons. Then once that fluid has been created, it should be exposed to a small but homogeneous magnetic field and a large electric field. The nEDM could then be measured by looking at the neutron precession frequency which is linearly dependent on the magnitude of the electric field strength, and whose sign is dependent on the alignment between the magnetic and electric fields.

Above are just examples of the experiments that are ongoing or planned for the near future, however, our theoretical work on the use of rough mirrors as quantum state selectors are well suited for dealing with these and similar applications.

APPENDIX A

Dimensionless Transition Probabilities

In this Appendix we make the equations for the harmonics of the transition probabilities dimensionless. According to Ref. [[2]], the angular harmonics of the transition probabilities for surfaces with Gaussian correlations of surface inhomogeneities. are

$$(A.1) \quad W_{jj'}^{(0,1)} = \frac{\hbar}{m^2 H^2} \left(\frac{\pi j}{H} \right)^2 \left(\frac{\pi j'}{H} \right)^2 4\pi l^2 R^2 I_0(QQ') \text{Exp}(-QQ') \text{Exp}\left(-\frac{1}{2}(Q - Q')^2\right).$$

Then

$$(A.2) \quad W_{jj'}^{(0,1)} * w_0 = \frac{\hbar}{m^2 H^2} \left(\frac{\pi j}{h} \right)^2 \left(\frac{\pi j'}{h} \right)^2 4\pi \eta^2 r^2 I_0(QQ') \text{Exp}(-QQ') \text{Exp}\left(-\frac{1}{2}(Q - Q')^2\right)$$

where $w_0 = m\tau_0$, with $\tau_0 = (4ml_0^2)/(\sqrt{2\pi\hbar})$. As a result the dimensionless equations become

$$(A.3) \quad w_{jj'}^{(0,1)} = \frac{\hbar}{m^2 H^2} \left(\frac{\pi j}{h} \right)^2 \left(\frac{\pi j'}{h} \right)^2 4\pi \eta^2 r^2 \left(m \frac{4ml_0^2}{\sqrt{2\pi\hbar}} \right) I_0(QQ') \text{Exp}(-QQ') \text{Exp}\left(-\frac{1}{2}(Q - Q')^2\right)$$

(A.4)

$$w_{jj'}^{(0,1)} = \frac{4l_0^2}{\sqrt{2\pi}H^2} (4\pi\eta^2 r^2) \left(\frac{\pi j}{h}\right)^2 \left(\frac{\pi j'}{h}\right)^2 I_0(QQ') \text{Exp}(-QQ') \text{Exp}\left(-\frac{1}{2}(Q-Q')^2\right)$$

$$(A.5) \quad w_{jj'}^{(0,1)} = \frac{8\pi\eta^2 r^2}{\sqrt{2\pi}h^2} \left(\frac{\pi j}{h}\right)^2 \left(\frac{\pi j'}{h}\right)^2 I_0(QQ') \text{Exp}(-QQ') \text{Exp}\left(-\frac{1}{2}(Q-Q')^2\right)$$

Therefore, our final equation for the transition probability for the Gaussian correlator becomes

(A.6)

$$w_{jj'}^{(0,1)} = \frac{8\pi}{\sqrt{2\pi}} \left(\frac{r}{h}\right)^2 \left(\frac{\pi j}{h}\right)^2 \left(\frac{\pi j'}{h}\right)^2 I_{(0,1)}(QQ') \text{Exp}(-QQ') \text{Exp}\left(-\frac{1}{2}(Q-Q')^2\right)$$

Note that in computations we assume the scaling parameter $\eta = 1$.

Additionally, in the same way, we derive the dimensionless transition probabilities for the exponential roughness,

$$(A.7) \quad w_{jj'}^{(0)} = \frac{32r^2}{\sqrt{2\pi}h^2} \left(\frac{\pi j}{h}\right)^2 \left(\frac{\pi j'}{h}\right)^2 \frac{E\left(2r\sqrt{\frac{q_j q_{j'}}{(1+r^2(q_j+q_{j'})^2)}}\right)}{(1+r^2(q_j-q_{j'})^2)(\sqrt{1+r^2(q_j+q_{j'})^2})}$$

(A.8)

$$w_{jj'}^{(1)} = \frac{16}{\sqrt{2\pi}h^2} \left(\frac{\pi j}{h}\right)^2 \left(\frac{\pi j'}{h}\right)^2 \times \frac{(1+r^2(q_j^2+q_{j'}^2))E\left(2r\sqrt{\frac{q_j q_{j'}}{(1+r^2(q_j+q_{j'})^2)}}\right) - (1+r^2(q_j-q_{j'})^2)K\left(2r\sqrt{\frac{q_j q_{j'}}{(1+r^2(q_j+q_{j'})^2)}}\right)}{(1+r^2(q_j-q_{j'})^2)(\sqrt{1+r^2(q_j+q_{j'})^2})}$$

APPENDIX B

Asymptotic Expansion for Transition Probabilities for Surfaces with Exponential Roughness Correlator

Here we present an asymptotic expansion for the transition probabilities for the surfaces with the exponential roughness correlator.

We need an asymptotic expression for:

$$(B.1) \quad \text{Exp}(-x^2) * (I_0(x^2) - I_1(x^2))$$

At large x ,

$$(B.2) \quad I_0(x^2) \sim \frac{\text{Exp}(-x^2)}{\sqrt{2\pi x^2}} \left(1 - \left(\frac{-1}{8x^2} \right) + \left(\frac{(-1)(-9)}{2!(8x)^2} \right) - \dots \right)$$

since

$$(B.3) \quad I_0(x^2) \sim \frac{\text{Exp}(-x^2)}{\sqrt{2\pi x^2}} \left(1 + \left(\frac{1}{8x^2} \right) \right)$$

and,

$$(B.4) \quad I_1(x^2) \sim \frac{\text{Exp}(-x^2)}{\sqrt{2\pi x^2}} \left(1 - \left(\frac{4-1}{8x^2} \right) + \left(\frac{(4-1)(4-9)}{4 * 64 * x^4} \right) - \dots \right)$$

$$(B.5) \quad I_1(x^2) \sim \frac{\text{Exp}(-x^2)}{\sqrt{2\pi x^2}} \left(1 - \left(\frac{3}{8x^2} \right) \right)$$

As a result,

$$(B.6) \quad w_{jj'}^{(0,1)} = \frac{8\pi}{\sqrt{2\pi}} \left(\frac{r}{h} \right)^2 \left(\frac{\pi j}{h} \right)^2 \left(\frac{\pi j'}{h} \right)^2 I_{(0,1)}(QQ') \text{Exp}(-QQ') \text{Exp}\left(-\frac{1}{2}(Q - Q')^2\right)$$

If we replace the exact transition probabilities by these asymptotic expansions, we get almost identical numerical results. We tried using this expansion to see if we could speed up computation time

APPENDIX C

Diagonal Elements of Transition Probabilities for the Biased Diffusion Approximation

In this Appendix we try to replace the summation over discrete states in Eq.(4.12) by integration. Starting from the equation, Eq.(4.12) and using the following definitions,

$$(C.1) \quad b_j = 10^5 \frac{\lambda_j}{h u_c},$$

$$(C.2) \quad \lambda_j = \frac{\pi^2 j^2}{h^2},$$

$$F_2(r, h) = \sqrt{\frac{2}{\pi}} \times 10^{-5} r^4 \sum_{j' > 1} b_{j'} \psi_2(y_1, y_{j'})$$

we can rewrite this expression in the following way

$$(C.3) \quad F_2(r, h) = \sqrt{\frac{2}{\pi}} \times 10^{-5} r^4 \sum_{j' > 1} 10^5 \frac{\lambda_j}{h u_c} \psi_2(y_1, y_{j'})$$

$$(C.4) \quad = \sqrt{\frac{2}{\pi}} r^4 \sum_{j' > 1} \frac{\lambda_j}{h u_c} \psi_2(y_1, y_{j'})$$

$$(C.5) \quad = \sqrt{\frac{2}{\pi}} r^4 \left(\frac{\pi^2}{h^3 u_c} \right) \sum_{j' > 1} j'^2 \psi_2(y_1, y_{j'})$$

Now note that $\mathcal{N} = \frac{h}{\pi} \varepsilon^{\frac{1}{2}}$, and $\chi = \frac{u_c}{\varepsilon}$, therefore we know that $\mathcal{N} = \frac{h}{\pi} \left(\frac{u_c}{\chi} \right)^{\frac{3}{2}}$. It should also be noted that we can write $\left(\frac{\pi^2}{h^3 u_c} \right)$ as follow,

$$(C.6) \quad \left(\frac{\pi^2}{h^3 u_c} \right) = \left(\frac{\pi \chi^{3/2}}{u_c^{1/2}} \right)^{-1} \left(\frac{\pi \chi^{3/2}}{u_c^{1/2}} \right) \left(\frac{\pi^2}{h^3 u_c} \right)$$

$$(C.7) \quad = \left(\frac{u_c^{1/2}}{\pi \chi^{3/2}} \right) \left(\frac{\pi^3 \chi^{3/2}}{h^3 u_c^{3/2}} \right)$$

$$(C.8) \quad = \left(\frac{u_c^{1/2}}{\pi \chi^{3/2}} \right) \left(\frac{1}{\mathcal{N}} \right)$$

hence we can rewrite $F_2(r, h)$ as,

$$(C.9) \quad F_2(r, h) = \sqrt{\frac{2}{\pi}} r^4 \left(\frac{u_c^{1/2}}{\pi \chi^{3/2}} \right) \frac{1}{\mathcal{N}^3} \sum_{j' > 1} j'^2 \psi_2(y_1, y_{j'})$$

Now to make this a continuous function we can replace the sum by an integral,

$$(C.10) \quad F_2(r, h) = \sqrt{\frac{2}{\pi}} r^4 \left(\frac{u_c^{1/2}}{\pi \chi^{3/2}} \right) \frac{1}{\mathcal{N}^3} \int_1^{\mathcal{N}} j'^2 \psi_2(y_1, y_{j'})$$

where we substitute $z = \frac{j}{\mathcal{N}}$ and $\frac{dj}{\mathcal{N}} = dz$ and then we can write $z^2 = \frac{j^2}{\mathcal{N}^2}$. The above equation now becomes,

$$(C.11) \quad F_2(r, h) = \sqrt{\frac{2}{\pi}} r^4 \left(\frac{u_c^{1/2}}{\pi \chi^{3/2}} \right) \frac{1}{\mathcal{N}^3} \int_0^1 z^2 \mathcal{N}^2 dz \mathcal{N} \psi_2(y_1, y_{j'})$$

$$(C.12) \quad = \sqrt{\frac{2}{\pi}} r^4 \left(\frac{u_c^{1/2}}{\pi \chi^{3/2}} \right) \int_0^1 dz z^2 \psi_2(y_1, y_{j'}),$$

which is Eq.(4.10) in the main text. This equation was used in Ref??.

Bibliography

- [1] A. Meyerovich and V. V. Nesvizhevsky, "Gravitational quantum states of neutrons in a rough waveguide," *Phys. Rev. A*, vol. 73, 063616, June 2006.
- [2] R. Adhikari, Y. Cheng, and A. E. Meyerovich, "Quantum size effect and biased diffusion of gravitationally bound neutrons in a rough waveguide," *Phys. Rev. A*, vol. 75, 063613, June 2007.
- [3] A. E. Meyerovich and A. Stepaniants, "Quantized systems with randomly corrugated walls and interfaces," *Phys. Rev. B*, vol. 60, no. 12, p. 9129, 1999.
- [4] A. E. Meyerovich and A. Stepaniants, "Transport equation and diffusion in ultrathin channels and films," *Phys. Rev. B*, vol. 58, p. 13 242, Nov. 1998.
- [5] A. E. Meyerovich and A. Stepaniants, "Transport phenomena at rough boundaries," *Phys. Rev. Lett.*, vol. 73, no. 2, p. 316, July 1994.
- [6] Y. Cheng and A. E. Meyerovich, "Mode coupling in quantized high-quality films," *Phys. Rev. B*, vol. 73, 085404, Feb. 2006.
- [7] A. E. Meyerovich and I. V. Ponomarev, "Surface roughness and size effects in quantized films," *Phys. Rev. B*, vol. 65, 155413, 2002.19
- [8] M. Escobar and A. Meyerovich, "Beams of gravitationally bound ultra-cold neutrons in a rough waveguide," *Phys. Rev. A*, vol. 83, 033618, Mar. 2011.
- [9] M. Escobar and A. Meyerovich, "Applications and identification of surface correlations," *arXiv:1404.1291*, 2014.
- [10] M. Escobar and A. Meyerovich, "Quantized ultra-cold neutrons in rough waveguides: GRANIT experiments and beyond," *Advances in High Energy Physics*, vol. 2014, Article ID: 185414, July 2014.

- [11] M. Escobar, F. Lamy, A. E. Meyerovich, and V. V. Nesvizhevsky, "Rough mirror as a quantum state selector: analysis and design," *Advances in High Energy Physics*, vol. 2014, Article ID: 764182, Aug. 2014.
- [12] M. Escobar and A. E. Meyerovich, "Quantum transport equation for systems with rough surfaces and its application to ultra-cold neutrons in a quantizing gravity field," *Journal of Experimental and Theoretical Physics*, vol. 119, no. 6, pp. 1123{1133, 2014.
- [13] M. Escobar, "Quantum Diffusion Of Ultra-Cold Neutrons in a Rough Waveguide in a Gravity Field", University of Rhode Island, 2015.
- [14] V. V. Nesvizhevsky, H. G. Borner, A. K. Petukhov, H. Abele, S. Baessler, F. J. Rueb, T. Stoferle, A. Westphal, A. M. Gagarski, G. A. Petrov, and A. V. Strelkov, "Quantum states of neutrons in Earth's gravitational field," *Nature*, vol. 415, pp. 297{299, Nov. 2002.
- [15] V. V. Nesvizhevsky, "Investigation of quantum neutron states in the terrestrial gravitational field above a mirror," *Physics-Uspekhi*, vol. 47 (5), p. 515, 2004.
- [16] V. V. Nesvizhevsky, H. G. Borner, A. M. Gagarski, A. K. Petoukhov, G. A. Petrov, H. Abele, S. Baessler, G. Divkovic, F. J. Rueb, T. Stoferle, A. Westphal, A. V. Strelkov, K. V. Protasov, and A. Y. Voronin, "V. V. Nesvizhevsky, "Investigation of quantum neutron states in the terrestrial gravitational field above a mirror," *Phys. Rev. D*, vol. 67, 102002, 2003.
- [17] V. V. Nesvizhevsky, A. K. Petukhov, H. G. Borner, T. A. Baranova, A. M. Gagarski, G. A. Petrov, K. V. Protasov, A. Y. Voronin, S. Baessler, H. Abele, A. Westphal, and L. Lucovac, "Study of the neutron quantum states in the gravity field," *Eur. Phys. J. C*, vol. 40, pp. 479{491, 2005.
- [18] V. V. Nesvizhevsky, H. Borner, A. M. Gagarski, G. A. Petrov, A. K. Petukhov, H. Abele, S. Baessler, T. Stoferle, and S. M. Soloviev, "Search for quantum states of neutron in a gravitational field: gravitational levels," *Nuclear Instruments and Methods in Physics Research A*, vol. 440, pp. 754{759, 2000.
- [19] V. V. Nesvizhevsky and K. V. Protasov, *Trends in Quantum Gravity Research*. Nova Science Publishers, Inc., 2006.20

- [20] I. Antoniadis, S. Baessler, O. Bertolami, D. Dubbers, A. Meyerovich, V. V. Nesvizhevsky, K. Protasov, and S. Reynaud, *C. R. Physique* 12, vol. 8, pp.703{706, Oct. 2011.
- [21] S. Baessler, M. Beau, M. Kreuz, V. N. Kurlov, V. V. Nesvizhevsky, G. Pignol, K. V. Protasov, F. Vezzu, and A. Y. Voronin, "The GRANIT spectrometer," *C. R. Physique*, vol. 12, pp. 707{728, 2011.
- [22] S. Baessler, A. M. Gagarski, E. V. Lychagin, A. Mietke, A. Y. Muzychka, V. V. Nesvizhevsky, G. Pignol, A. V. Strelkov, B. P. Toperverg, and K. Zherrenkov, "New methodical developments for GRANIT," *C. R. Physique*, vol. 12, pp.729{754, 2011.
- [23] A. Westphal, "Quantum Mechanics and Gravitation," Ph.D. dissertation, University of Heidelberg, 2001. [Online]. Available: arxiv.org/pdf/gr-qc/0208062.
- [24] C. Krantz, "Quantum States of Neutrons in the Gravitational Field," Ph.D. dissertation, University of Heidelberg, 2006. [Online]. Available:<http://www.physi.uni-heidelberg.de/Publications/>
- [25] A. Y. Voronin, H. Abele, S. Baessler, K. V. Protasov, and A. Westphal, "Quantum motion of a neutron in a wave-guide in the gravitational field," *Phys. Rev. D*, vol. 73, 044029, Feb. 2006.
- [26] V. V. Nesvizhevsky, K. Petukhov, K. V. Protasov, and A. Y. Voronin, "Centrifugal quantum states of neutrons," *Phys. Rev. A*, vol. 78, 033616, 2008.
- [27] V. V. Nesvizhevsky and A. Y. Voronin, "Centrifugal quantum states of neutrons," *C. R. Physique*, vol. 12, pp. 791{795, 2011.
- [28] A. Y. Voronin, P. Froelich, and V. V. Nesvizhevsky, "Gravitational quantum states of antihydrogen," *Phys. Rev. A*, vol. 83, 032903, Mar. 2011.
- [29] A. Y. Voronin, V. V. Nesvizhevsky, and S. Reynaud, "Whispering-gallery of antihydrogen near a curved surface," *Phys. Rev. A*, vol. 85, 014902.
- [30] G. Dufour, P. Debu, A. Lambrecht, V. V. Nesvizhevsky, S. Reynaud, and A. Y. Voronin, "Shaping the distribution of vertical velocities of antihydrogen in GBAR," *arXiv:1312.5534v1 [quant-ph]*, 2002.

- [31] P. Crivelli, V. V. Nesvizhevsky, and A. Y. Voronin, "Can we observe the gravitational quantum states of Positronium?" arXiv:1408.7051v1 [physics.atom-ph], 2014.
- [32] A. Y. Voronin, V. V. Nesvizhevsky, and S. Reynaud, "Whispering-gallery states of antihydrogen near a curved surface," *Nature Physics*, vol. 6, 114-117 2010.21
- [33] I. Antoniadis, S. Baessler, M. Buchner, V. V. Fedorov, S. Hoedl, A. Lambrecht, V. V. Nesvizhevsky, G. Pignol, K. V. Protasov, S. Reynaud, and Y. Sobolev, "Short-range fundamental forces," *C. R. Physique*, vol. 12, pp. 775{778, 2011.
- [34] S. Baessler, V. V. Nesvizhevsky, G. Pignol, K. V. Protasov, and A. Y. Voronin, "Constraints on spin-dependent short-range interactions using gravitational quantum levels of ultra-cold neutrons," arXiv:0902.3139, 2009.
- [35] M. Kreuz, V. V. Nesvizhevsky, P. Schmidt-Wellenburg, T. Soldner, M. Thomas, H. G. Borner, F. Naraghi, G. Pignol, K. V. Protasov, D. Rebreyend, F. Vezzu, R. Flaminio, C. Michel, N. Morgado, L. Pinar, S. Baessler, A. M. Gagarski, L. A. Grigorieva, T. M. Kuzmina, A. E. Meyerovich, L. P. Mezhov-Deglin, G. A. Petrov, A. V. Strelkov, and A. Y. Voronin, "A method to measure the resonance transitions between the gravitationally bound quantum states of neutrons in the GRANIT spectrometer," *Nucl. Instrum. Meth. A*, vol. 611, pp. 326{330, 2009.
- [36] T. Jenke, P. Geltenbort, H. Lemmel, and H. Abele, "Realization of a gravityresonance-spectroscopy technique," *Nature Physics*, vol. 7, pp. 468{472, 2011.
- [37] G. L. Greene and V. Gudkov, "Neutron interferometric method to provide improved constraints on non-newtonian gravity at the nanometer scale," *Phys. Rev. C*, vol. 75, 015501, 2007.
- [38] V. V. Nesvizhevsky, G. Pignol, and K. V. Protasov, "Neutron scattering and extra-short-range interactions," *Phys. Rev. D*, vol. 77, 034020, 2008.
- [39] T. Jenke, G. Cronenberg, J. Burgdorfer, L. A. Chizova, P. Geltenbort, A. N. Ivanov, T. Lauer, T. Lins, S. Rotter, H. Saul, U. Schmidt, and H. Abele, "Gravity Resonance Spectroscopy Constrains Dark Energy and Dark Matter Scenarios," *Phys. Rev. Lett.*, vol. 112, p. 151105, 2014.

- [40] S. Schleich and E. Rasel, "Neutrons knock at the cosmic door," *Physics*, vol. 7, no. 39, Apr. 2014.
- [41] O. Bertolami and F. M. Nunes, "ultra-cold neutrons, quantum effects of gravity and the weak equivalence principle," arXiv:hep-ph/0204284, 2002.
- [42] T. Bourdel, M. Doser, A. D. Ernest, A. Y. Voronin, and V. V. Voronin, "Quantum phenomena in gravitational field," *C. R. Physique*, vol. 12, pp.779{790, 2011.
- [43] O. Bertolami, J. G. Rosa, C. M. L. de Aragao, P. Castorina, and D. Zap-pala, "Noncommutative gravitational quantum well," *Phys. Rev. D*, vol. 72, 025010, July 2005.
- [44] O. Bertolami, "Nonlinear corrections to quantum mechanics from quantum gravity," *Phys. Lett. A*, vol. 154, pp. 225{229, Apr. 1991. 22
- [45] P. Brax and G. Pignol, "Strongly coupled chameleons and the neutronic quantum bouncer," *Physics Review Letters*, vol. 107, p. 111301.
- [46] J. H. Smith, E. M. Purcell, and N. F. Ramsey, "Experimental limit to the electric dipole moment of the neutron," *Phys. Rev.*, vol. 108, no. 1, Oct. 1957.
- [47] C. A. Baker, D. D. Doyle, K. Green, M. G. D. van der Grinten, P. G. Harris, P. Iadjiev, S. N. Ivanov, D. J. R. May, J. M. Pendlebury, J. D. Rischardson, D. Shiers, and K. F. Smith, "Improved experimental limit on the electric dipole moment of the neutron," *Phys. Rev. Lett*, vol. 97, 131801, Sept. 2006.
- [48] H. F. Dylla and J. C. King, "Neutrality of Molecules by a New Method," *Phys. Rev.*, vol. A7, pp. 1224{1229, 1973.
- [49] K. Durstberger-Rennhofer, T. Jenke, and H. Abele, "Probing neutron's electric neutrality with ramsey spectroscopy of gravitational quantum states of ultra-cold neutrons," *Phys. Rev. D*, vol. 84, 036004, 2011.
- [50] A. T. Yue, M. S. Dewey, D. M. Gilliam, G. L. Greene, A. B. Laptev, J. S. Nico, W. M. Snow, and F. E. Wietfedt, "Improved Determination of the Neutron Lifetime," *Phys. Rev. Lett.*, vol. 111, 22501, Nov. 2013.

- [51] J. A. Ogilvy, Theory of wave scattering from random surfaces. IOP Publishing, 1991.
- [52] J.A. Ogilvy and J. R. Foster, "Rough surfaces: gaussian or exponential statistics?" J. Phys. D: Appl. Phys., vol. 22, pp. 1243{1251, 1989.
- [53] R. C. Munoz, G. Vidal, G. Kremer, L. Moraga, and C. Arenas, "Surface induced resistivity of gold lms on mica: comparison between the classical and the quantum theory," J. Phys.: Condens. Matter, vol. 11, pp. L299{L307, 1999.
- [54] R. C. Munoz, G. Vidal, G. Kremer, L. Moraga, and C. Arenas, "Surface roughness and surface-induced resistivity of gold films on mica: influence of roughness modelling," J. Phys.: Condens. Matter, vol. 12, pp. 2903{2912, 2000.
- [55] R. C. Munoz, A. Concha, F. Mora, and R. Espejo, "Surface roughness and size effects of thin gold lms on mica," Phys. Rev. B, vol. 61, no. 7, p. 4514, Feb. 2000.
- [56] J. Gea-Banacloche, "A quantum bouncing ball," Am. J. Phys., vol. 67, p. 776,1999.
- [57] M. N. Berberan-Santos, E. N. Bodunov, and L. Pogliani, "Classical and quantum study of the motion of a particle in a gravitational eld," Journal of Mathematical Chemistry, vol. 37, no. 2, 2005 23
- [58] S. Flugge, Practical Quantum Mechanics I. Springer-Verlag, 1999.
- [59] V. I. Luschikov and A. I. Frank, JETP Lett., vol. 28, p. 59, 1978.
- [60] V. V. Nesvizhevsky, "Polished sapphire for ultra-cold-neutron guides," Nuclear Instruments and Methods in Physics Research A, vol. 557, pp. 576{579, 2006.
- [61] V. V. Nesvizhevsky, G. Pignol, K. V. Protasov, G. Quemener, D. Forest, P. Ganau, J. M. Mackowski, C. Michel, J. L. Montorio, N. Morgado, L. Pinard, and A. Remillieux, "Comparison of specularly reflecting mirrors for GRANIT," Nuclear Instruments and Methods in Physics Research A, vol. 578, pp. 435{438, 2007.

- [62] R. Golub, D. Richardson, and S. K. Lamoreaux, ultra-cold neutrons. IOP Publishing, 1991.
- [63] R. Golub and J. M. Pendlebury, "Ultra-cold neutrons," *Rep. Prog. Phys.*, vol. 42, p. 3, 1979.
- [64] V. V. Nesvizhevsky, A. K. Petukhov, H. G. Borner, T. Soldner, P. Schmidt-Wellenburg, M. Kreuz, G. Pignol, K. V. Protasov, D. Rebreyend, F. Vezzu, D. Forest, P. Ganau, J. M. Mackowski, C. Michel, J. L. Montorio, N. Morgado, L. Pinard, A. Remillieux, A. M. Gagarski, G. A. Petrov, A. M. Kusmina, A. V. Strelkov, H. Abele, S. Baessler, and A. Y. Voronin, "GRANIT project: a trap for gravitational quantum states of ultra-cold neutrons," arXiv:0708.2541v1, 2007.
- [65] D. Roulier, F. Vezzu, S. Baessler, B. Clement, D. Morton, V. Nesvizhevsky, G. Pignol, and D. Rebreyend, "Status of the GRANIT facility," arXiv:1410.1376v1[physics.ins-det], 2014.
- [66] I. Kurganskaya, A. Luttge, and A. R. Barron, "The application of VSI to the Study of Crystal Surface Processes," *Connexions*, 2009. [Online]. Available: <http://cnx.org/content/m22326/1.4/>
- [67] G. Fishman and D. Calecki, "Influence of surface roughness on the conductivity of metallic and semiconducting quasi-two-dimensional structures," *Phys. Rev. B*, vol. 43, no. 14, 1991.
- [68] G. Fishman and D. Calecki, "Surface-induced resistivity of ultrathin metallic films: a limit law," *Phys. Rev. Lett.*, vol. 62, no. 11, 1989.
- [69] S. M. Goodnick, D. K. Ferry, C. W. Wilmsen, Z. Liliental, D. Fathy, and O. L. Krivanek, "Surface roughness at the Si(100)-SiO₂ interface," *Phys. Rev. B*, vol. 32, no. 12, Dec. 1985.
- [70] F. G. Bass and I. M. Fuks, "Wave scattering from statistically rough surfaces". Pergamon, New York, 1979.24
- [71] S. K. Sinha, E. B. Sirota, S. Garo, and H. B. Stanley, "X-ray and neutron scattering from rough surfaces," *Phys. Rev. B*, vol. 38, no. 4, p. 2297, 1998.